Master Thesis

Meteorological Institute

Universität Hamburg

Cloud Geometry of Trade Wind Cumuli from Aircraft Observations

M.Sc. Meteorology at the Faculty of Mathematics, Informatics and Natural Sciences

Author:

Henning Dorff

Matriculation Number:

6546653

1st Supervisor:

Prof. Dr. Felix Ament

2nd Supervisor:

Dr. Heike Konow

March 02, 2020

Topic of the thesis: „Low-level clouds in the tropics - case studies based on the NARVAL-II aircraft campaign“

Abstract

This thesis examines the geometries of shallow low-level clouds from the NARVAL-II aircraft campaign in the trade wind region, using an airborne remote-sensing multi-device approach. The trade wind cumuli and their interaction within the boundary layer conditions are still limitedly understood, although these clouds are ubiquitous over tropical oceans. High-resolution measurements are necessary to detect the lower end of their cloud size spectrum and to resolve the complex geometries of these clouds.

The instrument payload of the research aircraft HALO during NARVAL-II provides such required datasets. This thesis merges cloud information from a 35.5 GHz cloud radar and the hyperspectral imager specMACS (spectrometer of the Munich Aerosol Cloud Scanner), measuring in the visible and shortwave-infrared spectrum. Using the cloud mask data, the two-dimensional view on clouds from specMACS enables new opportunities to characterise the horizontal extent of clouds in all directions. This analysis benefits from the large cloud sample of specMACS, as the imager detected 80 times more clouds compared to the radar.

Focussing on typical shapes that can be attributed to the cloud geometries, shallow clouds show structures similar to ellipses. Due to the elongation of these clouds, the difficulties in measuring cloud sizes from airborne observations are investigated from different perspectives. Besides the single cloud geometries, the cloud field that is detected by the field of view from specMACS is investigated regarding shallow cloud organisation. Distances between neighbouring clouds are on average lower than 300 m, which is of high relevance for the required resolution of airborne cloud observation systems. Impacts of the predominant trade winds on the two-dimensional cloud geometries are subsequently identified. One of the findings is that trade-wind cumuli tend to become more stretched and tilted into wind direction with increasing wind speed. Along-track cloud size measurements therefore do not necessarily cover the dominant cloud extent.

Overall, the thesis points out the benefits of two-dimensional airborne cloud observations and motivates their importance regarding further analysis of trade-wind cumuli coupling with their environment.

Contents

List of Acronyms

1D one-dimensional.

2D two-dimensional.

3D three-dimensional.

ASTER Advanced Spaceborne Thermal Emission and Reflection Radiometer.

ATEX Atlantic Tradewind EXperiment.

BAHAMAS Basic Halo Measurement and Sensor System.

BCO Barbados Cloud Observatory.

BL boundary layer.

BOMEX Barbados Oceanographic and Meteorological Experiment.

CBH cloud base height.

CERA Climate and Environmental Retrieval and Archive.

CTH cloud top height.

EUREC^{4}A Elucidating the role of clouds-circulation coupling in climate.

FOV field of view.

GCM global climate models.

HALO High Altitude and LOng Range Research Aircraft.

HAMP HALO Microwave Package.

I_{org} Organisation Index.

ID identification number.

ITCZ Intertropical Convergence Zone.

IWV integrated water vapour.

LCL lifting condensation level.

LDR linear depolarisation ratio.

LES large eddy simulation.

MODIS Moderate-Resolution Imaging Spectroradiometer.

NARVAL Next-Generation Aircraft Remote Sensing for Validation Studies.

NN nearest neighbours.

NNCDF cumulative density function of nearest neighbour distances.

RF research flight.

RICO Rain in shallow cumulus over the ocean experiment.

SCAI Simple Convective Aggregation Index.

SMART Spectral Modular Airborne Radiation Measurement System.

SNR signal-to-noise ratio.

SWIR shortwave infrared.

SZA solar zenith angle.

UTC Coordinated Universal Time.

VNIR visible and near infrared spectrum.

VZA viewing zenith angle.

WALES Water Vapour DIAL.

1. Introduction

1.1 Background and Motivation

Within the tropical circulation system, deep convection and shallow convection coexist and lead to several cloud types (Figure 1.1). Along the Intertropical Convergence Zone (ITCZ) strong upward motion and deep convective clouds evoke a large scale deep overturning circulation and lead to the subsidence of dry free atmosphere in the meridional. The trade inversion layer separates low-level easterly winds from the westerlies in the dry free atmosphere and keep the clouds shallow in low levels. These shallow low-level clouds (marine stratocumulus and shallow trade cumulus) constitute the cloud type with the highest frequency of occurrence above tropical oceans outside of the ITCZ (Bony et al., 2017).

The tropical low-level clouds play a crucial role in Earth's climate system, as they partly control climate on global scale. Located in a moist layer and blocked by the shallow overturning circulation, marine low-level clouds are relevant for the transport of moist air masses towards the ITCZ through the trades by collocating water vapour above the oceans. Mesoscale circulations transport moist static energy towards the Hadley circulation. Higher concentration of water vapour within the Tropics thus enhances upwelling and the large scale overturning circulation (Siebesma, 1998) and lead to aggregation of deep convection (Wing and Emanuel, 2014).

The radiative impact of low-level clouds in climate change is still limitedly understood (Nuijens and Siebesma, 2019). According global climate models (GCM), these clouds drive the largest spread in cloud-feedbacks (Medeiros et al., 2015; Ceppi et al., 2017). The response of tropical low-level clouds to global warming varies widely in GCM having a range of local cloud feedbacks about 2 $\mathrm{Wm^{-2}\,K^{-1}}$. Even large eddy simulations (LESs) are only capable to halve these ranges (Klein et al., 2018). Since different mechanisms in GCM and LES are responsible for the low-level cloud feedback, observational studies are still indispensable (Vial et al., 2017).

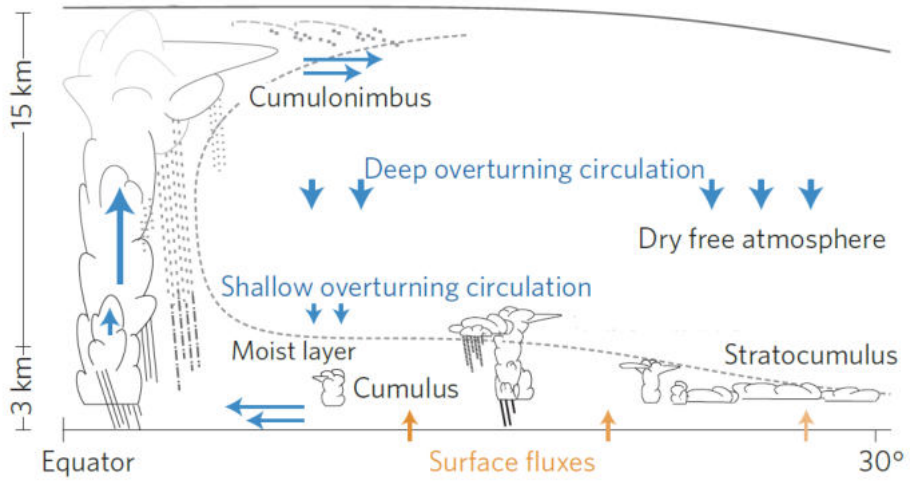

Figure 1.1: Tropical cloud circulation and interaction of shallow convective clouds to remote deep convection. Figure adapted from Bony et al. (2015).

Since shallow low-level clouds are ubiquitous over the ocean where ground-based observations are poor (Brueck et al., 2015), cloud remote-sensing is required. From satellites, however, this is complicated as these clouds exhibit sizes ranging over several orders of magnitude (Zhao and Girolamo, 2007). For common satellite-based spatial resolutions > 250 m, processes stemming from small and omnipresent sub-scale clouds are supposed to have far-reaching impacts. Satellite-based cloud cover which itself depends on the measurement resolution frequently reveals discrepancies to the actual cloud scene in shallow convection (Koren et al., 2008). Using higher resolved satellite measurements (spatial-resolution of 15 m) from the Advanced Spaceborne Thermal Emission and Reflection Radiometer (ASTER) and covering even small clouds, Zhao and Girolamo (2007) provided a comprehensive statistical overview of the macrophysical properties of trade-wind cumulus clouds over the western Tropical Atlantic. This increasing knowledge emerges in more comprehension of the complexity of these clouds. Such observations show that clouds are subject to much higher variability than archetypical clouds considered in LES. Most of the satellite observations, however, are still inadequate to detect sharp water-vapour gradients (Chazette et al., 2014). This emphasises the importance of additional field studies.

Much of current knowledge on marine low-level clouds over the Tropical Atlantic still stems from a few early field campaigns. Within the past decades, two of the larger field studies that have been conducted within regions of shallow convection are the Atlantic Tradewind EXperiment (ATEX) in 1969 (Augstein et al., 1974) and the Rain in shallow cumulus over the ocean experiment (RICO) in 2005 (Rauber et al., 2007). Limited remote-sensing capabilities hampered the clarification of the coupling between the macrophysical cloud properties and the boundary layer (BL) conditions. One big

milestone has been achieved with the establishment of Barbados Cloud Observatory (BCO) in 2010 (Stevens et al., 2016), and the two aircraft campaigns Next-Generation Aircraft Remote Sensing for Validation Studies (NARVAL) I and II held in December 2013 and August 2016 and performed with the High Altitude and LOng Range Research Aircraft (HALO). These data provide high-resolution measurements of shallow low-level clouds upstream the trade winds, eastern of Barbados.

In observing the clouds, the research focus today is shifting from mere limitation of uncertainties in climate cloud-feedbacks to the coupling of cloud-related properties with the BL conditions, which is presumably underestimated in climate models (Nuijens and Siebesma, 2019). The interplay between the predominant trade winds, cloud organisation, cloud geometries and precipitation in tropical low-level clouds forms a complex research field. It is widely examined over several scales and follows several research questions; *How are individual clouds affected by the BL conditions? Which quantity affect macrophysical cloud properties the most and to what extent? Which role plays the large-scale circulation on cloud organisation?* Based on these questions, Mieslinger et al. (2019) expands the ASTER-based statistics from Zhao and Girolamo (2007) and links macrophysical cumulus cloud properties to typical trade-wind layer conditions, such as the easterly winds, trade inversion strength, subsidence rate or sea-surface temperature, which are gained from reanalysis data. Considering more than five million clouds, their study represents the largest observational framework of tropical shallow low-level cloud properties so far. The recent study of Stevens et al. (2019c) based on Moderate-Resolution Imaging Spectroradiometer (MODIS) points out the persistent value of investigating shallow clouds back-again based on trivial phenomenological approaches. Making use of the latest observational methods, macrophysical properties and geometries of clouds are still urgently required for an advance understanding of cloud-controlling processes and their impact on climate.

These complex interactions in shallow convection regimes, which lead to diverse findings in observations (Klein et al., 2018), emphasise the importance of observational frameworks characterising clouds and their environment simultaneously, such as given by the airborne cloud observatory HALO. With its unique payload, HALO demonstrates the power of advanced remote-sensing instrumentation to characterise marine shallow clouds and their interaction with the environment. NARVAL-II represents the first aircraft campaign over the Tropical Atlantic, that was equipped with the hyperspectral imager specMACS. This imager allows to detect clouds in the across-track field. The recently published cloud masks for specMACS, developed by Gödde (2018) and for the airborne cloud radar (Konow et al., 2019) from NARVAL-II deliver high-resolution data of tropical shallow clouds in three dimensions.

These datasets are prerequisite for this thesis. As an extension to Gödde (2018) and the HALO instrument-based intercomparison of cloud fraction (Pavicic, 2018), this thesis makes use of both cloud masks to further elucidate the capabilities of modern airborne remote-sensing in characterising geometries of shallow low-level clouds, which mainly comprise shallow cumulus clouds over the Tropical Atlantic during NARVAL-II. The released dropsondes supply an observational-based realisation of the trade-wind BL conditions and thus represent a major benefit compared to the study of Mieslinger et al. (2019). Inspired by the general concept of Stevens et al. (2019c), cloud geometries are investigated in view of typical cloud shape descriptions. Since Mieslinger et al. (2019) identified the trade winds and especially the surface wind speeds as the most powerful cloud-controlling factor, the thesis investigates, if the dominant interactions between tropical shallow clouds and the trade winds similarly appear within individual cloud characteristics from NARVAL-II. Correspondingly, the following section reviews the cloud-controlling role of the trade winds.

1.2 The Trade Winds as Cloud Controlling Factor

Better understanding the influence of so-called cloud controlling factors (Siebesma et al., 2009) on cloud properties developed to a fundamental research aim (Klein et al., 2018). It conceives to identify the exterior factors relevant for cloud properties and to determine their magnitude. In doing so, cloud properties in future climate may be inferred from the changes of the cloud-controlling factors with rising global temperature. Observed relationships between shallow low-level cloud amount and controlling-factors are used to predict how low clouds will change in future climate, based on GCM-predicted tendencies of cloud-controlling factors.

The trade winds play a key role, as they transport relatively dry air towards the equator and thereby induce evaporation over the oceans leading to cloud formation above the lifting condensation level (LCL). From observational studies, Klein (1997) depicted low-level marine cloud amount within the tropics to be positively correlated with wind speed and surface-wind stress. His effort is supported by Brueck et al. (2015) using satellite observations from the MODIS, which revealed wind speed having the best correlation with monthly-mean low-level cloud amount in the North Atlantic Trades. Observations from the RICO campaign suggest that wind speed and subsidence regulate BL humidity and thus cloudiness and rainfall variability (Nuijens et al., 2009).

From LES simulations of idealised non-precipitating shallow cumulus clouds, Nuijens and Stevens (2012) discovered that the trade-wind layer becomes deeper at stronger winds. Aligned with larger moisture fluxes and smaller heat fluxes, shallow cumuli also become deeper. This deepening is a required response to contradicting effects of the enhanced fluxes arising in the sub-cloud layer and is explained by simple bulk concepts: While thermodynamically a moistening of the sub-cloud layer, resulting from increasing wind speed, tends to lower cloud base height (CBH), increases in surface and buoyancy fluxes dynamically tend to raise CBH. In order to adjust a new equilibrium, the layer has to deepen, enabling larger and deeper clouds to form. Furthermore, stronger winds correlate with stronger wind shear. The deeper the clouds are, the stronger the effects of the vertical wind profile. Vertical wind shear enhances the projected cloud cover as deeper and larger clouds get tilted with height (Neggers et al., 2003).

Since BL interactions are quite various, the wind field does not represent an alone-standing factor. The deepening of clouds produces more precipitation, whereby additional effects on cloud geometries become relevant which are neglected in the idealized study of Nuijens and Stevens (2012). Bretherton et al. (2013) similarly finds larger clouds with increasing wind speed, but a limited variation of BL depth, in the case of permitted precipitation. Precipitation also triggers gust fronts of upper-level cold air by partial rain evaporation, denoted as cold pools, which discourage further surface-based convection in the environment. Edges of precipitating shallow cumuli propagate faster than the low-level wind blows and similar to the propagation speed of the associated cold pool outflow (Zuidema et al., 2012). Cold pools are therefore considered to be responsible for the observed arc-shaped organisation of precipitating shallow cumuli. The role of precipitation on shallow cloud organisation is relevant, as the dry-out of the environment lead to moist domains of cloud clusters. Hence, organisation amplifies if clouds precipitate more (Vogel et al., 2016). In turn, Bretherton and Blossey (2017) pointed out that shallow convection appears to spontaneously develop and aggregate in clusters, even if precipitation is suppressed. Thus, cloud organisation in shallow convection describes one important domain within the role of cloud-controlling factors such as the wind field and, related to precipitation, influences mesoscale cloud patterns, e. g. elongated wind-parallel cloud streets, or even cross-wind cloud bands.

While Mieslinger et al. (2019) highlights the low-level trade winds, and especially the low-level wind speed, as the major driver on macrophysical cloud properties, the role of wind shear is considerably weaker. There are signs that wind shear acts as a limiting factor on cloud depth with increasing wind speed (Helfer et al., current research). Regarding cold pool dynamics, wind shear determines regions where precipitation falls and evaporates (Li et al., 2014). However, wind shear is a poorly observed quantity over the ocean which impedes its classification as individual cloud-controlling factor.

1.3 Thesis Outline

Investigating the geometries of shallow low-level clouds from airborne measurements during NARVAL-II, the remainder of this thesis encompasses the following topics: Chapter 2 gives an overview of performed flights and the instrument payload aboard HALO and focusses on the principles of the used cloud-detecting devices, namely the radar and specMACS. From those, cloud masks have been created in advance of the thesis being prerequisite for the further analysis. Based on their cloud mask products, suitable flights with simultaneous data are identified and the meteorological scenery is briefly described. Chapter 3 characterises the methods applied to the cloud masks in order to obtain horizontal geometrical cloud properties. It focusses on the coordinate transformation of the specMACS data that is based on a synergy with the radar data, describes the necessary assumptions and explains resulting uncertainties. Required adaptations to the datasets as well as occurring problems are described qualitatively. Chapter 3 introduces the question *What are the new capabilities of two-dimensional (2D) airborne-based observations by specMACS compared to the radar regarding cloud geometries?*

In addition to answering this question, Chapter 4 investigates the single cloud geometries. This chapter analyses the macrophysical cloud properties in two categories pursuing the questions *are the macrophysical properties of tropical shallow low-level clouds consistent with previous satellite-based statistics* and whether *simple shapes can well represent complex cloud structures.* Chapter 5 views the coherent cloud field geometry and examines the horizontal distribution of the clouds in order to respond: *Can cloud organisation phenomena be identified from specMACS? Does the spatial arrangement of the shallow clouds reveal certain patterns?*

Since the shallow low-level clouds underly easterly trade winds, Chapter 6 investigates the trade wind impact on cloud geometries. Motivated by Mieslinger et al. (2019), it examines *to what extent do the trade winds represent a controlling-factor on the geometries of shallow low-level clouds.* Chapter 7 specifies the robustness of the results and the magnitudes of uncertainties concerning main sources of error. Improvements focussing on an algorithm distributing nadir cloud information from the radar to the across-track pixels of specMACS are outlined. Chapter 8 summarises the findings of the thesis and provides an outlook referring to the aircraft campaign Elucidating the role of clouds-circulation coupling in climate (EUREC^{4}A). It sketches the capabilities of EUREC^{4}A to further investigate the cloud-circulation coupling of shallow low-level clouds over the Tropical Atlantic regarding the precedent research questions.

2. Datasets from NARVAL-II

This chapter introduces the airborne measurement devices established during the NARVAL-II campaign. Those devices and their measurement data products, i. e. their cloud masks, that are used for the analysis of tropical marine low-level clouds within this thesis are depicted in more detail. First, an overview of the research flights (RFs) from the NARVAL-II campaign is given and the measurement instrument configuration on the research aircraft HALO is listed. Based on this, the Sections 2.2 to 2.4 deepen the devices, which data products are used within this thesis.

2.1 Airborne Measurements

NARVAL-II was performed in August 2016 as a follow-up of the NARVAL-I campaign which was conducted in December 2013. Both campaigns started from the Grantley Adams International Airport on Barbados and deliver a tremendous meteorological dataset at the edge of the ITCZ and the Northeast Atlantic trade winds which benefits from HALO's high cruising level and long range (Krautstrunk and Giez, 2012). NARVAL-II aims to contribute to a better understanding of the coupling between marine tropical clouds and meteorological characteristics within the BL on various scales.

2.1.1 Research Flights (RFs)

During NARVAL-II, ten research flights were performed in deep and shallow convection regimes. Table 2.1 the specifications of the research flights of NARVAL-II together with a brief description of the predominant meteorological conditions and the main scientific purpose of the flights. Apart from the quality assessment of airborne measurements, one additional purpose of the NARVAL-II flight campaign was the satellite validation by collocating their satellite products with airborne measurements during the satellite overpass (Ewald et al., 2019). These satellite overpasses are not specified further in Table 2.1 as they are beyond the scope of this thesis.

Table 2.1: Synopsis of RFs from NARVAL-II in August 2016 based on the flight reports. The time is given in Coordinated Universal Time (UTC).

RF	Date	Flight Time (UTC)	Brief Description
01	08.08	08:22-18:59	Transfer flight from Germany.
02	10.08	11:53-20:47	Crossed the ITCZ flow, cyclic flight tracks, was performed for cloud statistics.
03	12.08	11:43-19:37	Cyclic flight tracks to check the methodology of measuring vertical velocity with dropsondes and mattress flight pattern in very dry atmospheric conditions.
04	15.08	11:49-19:46	ITCZ was crossed several times in ZigZag flight tracks, performed in shallow and deep convection regimes.
05	17.08	14:48-23:07	Cloud statistics with focus on cirrus clouds, flight tracks adapted to satellite overpasses, high cruising level above 12,000 meters in 75 % of flight time. Shallow convection at the beginning and high cirrus cloud fraction in moist air during high cruising level.
06	19.08	12:29-20:53	Circle flight pattern similar to RF03 to estimate wind divergence surface turbulent fluxes in shallow convection regimes, also some clear sky areas.
07	22.08	11:17-20:58	Closer to ITCZ in deep convection area with larger flown circles, high cloud fraction in all levels.
08	24.08	12:43-20:55	Deep convection observation western of hurricane Gaston in the dry inflow region, flight tracks in arch and circle shapes, most low level clouds at the edges and mid-level clouds in the vicinity of Gaston.
09	26.08	13:44-20:54	South of hurricane Gaston in shallow convection cloud regime, gradients from dry and shallow convection to congestus convection in moist layer, cross flight patterns.
10	29.08	09:44-19:00	Ferry transfer flight. Circles close to Madeira.

2.1.2 Instrumentation Payload on HALO

During the NARVAL-II campaign, the payload on the research aircraft HALO, a Gulfstream G550, consisted of a set of several remote-sensing devices. Active and passive sensors measured radiative fluxes in different ranges of the electromagnetic spectrum. Figure 2.1 illustrates the sensor configuration on board of HALO. Most of the measurement instruments were mounted in the belly pod below the front part of the fuselage. Only two devices, namely SMART and specMACS were mounted in the rear part of the aircraft. They were installed close to the launcher of the dropsondes, providing in-situ measurements of the vertical atmospheric profile. In the following, the installed sensors on board of HALO, shown in Figure 2.1, are briefly listed:

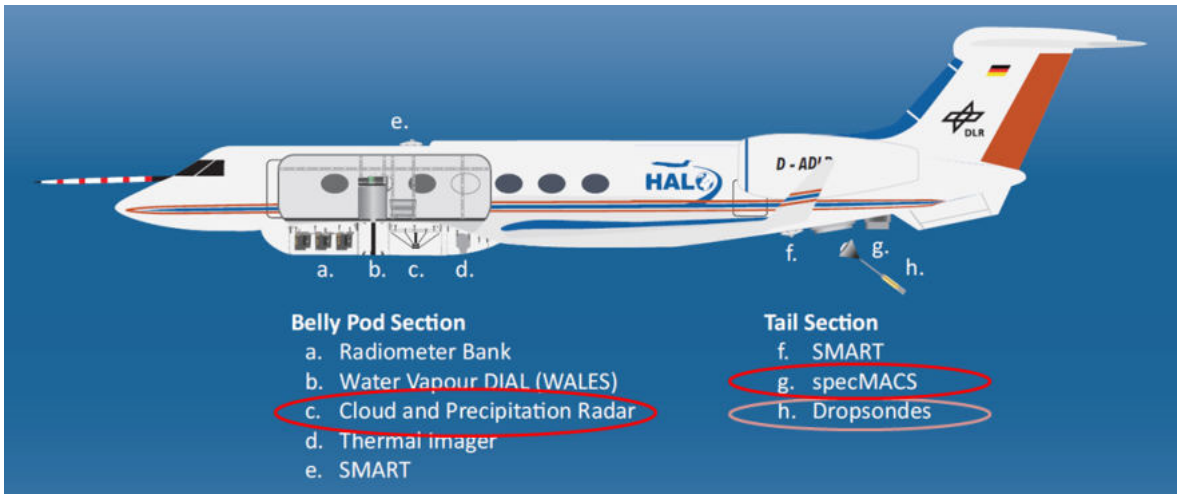

Figure 2.1: Cross-section of HALO showing all mounted devices during the NARVAL-II campaign. Figure adapted from Stevens et al. (2019a). Data used within the thesis is circled. Dark red circles represent the used devices providing cloud masks, whereas the dropsondes are used to examine the vertical atmospheric characteristics within the BL.

Radiometer Bank:

Three downward-pointing radiometers passively measure incoming radiation in 26 channels within the microwave spectrum, probing two water vapour and two oxygen absorption bands and several window channels in accordance with several satellite-based instruments in a time resolution of 1 s. The configuration allows the distinguishment between condensate phases and profiling of the quantities, as channels can be inferred to different heights (Konow et al., 2019).

Cloud and Precipitation Radar:

One active instrument component on HALO is given by the nadir-looking microwave cloud and precipitation radar MIRA-35, allowing to measure the droplet-based reflectivity and reflectivity-weighted Doppler velocity in the Ka-Band by penetrating atmospheric columns even under heavy precipitation. It has a time-resolution of around 1 Hz, comparable to that of the radiometer (Mech et al., 2014).

Water Vapour DIAL (WALES):

The multi wave-length water vapour differential absorption LiDAR operates in four wavelengths in order to vertically profile water vapour mixing ratio. Together with two aerosol channels, measurements with a vertical resolution of 15 m are possible in a frequency of 1 Hz (Wirth et al., 2009).

Spectrometer of the Munich Aerosol Cloud Scanner (specMACS):
SpecMACS is a passive imager, measuring in the near-infrared and visible spectra by two camera systems. Covering a field of view (FOV) of more than 30° with 1312 pixels in the visible spectrum and 320 pixels in the shortwave infrared (SWIR) spectrum, specMACS provides across-track detection of clouds in a range of more than 8 km when the flight altitude of HALO is roughly 15 km (Ewald et al., 2016).

Spectral Modular Airborne Radiation Measurement System (SMART):
SMART serves as a spectral irradiometer for downwelling and upwelling radiation in the SWIR spectrum in a time-resolution of 0.5 - 4 s (Wendisch et al., 2001).

Thermal Imager:
Within the belly pod of HALO, one section is reserved for the mounting of a thermal imager. During NARVAL-II, however, no thermal imager was installed – a shortcoming that will be changed in future flight expeditions (Stevens et al., 2019b).

Dropsondes:
During the campaign, HALO was able to load up to 70 dropsondes per flight that were released during the flights. This way the data of up to four falling dropsondes could be recorded simultaneously. During their fall, dropsondes profiled atmospheric conditions (Busen, 2012).

Regarding the analysis of cloud geometries and their coupling with the predominant wind field, the following sections of Chapter 2 describes the data of the cloud and precipitation radar and specMACS in more detail. They specify the characteristics of both devices and of their respective cloud masks, being prerequisites for the analysis.

2.2 Measurements from the Cloud and Precipitation Radar

Airborne radar systems have been used extensively for decades in the context of cloud-related research purposes (e.g. Mapes and Houze, 1995). Infiltrating the clouds, radar measurements enable vertical cloud structures to be obtained, so that these measurements still represent a fundamental component of airborne cloud analysis. The airborne cloud and precipitation radar mounted on HALO is specified in the following.

2.2.1 Instrument Characteristics

The cloud and precipitation radar is a MIRA-35, manufactured by METEK GmbH. It is a monostatic, pulsed and magnetron Ka-band Doppler radar operating in 35.5 GHz within the water-vapour window and facing downward from HALO. The two receivers provide a co- and cross polarisation channel. The output, having a data sampling of 1 Hz, mainly comprises the radar reflectivity , the Doppler spectra and Doppler velocity, the spectral width and the linear depolarisation ratio (LDR). The raw measurements are provided in a vertical resolution of 28.8 m. For typical cruising levels at 13 km, performed during the NARVAL, and a typical aircraft speed around 200 m/s, the sensitivity of the radar is $\approx$ 30 dBZ and the footprint size is $\approx$ 130 m. In the along-track distance, clouds are resolved at roughly 200 m (Mech et al., 2014).

The radar is part of the HALO Microwave Package (HAMP), consisting of two nadir-pointing instruments: firstly, the MIRA-35 cloud radar and secondly, the radiometer bank composed of passive microwave radiometers with 26 frequencies in bands ranging from 22.24 to 183 GHz. The data can be accessed from the freeware Climate and Environmental Retrieval and Archive (CERA) database (Konow et al., 2018). Within the CERA platform, the data is regridded in a unified grid, having a vertical resolution of 30 m and a time resolution of 1 Hz. Doppler velocity measurements were strongly affected by aircraft motion and are not provided in the unified CERA dataset (Konow et al., 2019), which is unproblematic for the macrophysical study in this thesis.

2.2.2 Radar Cloud Mask Product

From the radar measurements provided in the unified grid, a cloud mask has been created previous to this thesis by Heike Konow (Meteorological Institute, University of Hamburg). The radar cloud mask was derived from the measured radar reflectivity. Since the radar signals within the CERA platform are already filtered, i.e. adjusted for the constant background noise, the remaining detected signals represent clouds. As soon as a measured reflectivity value is available, the pixel is assigned as cloud (value of 1) in the cloud mask, otherwise the clear pixel has the value 0. In addition, the cloud mask was further processed by interpolating measurement gaps and morphologically closing the clouds. In the case that two clouds were measured very close to each other (around 1 s $\approx$ 200 m), they are connected. This is exemplarily shown in Figure 2.2 for one shallow cloud case during the NARVAL-II campaign. The reason for the closing of gaps is, that small cloud fragments often belong to larger adjacent clouds which could not be resolved by the radar (Konow et al., 2019).

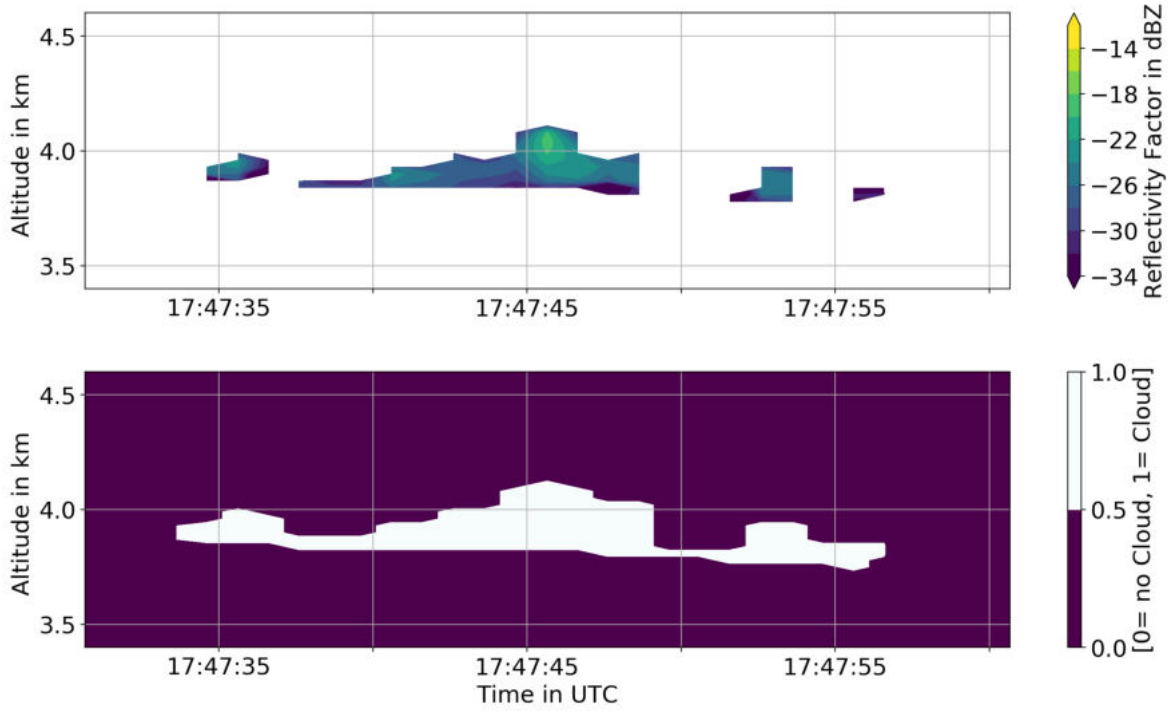

Figure 2.2: Radar reflectivity factor in dbZ of captured shallow clouds during RF07 (upper panel), together with the corresponding cloud mask (lower panel) where the morphological closing was applied to eliminate small cloud fragments and to connect them with corresponding larger clouds.

2.3 Measurements from specMACS

The upcoming sections further specify the hyperspectral imager specMACS which represents the major component for the cloud analysis in the scope of this thesis.

2.3.1 Instrument Characteristics

SpecMACS was developed at the Meteorological Institute of the Ludwig Maximilian University (LMU) in Munich and measures solar radiation in the 400-2500 nm wavelength spectra with the purpose to observe cloud and aerosol optical properties, as well as aerosol tracers. This is done using two hyperspectral cameras. These cameras are line-scanning slit spectrometers that capture the cloud scenery in two dimensions – spatial and spectral. One camera covers the visible and near infrared spectrum (VNIR) wavelength spectrum (400-1000 nm). The second camera measures in the shortwave infrared (SWIR) spectrum in the range of 1000-2500 nm. In a first step, the incoming light rays are spatially filtered by a slit and are subsequently divided by a holographic grating. The VNIR camera has a typical spectral bandwidth in the range of 2.5 and 4 nm, whereas the SWIR camera has a spectral bandwidth in the range of 7.5 and 12 nm (Ewald et al., 2016).

The following specifications focus on the SWIR camera, as the VNIR camera is not used in this thesis. During NARVAL-II, specMACS was mounted on the research aircraft HALO facing downward. The SWIR camera passively measures reflected sun light in 320 spatial pixels and in 256 wavelengths and thereby detects clouds. The instrument characteristics allow the observation of the across-track field in a FOV of 35.5°. The cloud-scanning during flight is hence composed of two dimensions. Since the aircraft overpasses the clouds underneath, clouds can then be detected in the along-track and across-track perspective. For a typical cruising altitude of 10 km, the FOV corresponds to an across-track viewing distance of around 6.4 km. Measuring at this cruising level with a frequency of 30 Hz, the geometrical spatial resolution of one pixel is roughly 18 m along and 38 m across the flight track (Gödde, 2018). Further technical details on the measurement principles of specMACS, concerning the spectral response and noise behaviour, can be found in Ewald et al. (2016).

For a better understanding, Figure 2.3 illustrates the measurement spectrum of the SWIR camera, covering 256 wavelengths. The graph shows the time-averaged SWIR measurement values from three marine cloud scenes on RF04 during NARVAL-II. The depicted cloud scenes are representative for the entire airborne measurement campaign as the spectra are based on one almost overcast, one partly cloudy and one cloud-free scene above the Atlantic ocean. All measurements were taken in a short time-range of five minutes, assuring almost homogeneous solar illumination, so that cloud-radiative impacts on the measured spectrum can be clearly identified. In the absence of disturbing solar reflectance from the ocean's surface, called as sunglint (Cox and Munk, 1954), the ocean is radiatively dark within the spectral range (blue-coded scene, Figure 2.3). The more clouds are present, the higher the reflection and the higher the radiation values measured by the sensors.

All spectra indicate the strong water vapour absorption lines around 1125, 1375 and 1890 nm. Within the SWIR spectrum, water vapour represents a radiatively active gas, having the strongest and broadest absorption bands located at about 1375 and 1890 nm, where almost no solar radiation reaches the instrument. Outside, the spectrum shows higher radiance values compared to the ocean when it is cloudy. The cloud surface reflects the incoming sunlight and thus raises the radiance values. Intuitively, a brightness threshold seems to be sufficient in order to distinguish between cloudy and clear pixels, collected in a cloud mask. However, the development of the specMACS cloud mask, established by Gödde (2018) from the Meteorological Institute of Munich, clearly required more effort due to the brightness dependency on Sun's position and the impact of sun glint. This is outlined in the following section.

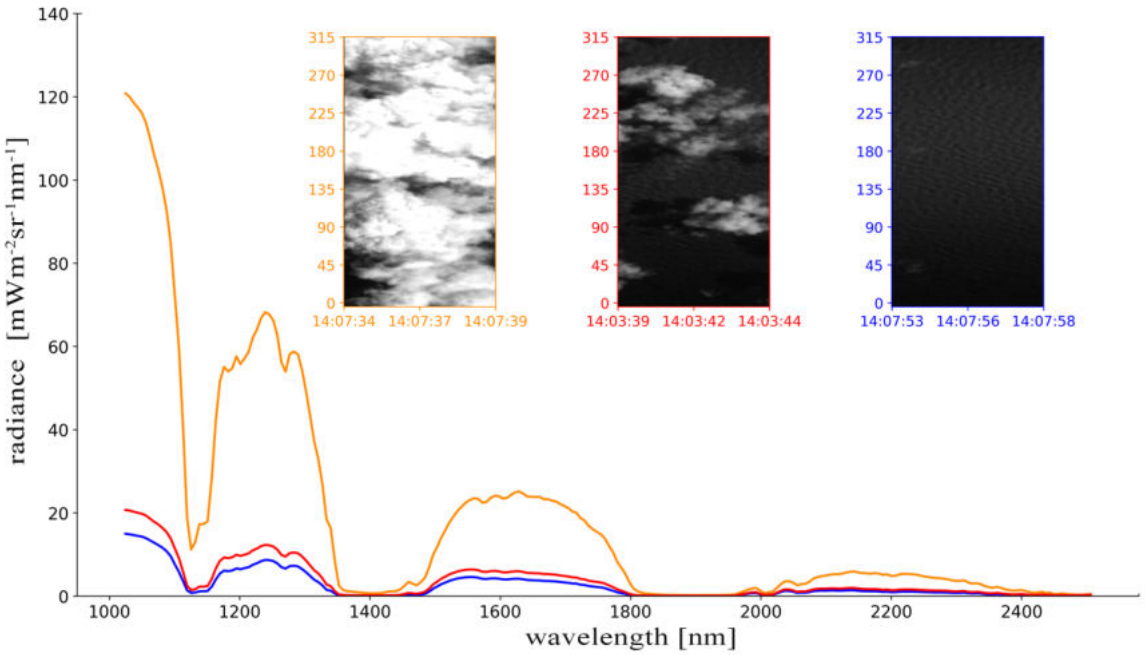

Figure 2.3: specMACS SWIR radiance measurement spectrum in $mW^{-2}sr^{-1}nm^{-1}$ for three different cloud scenes averaged in the across-track. These are depicted and colour-coded in the upper panels. For them, numbers of spatial across-track pixels are labelled on the y-axis. All measurement cases stem from a five minute time period on RF04.

2.3.2 specMACS Cloud Mask Product

To identify clouds from specMACS, the intuitive approach of brightness thresholds does not yield promising results. Various sources of disturbing processes affect the radiance values of each pixel. These are mainly the brightness dependency on the Sun's position and the presence of sunglint, meaning that the surface of the ocean can also significantly reflect the sunlight under specific conditions. Most of all, sunglint-contaminated pixels can have higher radiance values than cloud pixels. This section explains the processing steps from the specMACS raw data to the best estimate of a cloud mask (Figure 2.4), which were developed by Gödde (2018). The following paragraphs of Section 2.3.2 thereby summarise parts of the work from Gödde (2018).

From the raw data of the SWIR camera, in the form of digital numbers, pixels are calibrated to radiances. This calibration considers the corrections of the dark signals, the spectral transmittance of the aircraft window in front of the camera, damaged sensor pixels and the exposure time of the camera. The calibrated data is smoothed by a kernel 3x3 filter. For a first cloud mask estimate, the brightness threshold approach is based on the comparison of the measured spectrum and a simulated reference spectrum, neglecting molecular absorption.

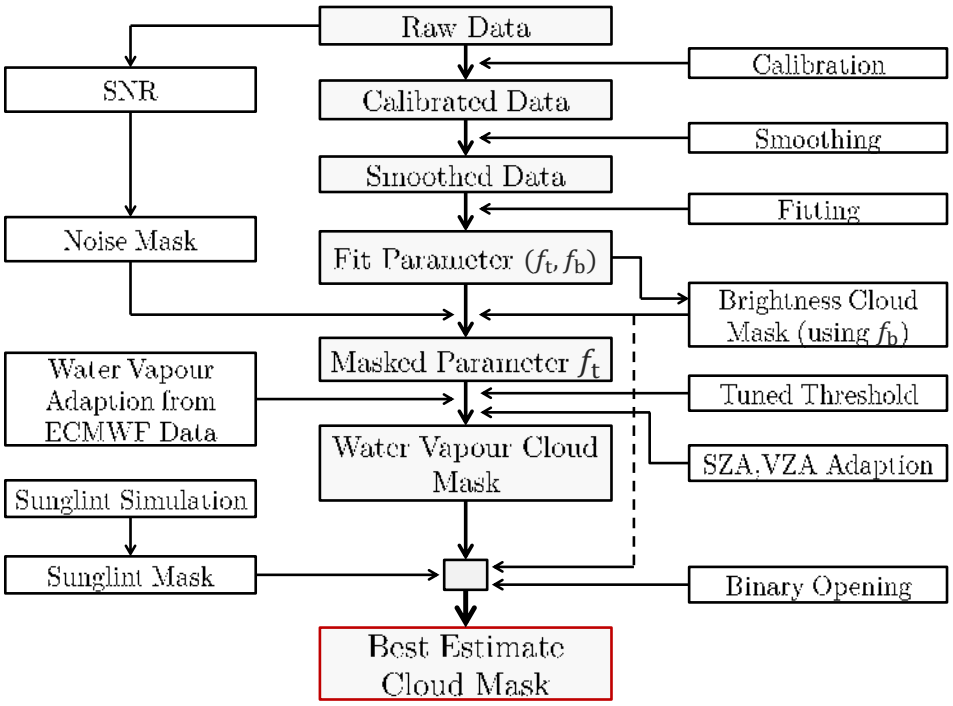

Figure 2.4: Sketch of the process steps and necessary components of the specMACS cloud mask. Figure redrawn and adapted from Gödde (2018).

From that, a least-square fit approximates the measured spectrum from the reference spectrum in a spectral range from 1015 and 1900 nm. In this fitting approach, one fitting parameter, here differently denoted as f_b is based on the brightness of the measured spectrum, whereas the second parameter, here f_t, depends on the spectral transmittance. Dark domains of the image are masked by a threshold of f_b. In addition, a noise mask aims to exclude last remaining dark pixels. The noise mask is based on the signal-to-noise ratio (SNR). However, the brightness mask together with the subsequent noise mask only provide a valid cloud mask in the absence of sunglint.

Small radiance differences at the edges of the water vapour absorption bands, caused by the shorter path of reflected sunlight when low-level clouds are present, can be detected from specMACS. Consequently, the best-estimate cloud mask includes water vapour absorption. Using the definition of the atmospheric optical thickness, the fitting parameter f_t can be set independently of the wavelength through mathematical simplifications. This fitting parameter, however, is dependent on the viewing zenith angle (VZA) of the camera and on the solar zenith angle (SZA) and thus tuned to the Sun's position. In addition, the threshold parameter depends on the water vapour amount that underlies high spatial and temporal variability. Reanalysis water vapour profiles from the European Centre for Medium-Range Weather Forecasts (ECMWF) are used to determine the impact of different water vapour contents on the fitting parameter. The adapted threshold of the fitting parameter represents a mathemati-

cal function of SZA, VZA and the integrated water vapour (IWV). Along the entire flight track and viewing area of specMACS, the sunglint is simulated for a constant wind speed of 5 m/s, containing the parametrisations of L. Tsang (1985). If the ocean reflectance is above a certain threshold, the water vapour cloud mask is preferred, otherwise the brightness cloud mask. Potentially false-detected cloud pixels are aimed to be identified with the aid of binary opening. From this, a best-estimate cloud mask is created. Further detailed specifications about the cloud mask algorithm and used thresholds values are mentioned in the master thesis of Gödde (2018). His cloud mask is accessible on the *macsServer* from the Meteorological Institute of the LMU (Kölling, 2020). The data from his cloud mask will be used in the following to analyse geometrical cloud properties.

2.4 Dropsondes

In the current state of art, the most accurate method to get vertical atmospheric profile data is given by sonde measurements. Whereas radiosondes are launched at fixed locations, being capable of rising above the troposphere, aircraft campaigns benefit from the fact that they can release dropsondes to get in-situ profiles of the atmospheric conditions underneath the aircraft during the flight.

The HALO payload allows to hold 72 dropsondes per flight. During the NARVAL-II campaign, 215 dropsondes were launched on 10 flights (Bony and Stevens, 2019). The released Vaisala RD94 dropsondes, further specified in Busen (2012), took vertical profile measurements of the standard meteorological parameters such as (temperature, humidity, pressure) wind speed and direction). As carried out by Wang et al. (2015), wide investigations of vertical wind profiles in tropical storms, using GPS dropsondes revealed the capability to derive the wind field from in-situ profiling sondes. Equipped with a GPS sensor, the Vaisala RD94 dropsondes can infer the horizontal wind speed and direction from the horizontal drift of during their fall. According to Stevens et al. (2017), measurement accuracy of the meteorological parameters pressure, temperature and relative humidity is 0.4 hPa, 0.2 °C and 2 % respectively. Wind speed values have an accuracy of 0.1 m/s. From the receiver, the signal data of up to four dropsondes can be recorded simultaneously. The dropsondes are equipped with a parachute in order to decrease the falling velocity. Typical fall periods during the NARVAL-II campaign were of about 12 minutes. Between the flights, the number of dropsonde releases was not equal as they depend on the scientific research motivation of every specific flight, the predominant weather conditions and also on restrictions of the air

traffic control. With 50 releases on RF03 and RF06, these two RFs had the highest number of dropsonde profiles. During both flights, HALO performed horizontal circular flight tracks of about 48-52 minutes in which more than ten dropsondes were released, in order to measure the large-scale vertical motion of airmasses (Bony and Stevens, 2019). During RF04, however, only ten dropsondes have been released. The first transatlantic transfer flight only consisted of nine launched dropsondes.

In this thesis, the raw dropsonde measurements, having a temporal resolution of 2 Hz, are not used but those from the unified grid of the CERA database (Konow et al., 2019), having a vertical resolution of 30 meters. This vertical resolution, which is equivalent to the radar reflectivity dataset and the corresponding cloud mask, guarantee the same reference coordinates when merging the outputs of the different measurement devices. The dropsonde data provides the essential knowledge of the wind field which is used for further investigation on how tropical low-level clouds interact with the trade winds. In particular, RFs with high-frequent releases allow representative temporal information on how the atmospheric wind field changed during one flight.

2.5 Combined Data Continuity during Research Flights

For the combined multi-sensor approach of this thesis, simultaneous measurements of specMACS and the radar are indispensable. The two transfer flights (RF01 and RF10) are excluded from the analysis, as most measurements were taken north of the tropics (north of 20°N). Furthermore, only two dropsondes were released over the tropical ocean during each flight. In addition, the radar was not operating from RF08 until the end of the campaign, so that those flights are not considered in the upcoming analysis. During the remaining flights, simultaneous cloud measurements were generally taken and several dropsondes launched. However, the individual flights do not always deliver continuous series of simultaneous measurements. Figure 2.5 illustrates the six flights during which all considered devices (specMACS, radar and dropsondes) were in operation. The periods in which radar and specMACS were measuring simultaneously and reliably are plotted as bold lines. In particular, when flights were performed on high cruising levels, the window in front of specMACS was partially severely affected by icing. This window-freezing prevents reliable cloud detection from specMACS and such measurements are useless. Decreasing the cruising level helped to prevent additional freezing in most of the cases. In addition some interruptions during these flights occured due to issues at the radar.

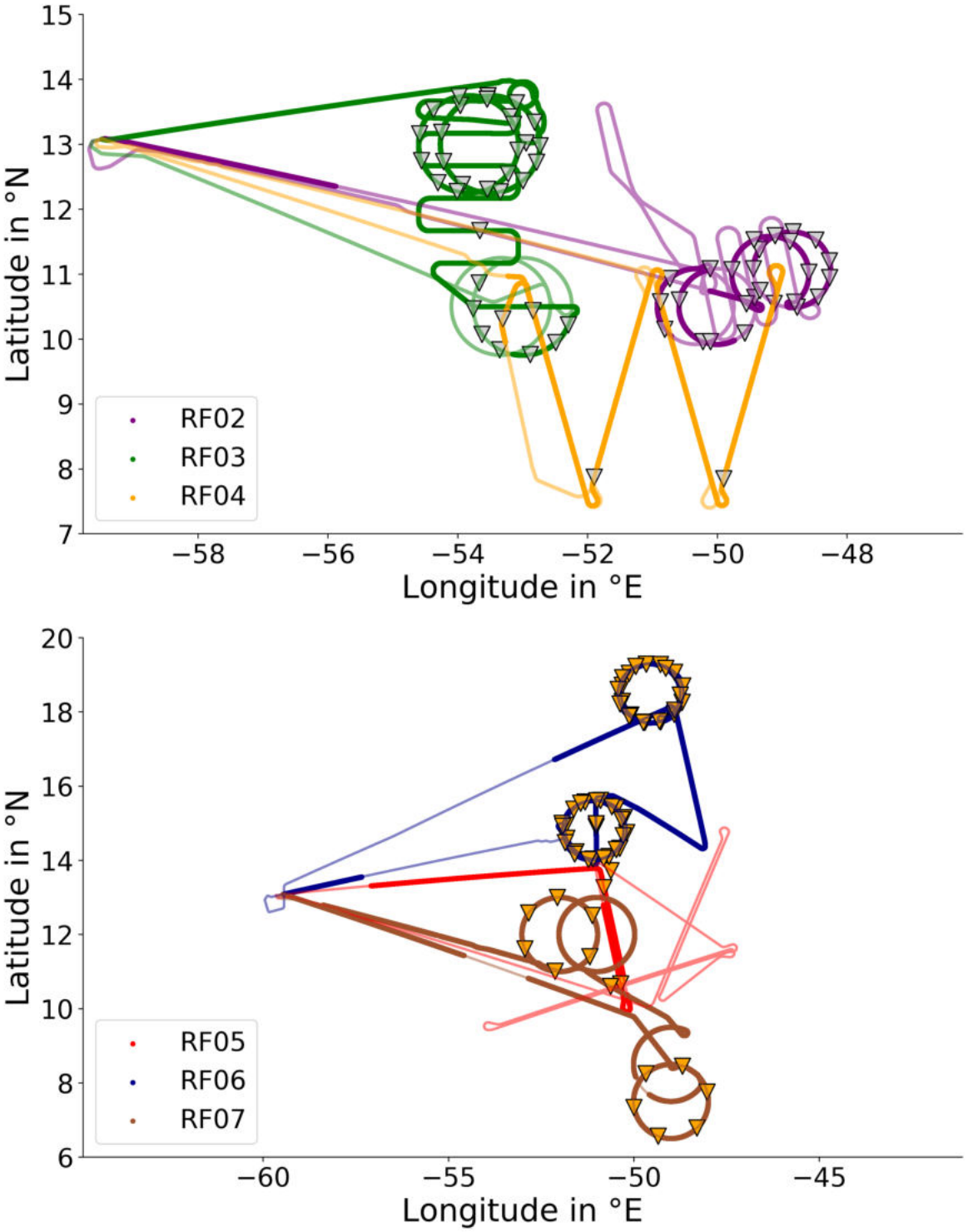

Figure 2.5: Map of flight tracks of the RFs during NARVAL-II, which are considered within the thesis. The periods in which both devices (radar and specMACS) were operating reliably and simultaneously are highlighted as bold lines. From all of the dropsondes, only those that are less than 15 minutes away from simultaneous measurements of radar and specMACS are indicated as triangles.

2.6 Tropospheric Vertical Profiles during NARVAL-II

Flights during NARVAL-II were partly performed in the vicinity of the ITCZ and partly more northern over the Tropical Atlantic (see Table 2.1) wherein shallow convection was more favourable and affected the vertical structure of the atmosphere. For the six considered RFs, indicated in Figure 2.5, tropospheric vertical profiles are illustrated in Figure 2.6 in terms of relative humidity (RH), wind speed and wind direction. The profiles result from the dropsonde measurements of each RF averaged over the height. Due to the interest of the thesis in low-level clouds, the profiles are only plotted up to an altitude of 8 km and described for the low-level and mid-level troposphere.

During RF03 and RF06 (first row in Figure 2.6), the lower troposphere consisted of a shallow BL, driven by the easterly trade winds. High SST together with the trades led to a moist lower BL in which shallow clouds were favourable. While, for both flights, vertical changes in wind direction were minor, as well as changes in wind speed up to 3 km, more intense vertical gradients in wind direction and higher wind speeds were recorded during RF04 and RF05. Regarding the wind speed, RF05 shows the highest intervariability of the dropsondes. RF02 and RF04 are characterised by a significant decrease in wind speed at altitudes between 1 km and 2 km.

For all flights in shallow convection, the low-level moist-layer, stemming from the marine BL, was mostly located up to an altitude of 1 km marking the estimated CBH. In particular during RF06, a sharp hydrolapse was found in around 2 km wherein the mean relative humidity decreased by 60 % in a few hundred meters. This dry-out was identified as the trade-wind inversion with the layer of shallow convection below in Bony and Stevens (2019). During RF03, an elevated moist-layer occurred and the relative humidity reached a maximum at an altitude of 4.5 km. Above 5 km, the atmosphere was very dry and apart from the profiles of RF07, relative humidity decreased strongly below 40 %. Deep convection during RF07 led to more moisture in the upper levels and weaker vertical gradients in relative humidity. Southern regions overflown by RF07 were characterised by south-westerly winds, affecting the mean value of the wind profiles. RF07 showed the lowest wind speeds with below 5 m/s in the lowest 3 km. Subsidence was quite similar during all flights and rather weak, as found by lower tropospheric stability values below 15 K for most of the time. Since NARVAL-II was performed during the wet season, IWV values up to 60 $\frac{kg}{m^2}$ were observed by Jacob et al. (2019a), distributed into two modes that resulted from the differently intense moist layers.

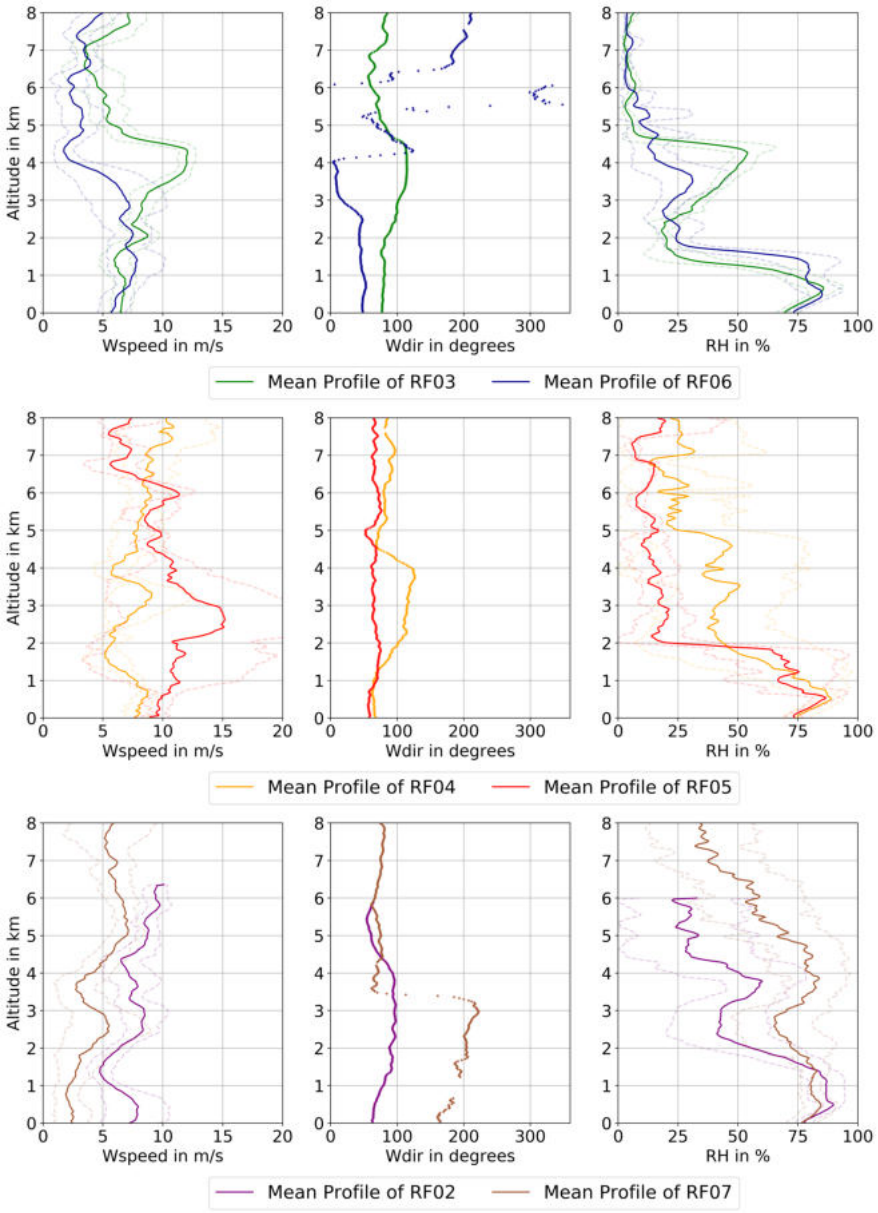

Figure 2.6: Mean vertical profiles of wind speed (Wspeed), wind direction (Wdir) and relative humidity (RH) from the dropsondes averaged over each of the chosen RFs. Flight days are divided into three groups with respect to their vertical tropospheric characteristics. Dashed lines show the intervariability of the profiles, calculated by the standard deviation.

This atmospheric state has a direct impact on the vertical cloud distribution which was sampled during NARVAL-II. Besides the IWV, Jacob et al. (2019a) investigated the vertical hydrometeor paths during NARVAL-II and compared them to those of the previous campaign NARVAL-I carried out during the dry season within a similar domain of the tropical atlantic. In their study, they found that cloud water content was relatively low during NARVAL-II. They suspected this to result from more effective precipitation and increased cloud organisation. As a supplement, Figure 2.7 depicts the vertical presence of clouds throughout the campaign, showing the vertical frequency distribution of cloud fraction captured by the cloud radar.

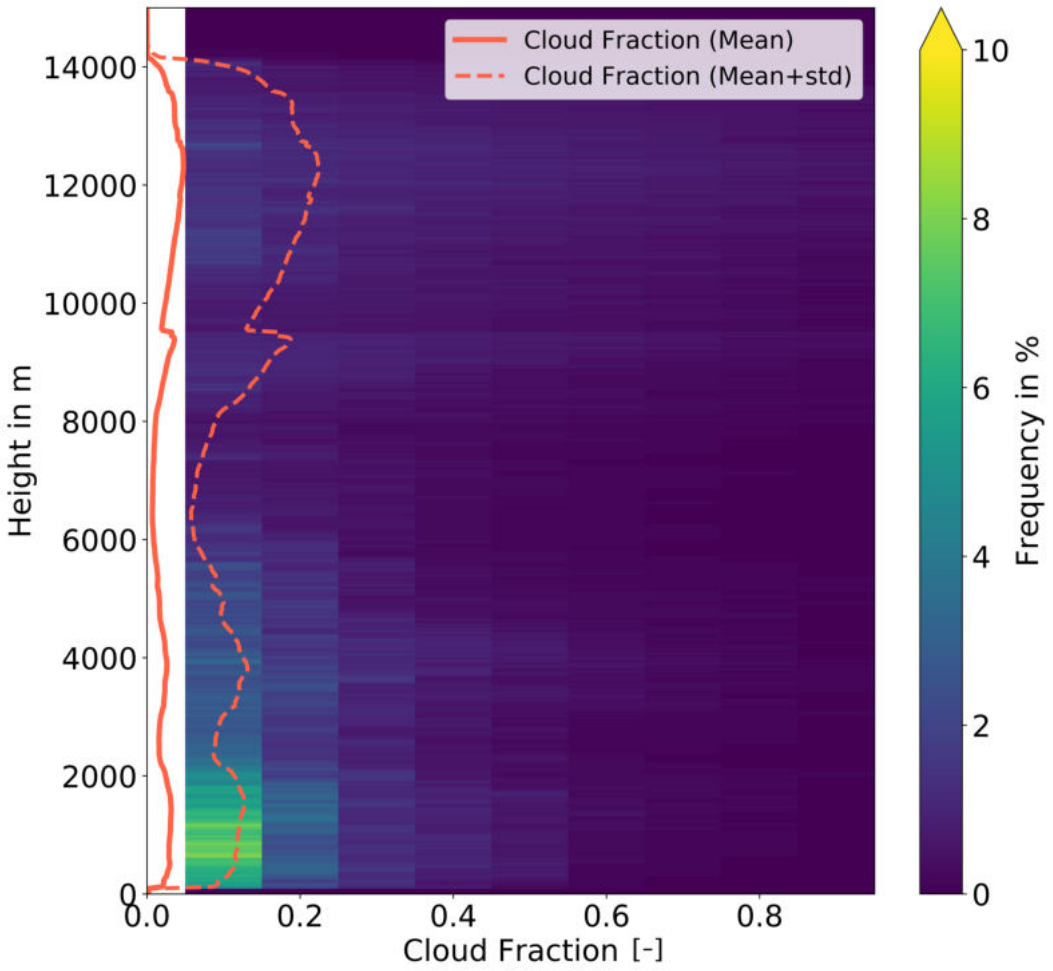

Figure 2.7: Vertical frequency distribution of cloud fraction based on 15-min averages, gained from the radar cloud mask during the considered RFs of NARVAL-II. Cloud fraction < 0.05 is excluded in the plot due to the high frequency of occurrence. Vertical mean profile and their standard deviation are depicted as red solid and dashed line, respectively.

In terms of the mean cloud fraction, the vertical profile of clouds is relatively constant and values are generally very low. In each height, the mean cloud fraction is below 5 %. If a significant amount of clouds were dominant (cloud fraction > 0.05), cloud fraction was mostly measured around 0.1 in the lower troposphere between 1000 m and 1500 m. This maximum in frequency of occurrence is related to the moist low-level BL (Figure 2.6), where broken shallow low-level clouds favourably form above the LCL. Due to the hydrolapses in the upper middle atmosphere (around 6 km), clouds are barely found in these levels. The standard deviation of cloud fraction also reveals a lower variability in the mid-levels compared to the low-levels.

However, high-level clouds, not included in the cloud liquid water investigation by Jacob et al. (2019a), were frequently observed during NARVAL-II. Both, mean cloud fraction and its standard deviation are considerably higher than in the mid-levels.

For this thesis, these high-level clouds are in turn disturbing, as they prevent passive devices from observing clouds in underlying layers. Instead, the shallow low-level clouds with cloud top height (CTH) below 3000 m represent the cloud type of interest for the scope of this thesis.

3. Methods of Cloud Analysis

This chapter presents the methods that are applied to the cloud masks from radar and specMACS to perform an analysis of cloud geometries. In that context, this chapter elaborates the role of the viewing perspective and resolution for further applications. Originally, both cloud masks are provided in aircraft aligned coordinate systems in which one axis is given by time in UTC. Regarding the radar, the second axis describes the vertical dimension which is measured in meters and consists of a resolution of 30 m (Section 2.2.2). Regarding specMACS, however, the second axis consists of across-track pixels and is not provided meter-based coordinates. For a cloud geometries analysis, a coordinate system with both axes in meters is essential though. Thus, the specMACS cloud mask data requires additional post-processing. Moreover, simplifications of cloud shape help to compare cloud fields and cloud structures in different BL conditions such as variable wind fields. These methods are fundamental for the subsequent chapters.

3.1 Cloud Labelling in the Cloud Mask

First, the geometrical cloud analysis requires clouds to be individually analysed in the cloud mask. Single clouds have to be identified as coherent objects. Previous to this thesis, this identification was already achieved for the radar cloud mask by Konow et al. (2019), through a connected component analysis. Basically, each cloud-pixel is connected to its neighbour cloud-pixels, to consider them as a coherent object, i.e. a single cloud. From the eight-connectivity algorithm (Rosenfeld and Kak, 1982), the neighbouring cloud-pixels are considered as coherent when they are connected on one of their edges or corners. Pixels can thus be connected horizontally and diagonally. In addition to four-connected pixels in which cloud-pixels, having the coordinates $(x \pm 1, y)$ and $(x, y \pm 1)$, are connected, diagonal pixels with $(x \pm 1, y \pm 1)$ are merged. While the algorithm is based on the along-track and the vertical dimension for the radar, it is here applied to the along-track and across-track direction of specMACS using the Python package *skimage*. Each cloud is labelled with an identification number (ID). Figure 3.1 shows an exemplary short scene from RF06 of overpassed shallow clouds.

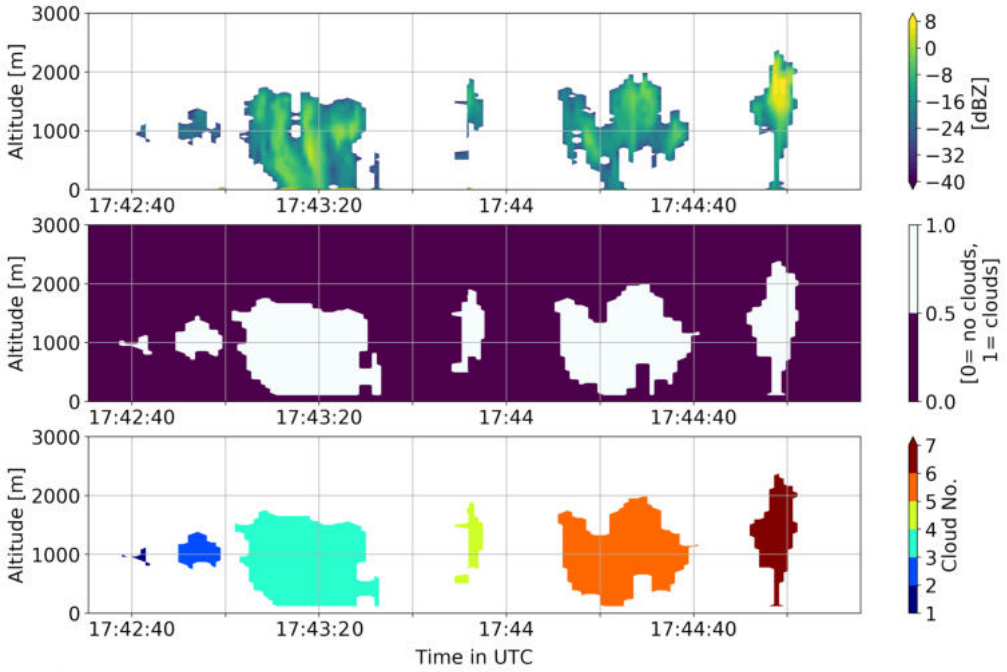

(a) radar

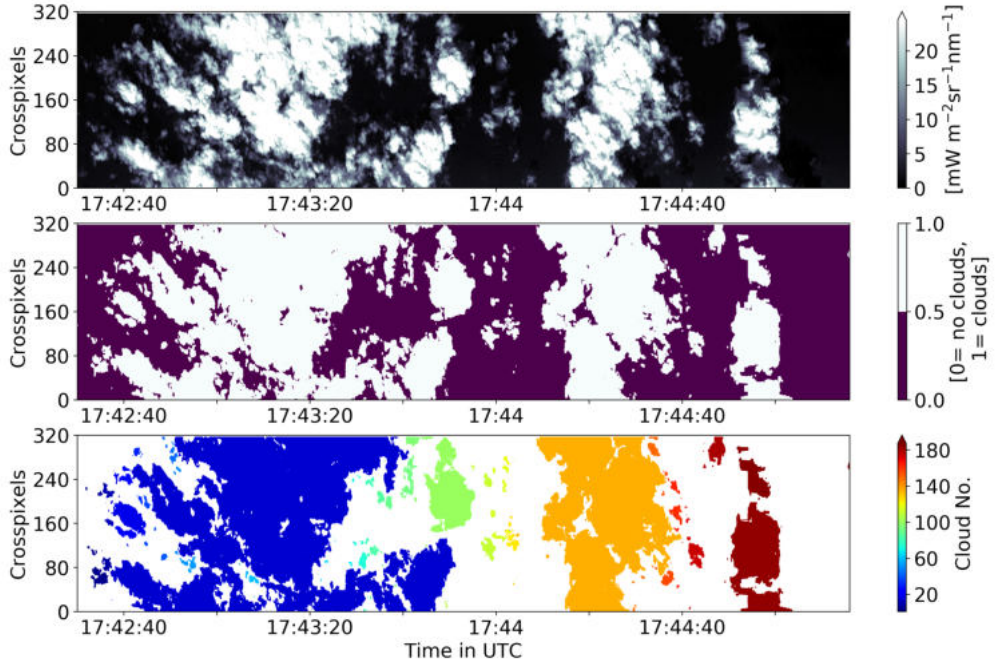

(b) specMACS

Figure 3.1: Cloud scene during RF06 from 17:42:30 to 17:45:15 UTC as seen from the radar (a) and from specMACS (b). The upper panel of each device shows measurements of the cloud scene, namely the reflectivity factor in dBZ, regarding the radar, and radiance measurements of the 1600 nm channel from the SWIR camera for specMACS in mW $m^{-2}sr^{-1}nm^{-1}$. The corresponding cloud masks are shown in the middle panel for the radar and specMACS respectively. The lowest panels indicate the number of clouds based on their IDs from the connected-component analysis of the given cloud scene, from the radar and specMACS respectively.

For the scene in Figure 3.1, the radar data clearly indicates precipitating shallow clouds within the considered time period, as the measured radar reflectivity partly reaches down to the surface. Comparing the reflectivity to the colour-coded cloud IDs, the morphological closing for the radar data becomes visible. During the depicted period, the connected-component analysis displays seven clouds. The two-largest precipitating clouds extend over the entire across-track FOV of specMACS.

Considering the along-track axis, it is notable that specMACS detects more than one hundred clouds in the time-period of less than three minutes. The high resolution of specMACS enables a precise detection of the cloud field so that even small cloud structures can be distinguished from the rest of the cloud field. Moreover, several clouds that do not extend into the FOV of the radar are additionally captured. However, the vertical information for the clouds underneath the aircraft, obtained from the radar, represents an essential additional degree of information, not provided by specMACS. Even though both devices measure the same cloud scene, they reveal different cloud conditions and information. Consequently, merging the individual cloud information from both devices based on the cloud IDs is by no means trivial.

3.2 The Role of the Field of View and Resolution

In order to merge cloud information from both devices, radar and specMACS, it is necessary to consider the different viewing directions and FOVs. Figure 3.2 provides an overview of the viewing fields of the devices, installed at HALO during the NARVAL-II campaign. For the sake of this thesis, the focus is on the radar and specMACS. The given angles were empirically determined from T. Koelling et. al. by visual inspection of the measurement products.

The nadir of HALO, with regards to the radar, lies in the origin of the coordinate system. Compared to the origin, and thus the FOV of the radar, the specMACS across-track axis looks ahead of the radar by 2.6°. The central spatial pixel of specMACS is shifted by 0.55° to the left in flight direction. The pixel-based across-track FOVs from specMACS overlap. Due to the different viewing angles, the detection of the same cloud underneath the aircraft takes place at different timestamps on both devices, radar and specMACS. Therefore, the cloud-analysis requires a time-shift to be applied to the datasets. This time-shift is based on a simplified method from Pavicic (2018), considering the distance d between HALO and cloud as well as the ground speed v.

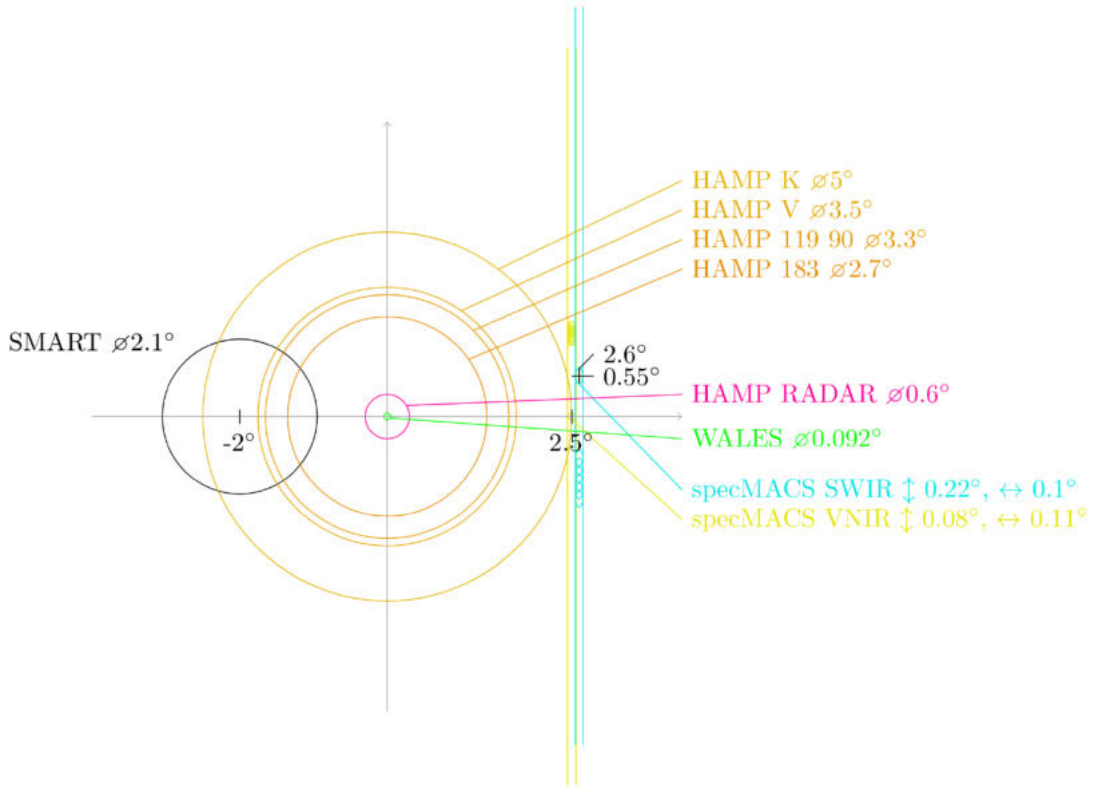

Figure 3.2: Viewing direction and FOV of the measurement devices mounted on HALO during the NARVAL-II campaign. Image courtesy of T. Kölling.

This approach is sketched in Figure 3.3. The distance d between HALO and the cloud underneath the aircraft is obtained using the flight altitude data from the Basic Halo Measurement and Sensor System (BAHAMAS) and the measured CTH from the radar. The horizontal distance Δx of HALO between the cloud-detection from specMACS and from the radar is calculated using the tangent of the viewing angle of specMACS and the distance d. Considering the ground speed v of HALO which is approximated to be constant in this short period, the time-shift Δt can be calculated following the speed-time law. Hence, both devices see the cloud at the same timestamp.

However, when combining cloud information frow two cloud-detection devices, the effects of the different device-specific sensitivities and resolutions on the cloud masks are far-reaching and have to always be kept in mind. Concerning the device-specific sensitivity, a highly-sensitive device labels a pixel as cloudy sooner than a low-sensitive device. Pavicic (2018) points out this essential role of sensitivity for cloud detection from HALO through a comparison of cloud fraction during NARVAL-II between the devices, introduced in Figure 2.1. It is very complicated to infer the real cloud that is hidden behind the cloud mask. Furthermore, Zhao and Girolamo (2006) and Koren et al. (2008) found out from satellite products that the spatial resolution strongly affects cloud masks through the contribution of small clouds to the total cloud area.

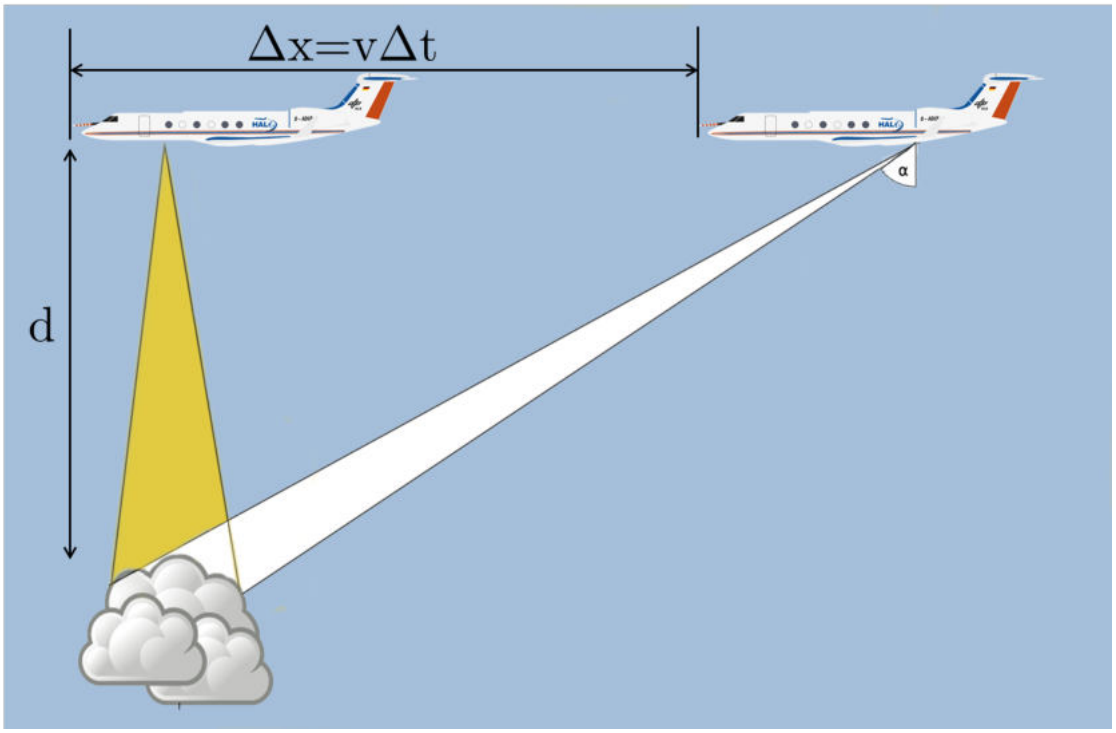

Figure 3.3: Time difference Δt and location difference Δx during cloud detection, due to different viewing directions of the two devices, specMACS (white-shaded) and radar (yellow-shaded). The angle α (not true to scale) denotes the viewing angle of specMACS, looking ahead by 2.6°. The VZA of the radar is zero. Figure redrawn from Pavicic (2018).

This fact motivates the investigation of the effects of the resolution on the specMACS cloud mask, by creating a cloud mask with a coarser resolution. SpecMACS' resolution is adapted to the temporal along-track resolution of the radar cloud mask and FOV characteristics of the radar. First, the specMACS cloud mask is averaged in time and regridded to a temporal resolution of 1 Hz, equivalent to the radar. Secondly, the footprint size of the radar, which is larger than the FOV of every single across-track pixel in specMACS, is considered. While the radar has a footprint size of 0.6°, every specMACS pixel of the SWIR camera has an half-overlapping FOV of 0.22°. The across-track pixels are regridded through averaging windows of six equally-weighted across-track pixels. The number of across-track pixels decreases to 53.

The threshold value to label the averaged pixels as cloudy is simply set to 0.5. If the regridding from the high-resolution pixels leads to an average value below 0.5, the resulting pixel in the coarser resolution is classified as cloud-free, having a value of 0, and vice-versa, if the mean value exceeds 0.5. Actually, both measurement principles from the radar and specMACS, especially their sensitivities, considerably differ though. Figure 3.4 demonstrates the regridded specMACS cloud mask for the scenario depicted in Figure 3.1, compared to the high-resolution cloud mask.

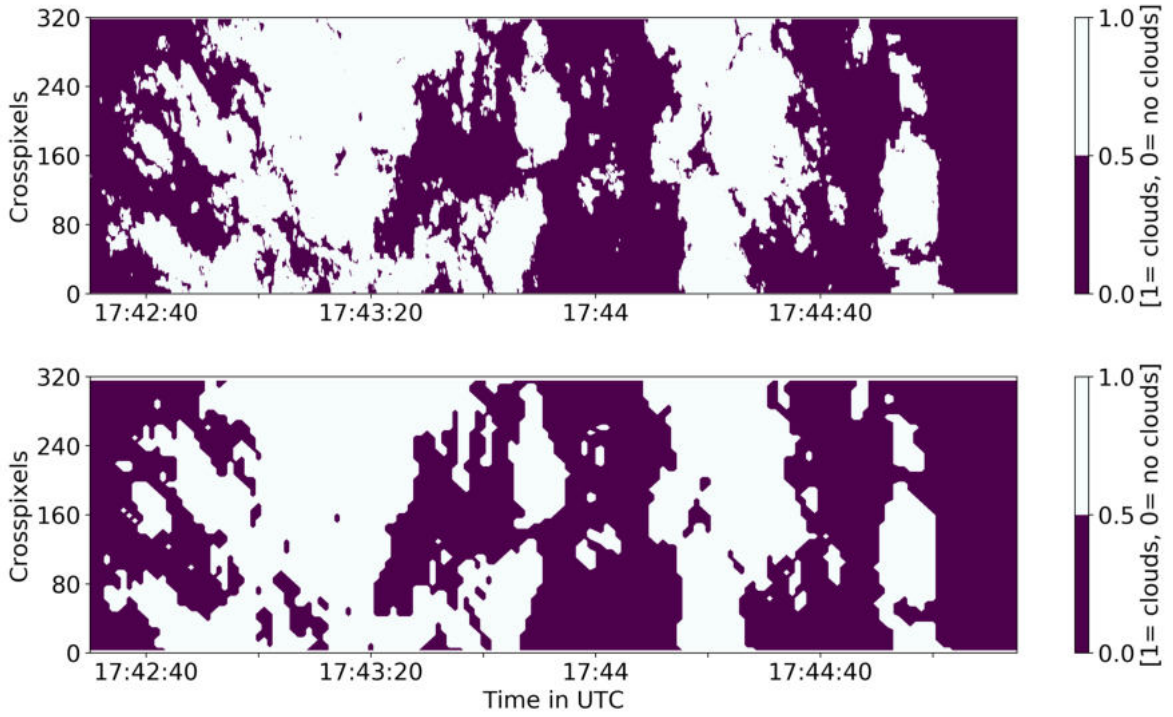

Figure 3.4: Shallow cloud scene from RF06 from 17:42:30 to 17:43:15 UTC seen from specMACS. The upper panel, showing the specMACS cloud mask, is equivalent to Figure 3.1 and the lower panel illustrates the regridded specMACS cloud mask for the cloud scene.

Qualitatively comparing both cloud mask resolutions in Figure 3.4, it can first be concluded that the large cloud structures around 17:43:10 and 17:44:15 UTC persist. In turn, small cloud fragments that are close to the large cloud structures are merged in the coarser resolution. Consequently, the larger clouds are further enlarged by incorporating small holes and the nearby clouds. On the other hand, small clouds that are distant from these clouds (e.g. around 17:44:00) diminish in their size or are even washed out due to the averaging.

As already mentioned in Section 2.2.2, small cloud fragments nearby larger clouds are interpreted as coherent within the radar cloud mask. This is assumed, as the coherence of these clouds could probably not be detected by the sensitivity and the resolution of the radar. By applying a morphological closing, these clouds are merged. Since the cloud labelling is the first essential step for the upcoming statistical cloud analysis, the definition, up to which minimum size and up to which minimum gap length to other clouds, an arrangement of cloudy pixels is considered as one distinct cloud is fundamental. This issue has to be kept in mind for the upcoming analysis and discussion of cloud geometry statistics in the subsequent chapters. Therein, the invariance of cloud statistics to different resolutions shall be examined with the aid of this regridded cloud mask.

3.3 Number of Clouds from Radar and specMACS

An ID-based merging of cloud information from radar (vertical) and specMACS (horizontal) requires an equal number of clouds. As already outlined in Section 3.1 and 3.2, however, this requirement is completely unfulfilled, as specMACS registers far more clouds. During the entire overlapping period in which both devices were reliably in operation (Figure 2.5), specMACS detected 80,000 clouds, whereas the radar only registered 1,000. This section hence identifies the reasons for the loss of more than 98 % of the clouds while using the radar and determines their respective proportions. The lower sensitivity of the radar, causing smaller low clouds in particular to be undetected, serves as one explanation for fewer clouds in radar measurements, for instance during RF03. However, the cloud fraction comparison between radar and specMACS from Pavicic (2018) has not revealed such strong impacts.

Instead, the two major reasons are rather the much higher time-resolution of specMACS and its across-track FOV. Their impact on the number of clouds is separately elucidated in Figure 3.5 by comparing the total number of clouds between the specMACS, the regridded specMACS (according to Section 3.2) and the radar cloud mask and for different viewing perspectives. As shown in the top panel, the regridding of specMACS to a coarser resolution decreases the number of clouds to around 20 % due to the fact that smallest clouds are no longer resolved or seem to be connected to larger adjacent clouds. As a consequence of the across-track FOV, specMACS captures clouds which are not located directly underneath HALO and are thus undetectable for the radar. Looking only at the narrow along-track path within the FOV of the radar in the initial resolution of specMACS, referred to as specMACS 1d, it can be concluded that specMACS is able to see roughly 13 times more clouds due to its across-track FOV. The regridding again induces a decline of 65 %. The consideration of the initial cloud ID in this narrow swath further shrinks the number of clouds from specMACS located within the FOV of the radar, denoted as regr. specMACS 1d with ID. Due to the included across-track information, distinct cloud-pixels emerging into the radar FOV are then no longer identified as new clouds if they are labelled with the equivalent ID. Due to the missing across-track perspective, however, this information is not given for the radar. In particular, specMACS detects more clouds than the radar in the same FOV, even when the IDs are considered and the regridded specMACS is also morphologically closed. SpecMACS data lacks vertical information. This impact on the number of clouds, is estimated using the radar with and without vertical information. The vertical column is checked for containing cloud-pixels. In the case that at least one pixel underneath the aircraft is identified as cloudy, the timestamp is considered as cloudy without any information of the number of clouds, denoted as radar w/o vertical profile. This dimension loss decreases the cloud number by about one third.

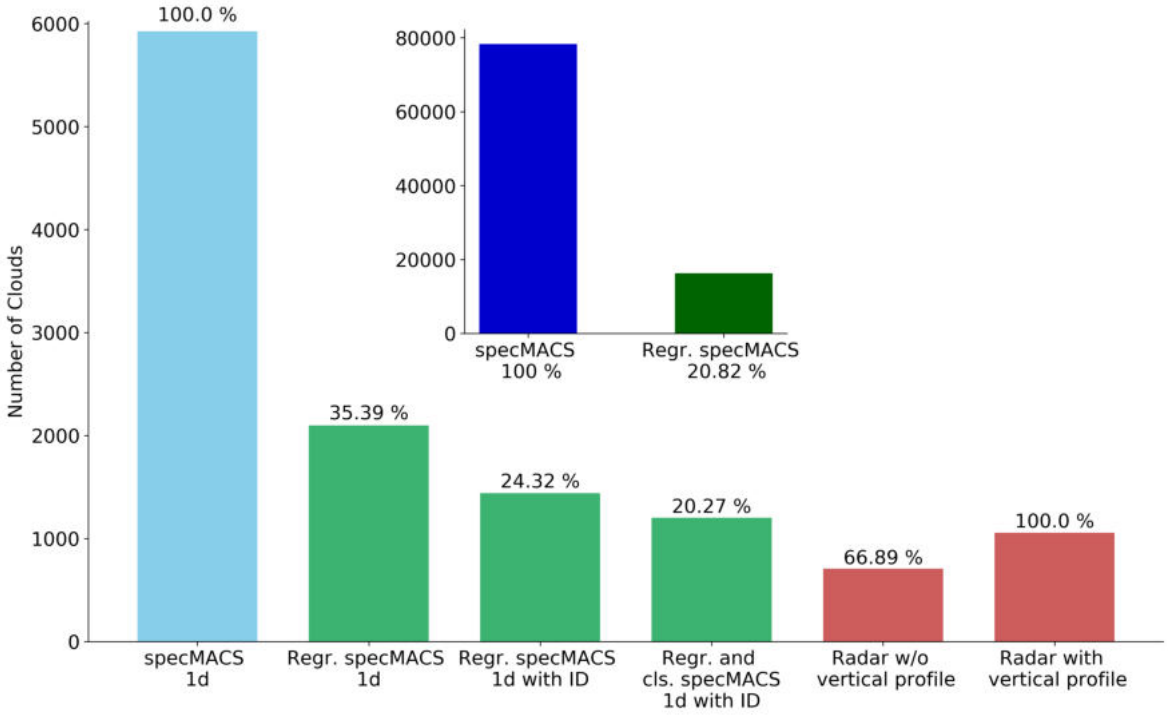

Figure 3.5: Number of clouds from the radar (red) and specMACS (standard resolution in blue, regridded, in green) and from different perspectives, considering the entire across-track FOV (upper panel) and the clouds within the radar FOV (lower panel), denoted as 1d. The two smallest green bars depict the consideration of the cloud ID from the 2D cloud mask, for counting clouds in the radar FOV. The regridded (regr.) cloud mask is also morphologically closed (cls.). The radar cloud number is based on the vertical profile and without it (w/o). Percentages refer to edge bars.

Similarly, a passive instrument cannot separate clouds in the vertical. The comparison of Figure 3.5 constitutes an estimate, as the sensitivity of specMACS and radar is by no means identical. However, it highlights the importance of 3D cloud detection, as each loss in dimension is related to a significant loss of information about each of the clouds and their total number. In particular, the across-track information of specMACS plays an essential role in quantifying the cloud geometries.

3.4 Coordinate Transformation of specMACS Cloud Mask

The coordinate frame of the SWIR camera in specMACS is defined differently for each timestamp. To achieve 2D cloud geometries and to characterise cloud sizes in the horizontal projected plane, the airborne across-track information has to be converted to a distance-based axis. The basic concept is sketched in Figure 3.6 for the transformation from the aircraft-aligned system to the distance-based Cartesian coordinate frame.

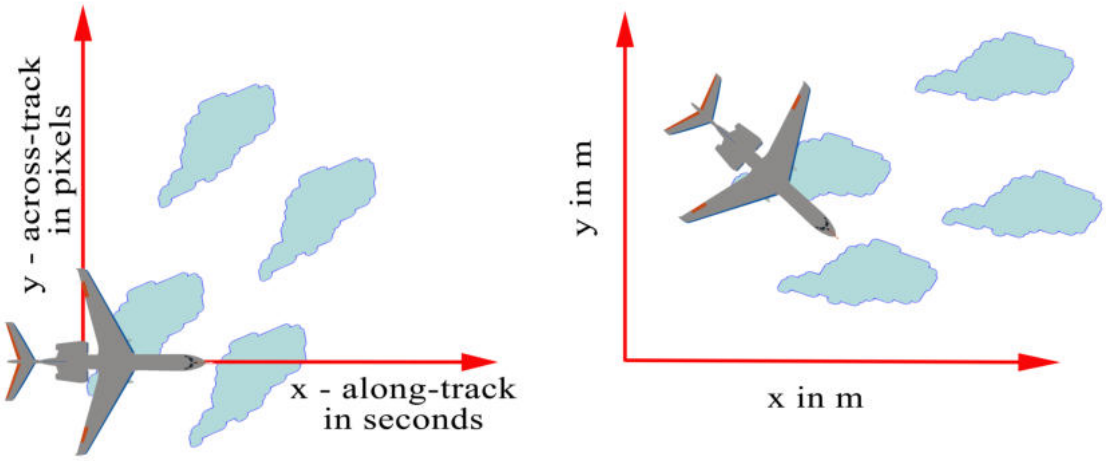

(a) Aircraft-aligned at one timestamp **(b)** Cartesian

Figure 3.6: Illustration of the two coordinate systems in which clouds from the specMACS cloud mask are analysed.

In the following, "Cartesian" always refer to this distance-based coordinate system. The aircraft-aligned perspective has to be transformed in a way that the aircraft is placed into a Cartesian coordinate system, indicating zonal and meridional distances, x and y in meters. Therefore, the Cartesian coordinate system has to be defined static in time for each cloud. This transformation between two coordinate systems requires rotation matrices (Gentle, 2017), that relate the reference system to a new desired coordinate system as described in Equation 3.1 for the linear case:

$$\vec{p} = \boldsymbol{R} \cdot \vec{P} + \vec{r}, \tag{3.1}$$

where $\boldsymbol{R}$ is the rotation matrix between both coordinate systems and $\vec{r}$ represents the translation to the origin in the Cartesian coordinate system. $\vec{P}$ is the direction vector in the initial reference system, given in three-dimensional coordinates, and $\vec{p}$ is the direction vector in the desired (Cartesian) coordinate system.

To define the specMACS cloud mask products within a Cartesian coordinate system, the transformation takes into account the direction vectors of the SWIR camera pixels. In the SWIR coordinate system, each across-track pixel has a defined direction. In reference to the aircraft HALO, this direction is fixed as specMACS has the same viewing direction for each flight. To transform the direction vectors from the SWIR camera pixels into the target Cartesian coordinate system, the product of the rotation matrix $\boldsymbol{R}$ and each pixel direction vector $\vec{P}$ is calculated. Even if $\vec{P}$ is fixed within the camera system, the projection to Cartesian coordinates, however, is dependent on the flight attitude and thus time-dependent. Hence, the rotation matrix $\boldsymbol{R}$ becomes a function of time t. For its computation, aircraft location and

attitude data of HALO from the BAHAMAS dataset, having a time-resolution of 100 Hz, is needed. The BAHAMAS dataset includes the location of HALO via latitude, longitude and cruising altitude, together with the flight attitude, defined by the pitch, yaw and roll angle. These angles are illustrated in the scheme of Figure 3.7. Since the specMACS cloud mask has a time-resolution of 30 Hz, the BAHAMAS dataset is resampled on the identical time resolution, by applying 30 Hz average, and synchronised in time.

The determination of $\boldsymbol{R(t)}$ is provided by the Python library *mounttree* developed by T. Kölling (Meteorological Institute, LMU München). The time-dependent unity direction vectors $\vec{p}_{\mathrm{u}}$ can be calculated from this rotation matrix $\boldsymbol{R(t)}$ according to Equation 3.1. In the target Cartesian coordinate system, the coordinates of every SWIR pixel at one timestamp have the form:

$$\vec{p}_{\mathrm{u}} = \begin{pmatrix} k_x \cdot e_x \\ k_y \cdot e_y \\ k_z \cdot e_z \end{pmatrix}, \tag{3.2}$$

with k_i being a scalar on the axis i, and e_i the unit vector on axis i. For the first timestamp of an appearing cloud, the SWIR camera $\vec{r}_{\mathrm{camera}}$ is set vertically displaced from the origin of the Cartesian coordinate system, having the coordinates:

$$\vec{r}_{\mathrm{camera}} = \begin{pmatrix} 0 \\ 0 \\ h \cdot e_z \end{pmatrix}, \tag{3.3}$$

where h represents the altitude above ground-level of the SWIR camera onboard HALO. For the cloud projection into the Cartesian coordinate system, the height difference between the cruising altitude of HALO and the CTH are required. As described in more detail in Section 3.5, the radar cloud mask allows estimates of the actual CTH for the clouds underneath the aircraft. Based on the CTH from the radar, the height difference, divided by the vertical z-component of the direction vector $\vec{p}_{\mathrm{u}}$, delivers the slanted distance d. This scalar describes to what extent the direction vector has to be stretched for the projection from the aircraft down to the height of the CTH layer z_{CTH}. The location of the cloudy pixel $\vec{c}_{\mathrm{cloudy}}$ in Cartesian coordinates is given by:

$$\vec{c}_{\mathrm{cloudy}}(x, y, z_{\mathrm{CTH}}) = d \cdot \vec{p}_{\mathrm{u}}(x, y, z) + \vec{r}_{\mathrm{camera}}(0, 0, h). \tag{3.4}$$

Applied to every cloudy pixel of one single cloud, the horizontal projection $\vec{c}_{\mathrm{cloudy}}(x, y)$ of all corresponding pixels represents the horizontal geometry of the cloud.

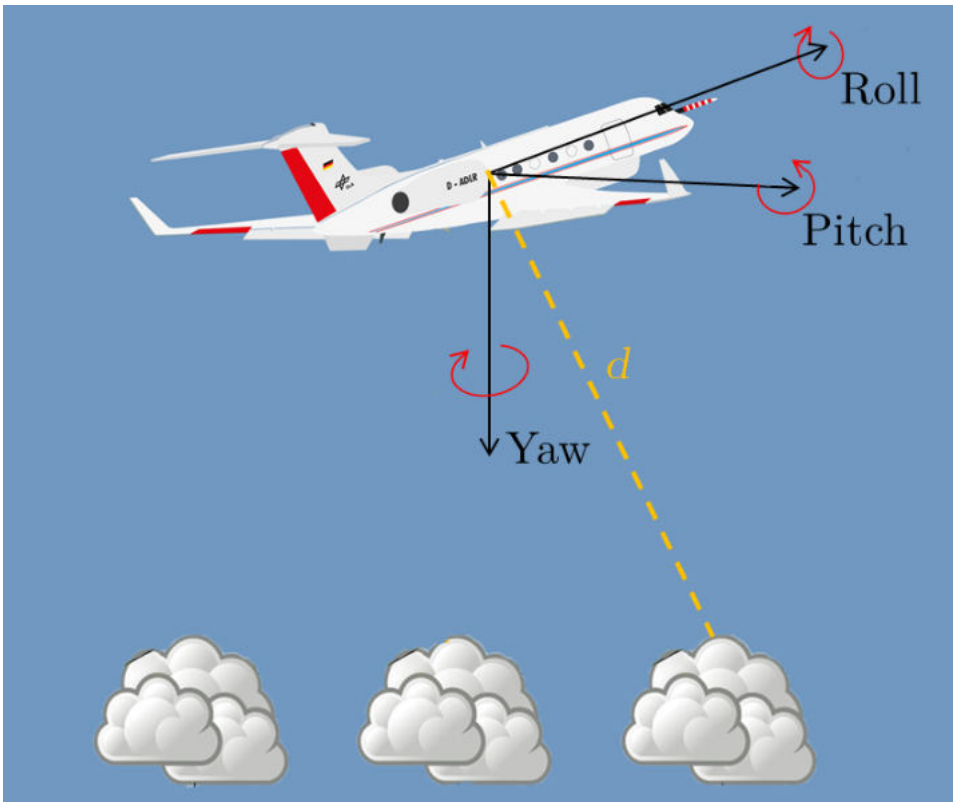

Figure 3.7: Aircraft orientation description via pitch, yaw and roll angle and the slanted distance d between HALO and the CTH, gained from the radar.

This procedure is carried out for the single ID-labelled clouds (Section 3.1). As indicated in Equation 3.3, the position of the SWIR camera at the first timestamp of an occuring cloud is considered as the reference point and is set as $\vec{r}_{\text{camera}} = (0, 0, h)$ for every cloud. The recalculation of the transformation and redefinition of the coordinate system for each cloud individually enable that the x-y plane of the Cartesian coordinate system is better aligned to the surface of the earth at the location of the cloud. Otherwise, a missing redefinition of the coordinate system and of the reference point would cause wrong values of d and thus erroneous cloud projections over long distances, as the Cartesian projection produces a layer in CTH which does not consider the curvature of the surface.

Clouds extending out of the FOV are not included, as their real size outside of the specMACS FOV is not obtainable. In addition, clouds having an along-track cloud length higher than the across-track FOV from specMACS are excluded, as otherwise cloud size statistics would be biased depending on the flight course. In particular, when the sample includes larger clouds, the largest clouds with an orientation along the flight course are considered preferentially.

3.5 Cloud Height Estimates and their Limits

As depicted in Section 3.4, the CTH is of great importance to obtain 2D geometrical cloud characteristics out of the required coordinate transformation, as it specifies the projection path downwards by z_{CTH} and d in Equation 3.4. This section describes the implementation of the radar-based CTH estimates in the coordinate transformation of Section 3.4 with a view to the subsequent analysis of cloud geometries.

To obtain the cloud height, from which a continuous representation of CTH is required, the radar cloud mask is used. Provided by CERA, the unified grid of the cloud mask is given on fixed height-levels. Thus, CTHs below the aircraft can be specified with a vertical resolution of 30 meters. As stated in Section 2.3.2, the cloud mask has the advantage over the reflectivity data that the cloud mask is cleaned of noise. Furthermore, the morphological closing connects very small fragments. Nonetheless, since the radar is also sensitive to rain droplets, wind-affected fall streaks that reach into the FOV of the radar can cause very low CTH values that actually only refer to precipitation. The sensitivity of the radar can cause too low CTH values, in particular when the detected clouds are rather low and small in their extent. In other cases, the surface of the ocean is not correctly filtered out from the cloud mask.

The time-series is hence quality-checked for physical limits in order to guarantee plausible CTH values. Defined as the height at which an adiabatic lifted air-parcel reaches saturation and above which the air parcel will begin condensing, the LCL represents a good approximation of the CBH and hence serves as a lower threshold for CTH. The LCL is calculated from the dropsonde profiles of pressure, air temperature and dewpoint. For this, the Python package *metPy* (May et al., 2020) is included to obtain the LCL in a pressure height. The height of the nearest pressure value within the unified grid is then considered as the height of the LCL in meters. The discrete LCL values from the dropsonde releases are then interpolated in time to the same resolution of the radar cloud mask so that a lower CTH threshold for every time step exists. CTH values below the lifting LCL are filtered out.

However, as found in Section 3.3, the radar captures fewer clouds than specMACS, even in the same FOV. This loss has two reasons: The different resolutions and the different sensitivities of both devices. The discrete along-track CTH values are thus upsampled through interpolation in time and time-synchronised to the specMACS resolution. As a result, the continuous along-track time-series of CTH is obtained.

The across-track observation of clouds with specMACS enables a much larger sample of clouds lying laterally of HALO to be included in the cloud analysis. For this purpose, the coordinate transformation also requires estimates of CTH in the across-track direction. Since none of the active devices (Section 2.1.2) can provide across-track cloud height measurements (Figure 3.2), the CTH is set constant in the across-track direction as a simplified assumption. It is evident that this simplification severely increases uncertainties in CTH estimates.

To circumvent this issue, the resulting uncertainties can be dammed to a certain magnitude when only shallow low-level cloud scenes are taken into account and flights or at least flight periods in deep convection regimes are ignored. In particular, the CTH variability is significantly lower in shallow convection regimes. The restriction to low-level cloud regimes also has advantages regarding sources of errors resulting from the viewing geometry of specMACS. The further the detected clouds are located at the edges of the FOV, the higher the pixel VZA and the more clouds are detected from the side. This error additionally increases more the deeper the clouds in deep convection are and the higher the general cloud height in high-level cloud regimes is (Henderson-Sellers and McGuffie, 1990). Since the CTH uncertainties have a non-negligible impact on the cloud geometry results, Section 3.6 establishes a method to quantify their magnitude.

3.6 Determination of Cloud Height Uncertainty

Several assumptions and simplifications are made within the cloud geometry analysis. These are strongly pronounced within the coordinate transformation, whereby the cloud projection depends on the assumed cloud height (Section 3.5). The simplification of an across-track constant cloud height and its interpolation in time cause uncertainties. Since every single cloud undergoes a coordinate transformation, the absolute CTH uncertainty U_{CTH} has a different magnitude for each cloud. This has to be considered in discussing the upcoming results from the cloud geometry analysis.

The determination of U_{CTH} is explained with the aid of Figure 3.8, depicting an exemplaric shallow cloud scene during RF06 from 16:43 to 16:46 UTC. The method makes use of the radar data in combination with the regridded specMACS cloud mask, having a 1 Hz time-resolution and simulating the radar footprint size (see Section 3.2). Figure 3.8 reveals that each cloud has one average uncertainty value U_{CTH}.

According to the unified grid (Section 2.2.2), the radar cloud mask resolves the CTH with an accuracy of 30 m. Under the simplified neglect of biased measurements due to the radar sensitivity, the CTH has thus an initial uncertainty of at least 30 m. However, this consideration only applies for specMACS cloud-pixels within the radar-detected clouds in the narrow overlapping FOV in which the radar theoretically detects the same clouds as the regridded specMACS. In that case (e.g. at 16:44:45), the specMACS pixels in the overlapping FOV are assumed to have a small CTH uncertainty of 30 m. In Figure 3.8, this assumption is only valid along the orange line. Pixels outside of the radar cone are supposed to have a significant higher CTH uncertainty. Cloud top heights farther in the across-track field are less certain than underneath the aircraft. For most of the flight periods, the entire across-track FOV of specMACS extends to about 8 km. This additional uncertainty is included based on an estimate of the across-track CTH variability, as follows:

Around radar-detected clouds, the across-track CTH variability is calculated as the average of a running standard deviation of the CTH, including windows of 20 radar pixels. The consideration of 20 pixels represents about 4 km for a typical ground speed of 200 m/s and quantifies the across-track CTH variability in the vicinity of radar-detected clouds in both across directions. Its value is added at the edges of the specMACS FOV and linearly interpolated to the centre pixel having a value of zero. Thereof, the across-track based values are added in both lateral directions to the previously calculated uncertainties in the along-track. This means that the smaller the across-track extension of clouds being partly detected by the radar is, the lower their absolute uncertainties are (Figure 3.8), as their internal across-track variability is decreased compared to clouds that extend up to the edges of the FOV. Nonetheless, it has to be mentioned that the across-track distance changes during flight with regard to the flight attitude. Therefore, the fixed running window size only represents a simplification. During most of the flight periods, the aircraft cruising level was rather constant though and curves were flown quite large-scale. The estimate of CTH variability from fixed across-track distances is thus a sufficient assumption.

Several clouds are completely unresolved using the radar (e.g. shortly before 16:46) and are even not within the vicinity (4 km) of detected clouds. In these cases, U_{CTH} is approximated from the overall variability of CTH from the radar. This is quantified by the standard deviation of the radar-based CTH time series. In order to neglect any daily cycle of CBH and CTH (Vial et al., 2019), the standard deviation only considers flight periods of 30 minutes and uses its mean in the uncertainty analysis. For the given scene in Figure 3.8, these clouds have CTH uncertainties of around 280 m.

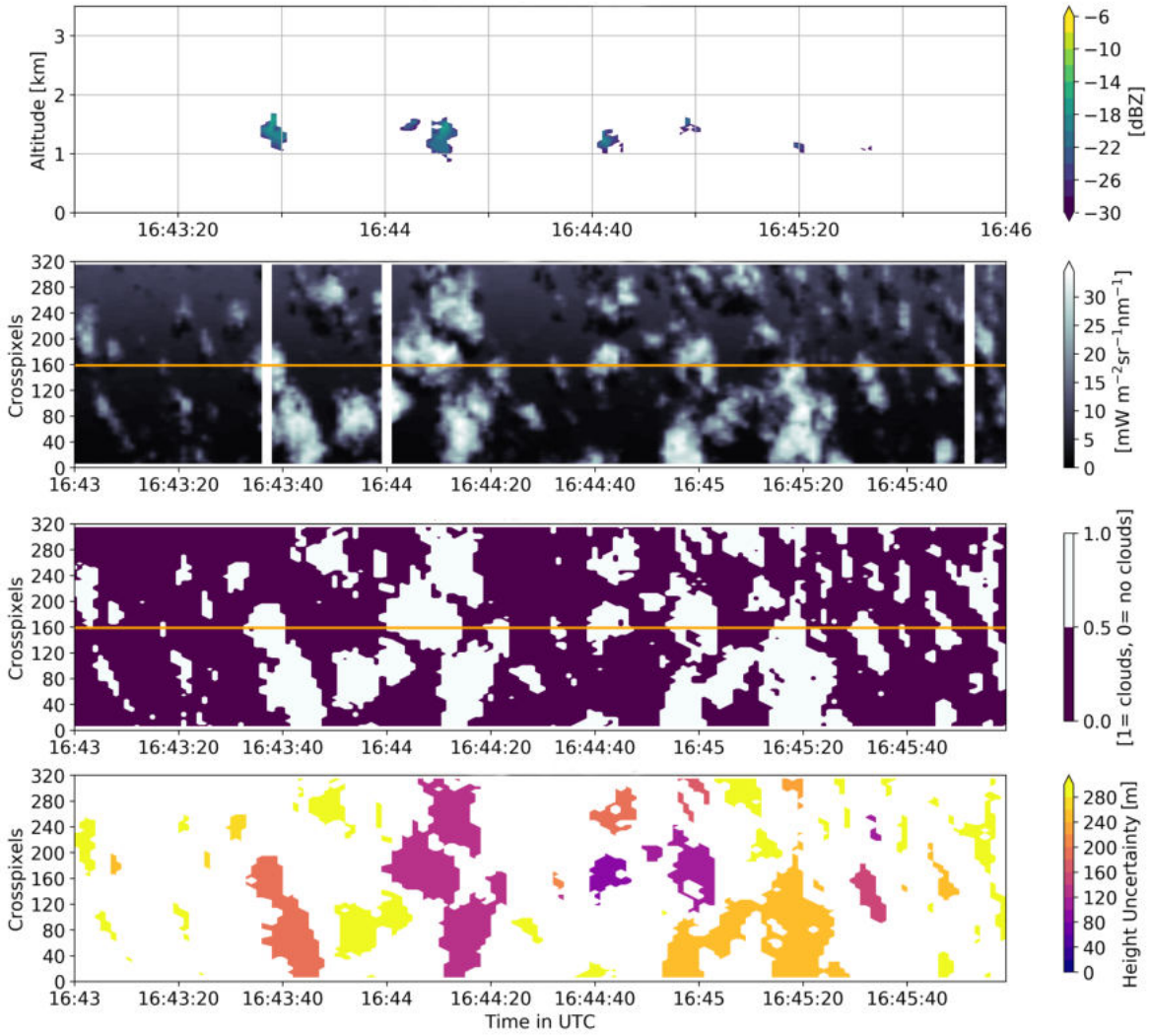

Figure 3.8: Airborne measurements of an exemplary shallow cumulus scene from RF06. The time period is indicated on the x-axis at the bottom. The upper panel shows the radar reflectivity in dBZ. The second and third panel illustrate the specMACS measurements and the cloud mask respectively which are downgridded to the equivalent time resolution of the radar (regridded specMACS). The last panel quantifies the average CTH uncertainty for each cloud given in the scene.

The pixel-specific uncertainty values are averaged for each labelled cloud (Section 3.1). The approach to reduce the uncertainties to a mean value per cloud results from the effects implementing the uncertainties in the coordinate transformation. Otherwise, with linear increasing uncertainties in the across-track direction, clouds are always increasingly compressed or stretched in the across-track direction and thus irregularly deformed. Thus, each cloud is associated with one absolute mean value of U_{CTH}. Finally, the cloud analysis can be performed with the initial CTH $\pm$ the obtained uncertainties of cloud height U_{CTH}. In the cases where the subtraction leads to CTHs below the LCL, the CTH is set back to LCL in order to remain physically consistent.

3.7 Elliptical Fitting of Clouds

After applying the coordinate transformation to each cloud (Section 3.4), cloud shapes are described in Cartesian coordinates on meridional and zonal scales. In this system, cloud shapes reveal a certain variability. Simplifications in their shape description are hence beneficial in order to compare the geometries of single clouds. Cloud sizes are frequently quantified by the cloud area-equivalent diameter D, by which clouds are compared in a circular perspective. D defines the diameter of a circle which spans an equally sized area A as the cloud, as follows:

$$A = \frac{\pi}{4} \cdot D^2. \tag{3.5}$$

In the scope of this thesis, however, a step further is taken and cloud shapes are also enlightened with regard to their dominant spatial extension and orientation. While circular description of clouds is useless for this aim, as clouds would then be homogeneous in all directions, another principal shape description is required. It has to provide a reference to which the rotation of clouds is clearly attributable and by with the cloud shapes are characterised in a standardised way as trivial and as precise as possible. These requirements are met by an elliptical description of cloud shapes which allows to determine the orientation of clouds and the deviation of cloud shape from the idealised description as a circle. Each cloud labelled in Section 3.1 within the specMACS cloud mask that does not extend out of the FOV is fitted by an ellipse. The fit has to be performed within the Cartesian coordinate system, as otherwise the geometrical cloud shape is not correctly interpreted from the arrangement of cloud-pixels in the aircraft-aligned coordinate system. This is schematically depicted for a cloud scene captured from specMACS in Figure 3.9. The fitting algorithm is performed in a least-squares sense based on the methods of Fitzgibbon and Fisher (1996). Mathematically, ellipses are bivariate equations with a set of points in the form of $\vec{p} = (x, y)$ that fulfil the equation:

$$f(\vec{d}, \vec{p}) = \vec{E} \cdot \vec{d} = 0, \tag{3.6}$$

in which the vectors are $\vec{E} = (x^2, xy, y^2, x, y, 1)$ and $\vec{d} = (d_{x,x}, d_{x,y}, d_{y,y}, d_x, d_y, d_1)$. $f(\vec{d}, \vec{p_i})$ represents the so-called algebraic distance of a point $\vec{p_i} = (x_i, y_i)$ to the conic. Since the least-square approach aims to minimise the algebraic distance, the mathematical term transformation then leads to an eigen value problem, having the form:

$$1/\lambda \cdot \vec{d} = S^{-1} M \vec{d}, \tag{3.7}$$

where $S = \vec{E}\vec{E}^T$ and M is a 6x6 matrix. The centre of the ellipse, its rotation angle and axes can be inferred by solving this equation and determining the eigen vector $\vec{d}$.

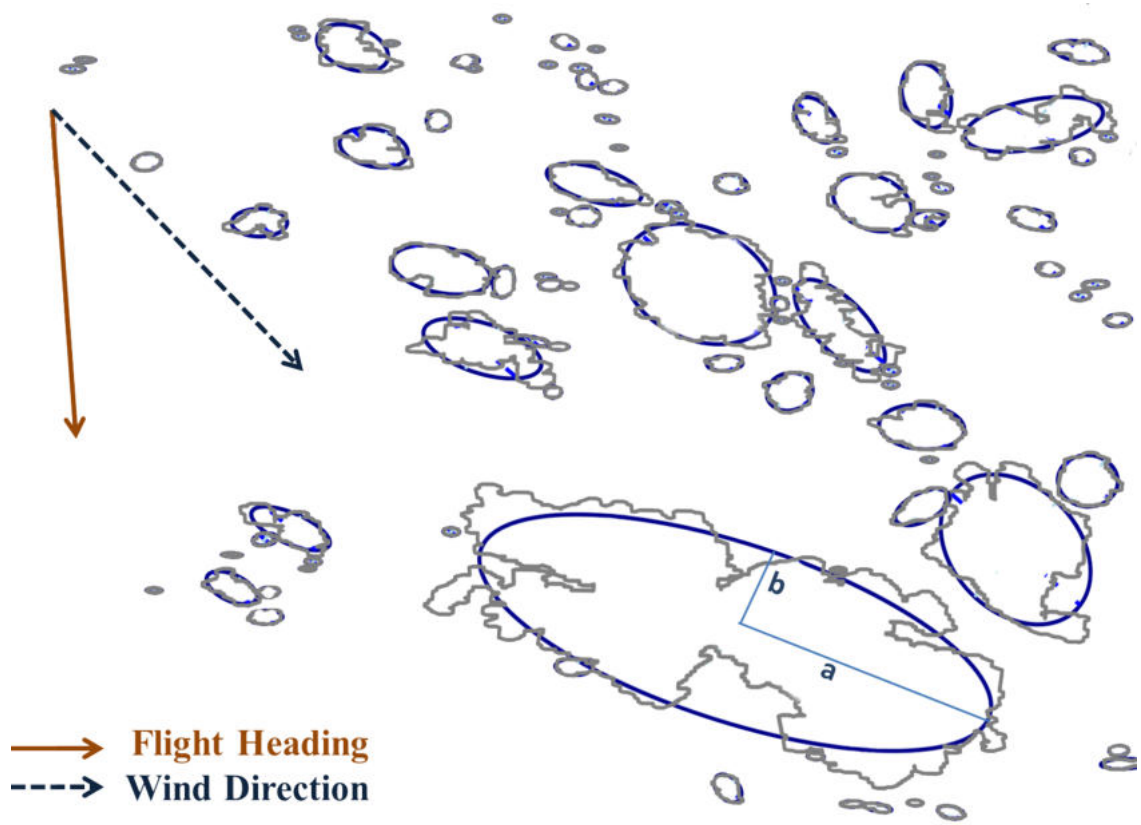

Figure 3.9: Schematic illustration of the elliptical fit around clouds from the cloud mask, drawn as grey contours. The fitting ellipses are plotted in blue. The major axis a and minor axis b are indicated for the largest cloud. The flight heading and the mean wind direction in cloud top height are indicated as arrows in the top left corner.

Ellipses are defined by their semi-major axis a and their perpendicular semi-minor axis b, as illustrated for the largest cloud in Figure 3.9. In order to compare the elongation of ellipses and the deviation to a circle, the cloud analysis makes use of the definition of the eccentricity e:

$$e = \sqrt{1 - \left(\frac{b^2}{a^2}\right)}. \tag{3.8}$$

If clouds have circular shapes, e will have a value of 0. The stronger the stretching of clouds is, the further their value of e approaches 1.

Referring back to the established cloud analysis workflow, the contours of clouds within the Cartesian coordinate system are determined and described as polygons, using the Python library *skimage*. According to Equation 3.6, these polygons can be considered as a set of points $p = p(x, y)$ to which the fitting algorithm is applied and whereout the ellipses can be drawn. Each elliptical fitted cloud can be thus characterised by the geometries of its ellipse.

For the given scene in Figure 3.9, clouds are true to scale, showing several magnitudes of cloud sizes, whereby the largest cloud has a major axis of around 3 km. The elliptical fit represents a valid simplification of the cloud shape for the depicted clouds. Since the least square fit aims to find an ellipse that has a similar area to the cloud polygon, the ellipses sometimes tend to look quite small for complex clouds. The elliptical fit reveals the orientation of clouds well, showing tendencies into the wind direction.

Chapter 3 described the methods applied to the cloud mask dataset of specMACS, making additional use of the radar cloud mask, dropsondes data and the aircraft BAHAMAS dataset. The methods aim to provide the framework for the cloud geometry analysis from NARVAL-II. The merging of the cloud information primarily involves the following aspects:

- Single clouds are identified and labelled from the specMACS cloud mask through a connected-component analysis based on eight-connectivity.
- The viewing directions and resolutions of specMACS and the radar have to be considered in order to apply a synchronisation in time of detected clouds within the overlapping FOV.
- Every cloud from specMACS is transferred into a Cartesian coordinate system in order to obtain geometrical cloud information in the across-track dimension. This requires information of the flight attitude from the BAHAMAS dataset.
- The coordinate transformation requires a physical plausible CTH estimate (being above LCL) and therefore makes use of the radar cloud mask. The continuous LCL time-series is gained from dropsonde profiles through interpolation in time.
- CTH uncertainties are assessed with a major focus on the weakness of the assumption of across-track constant cloud height.
- Clouds are fitted as ellipses in order to facilitate the comparison of cloud shapes and their orientation for different BL conditions.

4. Single Cloud Characteristics

Based on the methods presented in Chapter 3, this chapter investigates the single cloud characteristics regarding cloud geometries. The fact that the radar detects less clouds than specMACS even in the overlapped FOV (Section 3.3) motivates a further investigation of the influence of the larger sample of clouds from specMACS on cloud size statistics. Besides the along-track cloud size, the benefit of the 2D-cloud mask from specMACS on the cloud statistics is highlighted and compared to the radar. Other questions focussing on shallow cloud geometries examined in this chapter are:

- How sensitive are the cloud size distributions to different observational and mathematical approaches?
- What is the 2D cloud size in terms of cloud area?
- To what extent do clouds that are to small to be resolved by the radar contribute to the total cloud area?
- How representative is the elliptical shape for clouds?
- What is the actual shape complexity of shallow trade wind clouds?

4.1 Cloud Size Distribution

Ranging over several orders of magnitude, starting from a few meters up to several ten kilometres, the vast majority of tropical shallow low-level clouds are rather small and the cloud size distribution tails off towards rare larger clouds (Zhao and Girolamo, 2007). Thus, cloud size distributions are conventionally analysed in logarithmic mode. As verified from observations by Zhao and Girolamo (2007), tropical cloud size distribution obeys a power law distribution. The frequency $n(D)$ of the cloud size D mostly representing the area-equivalent diameter (Equation 3.5), is described as:

$$n(D) = a \cdot D^{\beta}, \tag{4.1}$$

with a and β being mathematical coefficients.

Taking the logarithm of Equation 4.1, the cloud size distribution can be fitted by a linear function with the slope β:

$$\log(n(D)) = \log(a) + \beta \cdot D. \tag{4.2}$$

Apart from Zhao and Girolamo (2007), tropical cloud size distributions have been widely studied using airborne and satellite observations and are very relevant for cloud-modelling parametrisations. This section investigates the along-track size distributions of the clouds recorded during the NARVAL-II campaign and thereby extends the analysis of Gödde (2018), who first calculated such distributions from specMACS for the two flights RF03 and RF06. For that, the methods to quantify the along-track cloud size from airborne measurements are described in a first step. The influences of larger cloud samples provided by specMACS, on cloud size statistics are examined by comparing the along-track cloud size distribution from specMACS to that from the radar in their overlapping FOV. Using this knowledge, the along-track cloud length for all clouds of the considered flights (Section 2.5) are discussed.

4.1.1 Airborne Determination of Along-Track Cloud Size

Along-track cloud size distributions are frequently calculated from airborne and satellite measurements, e.g. in Wood and Field (2011). From the airborne cloud datasets from NARVAL-II, this one-dimensional (1D) investigation also represents the most simple approach to quantify the cloud sizes due to the cloud detection in the along-track direction. Both cloud mask datasets, from the radar and specMACS respectively, provide the timestamp for every cloudy pixel. Hence, the along-track cloud length can be calculated under consideration of the aircraft ground speed. Using the given time period Δt between the first and last cloudy pixel that correspond to one cloud and considering the mean ground speed $\overline{v}$ from the BAHAMAS dataset, the along-track cloud distance is calculated as:

$$\Delta x = \overline{v} \cdot \Delta t. \tag{4.3}$$

Regarding the radar and its time resolution of 1 Hz, only clouds longer than 200 m can be measured for a typical ground speed of 200 m/s. According to the tropical marine cloud statistics from Zhao and Girolamo (2007), however, 90 % of the clouds observed have a cloud area-equivalent diameter below 200 m. Having a time-resolution of 30 Hz, specMACS is able to detect these smaller clouds. However, the high sampling rate of specMACS leads to distances between two consecutive camera frames which are lower than the along-track FOV of each pixel, as demonstrated in Figure 4.1.

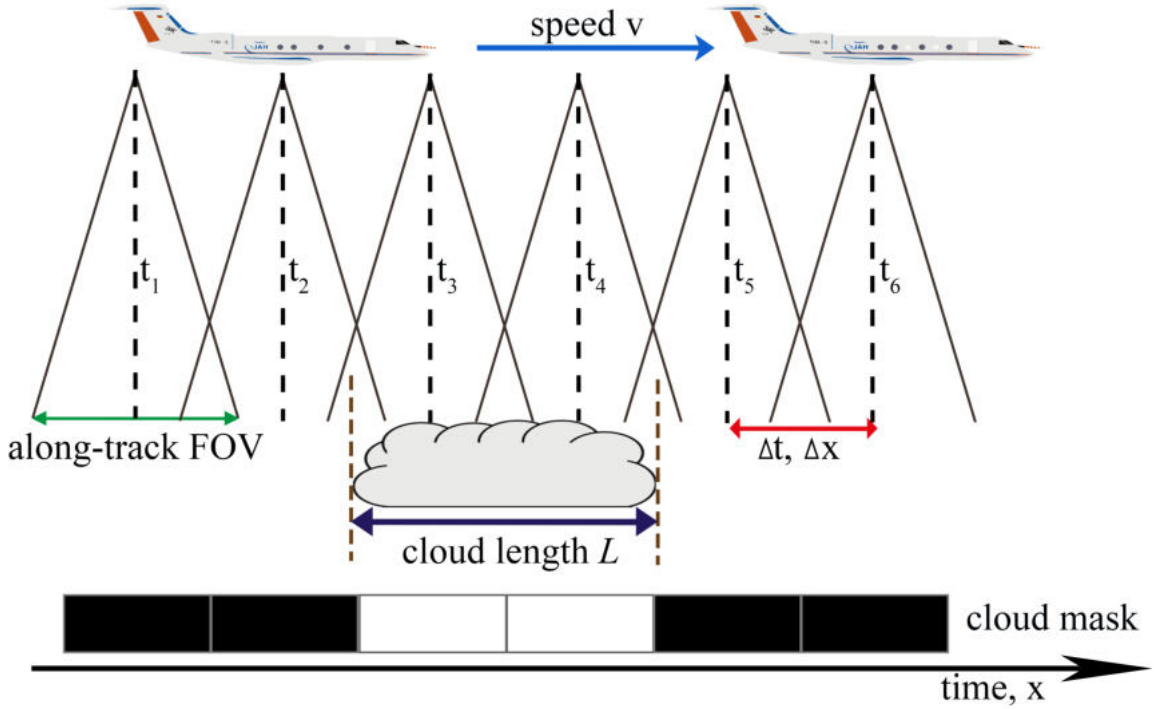

Figure 4.1: Sketch of a cloud overpass from HALO together with the corresponding measurement time steps from specMACS. For each measurement timestep, labeled as t_i, the gray cones indicate specMACS' FOV. Δt and Δx here denotes the distances between two consecutive pixels. The panel show the cloud mask with two pixels labelled as cloudy. The abscissa axis represents the time and specifies the location of the aircraft. Figure redrawn from Gödde (2018).

To avoid this issue, Gödde (2018) provided a method to calculate along-track cloud sizes, even though the FOVs overlap. His approach is also explained with the aid of the cloud overpass in Figure 4.1. As sketched, the cloud extends over two frames and is also partly detected by the neighbouring pixels, as their along-track FOVs overlap. Therefore, it is assumed that each cloud extends to about half of the distance of the previous and following cloud-free pixel (t_2 and t_5 in Figure 4.1). The along-track cloud length L is hence calculated by the modification of Equation 4.3:

$$L = \overline{v}\left(\frac{t_\mathrm{in} - t_\mathrm{in\text{-}1}}{2} + t_\mathrm{end} - t_\mathrm{in} + \frac{t_\mathrm{end+1} - t_\mathrm{end}}{2}\right), \tag{4.4}$$

where t_in and t_end denote the timestamps of the first and last cloudy pixels of a specific cloud (t_3 and t_4 in Figure 4.1). Considering both Equations 4.3 and 4.4, along-track size distributions of the clouds recorded by both devices can now be investigated.

4.1.2 On the Trust in Cloud Size Distributions

The impact of the measurement perspectives for both devices on the along-track cloud size is investigated in the following. For all considered flights during NARVAL-II, Figure 4.2 depicts the corresponding along-track cloud size distributions intercomparing radar and specMACS within their unanimous FOV (Figure 3.2). Hence, only a very small strip from the specMACS across-track FOV is taken into account and interpreted as 1D swath. In case of specMACS, two cloud mask resolutions are investigated. The analysis also considers the regridded cloud mask for the sake of representative comparability between both devices, radar and specMACS. As introduced in Section 3.2, the regridded specMACS cloud mask aims to adapt the spatio-temporal resolution of specMACS to that of the radar having a time-resolution of 1 Hz and considers the larger footprint.

The considered along-track cloud lengths plotted in Figure 4.2 are restricted to a range from 300 m up to 10 km, but with open intervals at both ends. All three cloud size distributions show noise behaviour for cloud sizes above 6 km, as the sampling rate is very low. For clouds shorter than 6 km, the distributions show a robust decrease in the relative number of clouds with increasing cloud size. According to the slopes of the step functions approximating the cloud size distributions, the frequency decay towards larger clouds is less sensitive to the resolution of the cloud mask than to the device.

Concerning specMACS, the slope of the normalised distribution is quite similar in both resolutions for most of the cloud sizes. However, the higher the time-resolution, the smaller the clouds that can still be captured. This leads to a shift towards lower values in case of the high-resolution cloud mask. A higher proportion of cloud lengths below 300 m shifts the distribution leftwards. The similar decay indicates that the wash out of subgridded clouds, mentioned in Koren et al. (2008), has a minor influence on the slope of cloud size distributions.

The radar detects larger clouds in the along-track direction more frequently, manifesting in a weaker decay of the distribution. This results from the morphological closing that partly merges distinct clouds into single clouds, so that in particular the relative number of small cloud fragments decreases. Another reason for distribution variations is the ability of the radar to vertically distinguish between clouds, whereas the specMACS cloud mask cannot distinguish between cloudy pixels from different heights and projects overlapping clouds onto a single cloud. This contrarily affects cloud size distributions, as specMACS overestimates the size of these clouds.

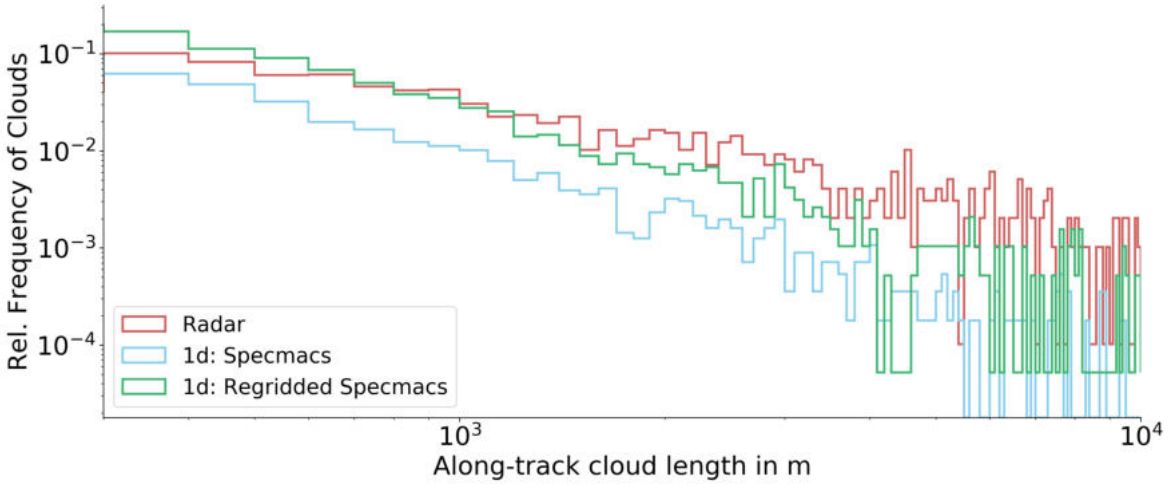

Figure 4.2: Along-track cloud size distribution on logarithmic scale captured by specMACS (blue and green) and the radar (red) only considering their overlapping FOV and being one-dimensional (1d). The 1d regridded specMACS represents the coarser cloud mask having a time-resolution of 1 Hz (Section 3.2). Cloud sizes are subdivided in 200 m bins and the relative number of clouds within the bin widths is plotted as step function.

One of these typical cloud scenes is paradigmatically illustrated in Figure 4.3 from a 30-minute radar measurement period. According to the radar reflectivity, several clouds overlap each other and in high levels, the pattern of anvil clouds shields underlying clouds. In the specMACS cloud mask (not shown), most of these clouds are merged into one single cloud due to missing vertical information. In particular while approaching and partly crossing the ITCZ (during RF02 and RF07), a bunch of these anvil cloud scenes is found.

Depending on the prevailing cloud scenario, it is therefore crucial to declare one of the demonstrated cloud size distributions as the truth in the narrow swath. In deep convective regimes, where clouds occur in several levels as well as during flight periods where thin cirrus layers shield underlying clouds, radar-based along-track cloud sizes are postulated as more representative. In shallow convection regimes, where the majority of cloud sizes is smaller than the radar resolution (Zhao and Girolamo, 2007), cloud size distributions obtained from specMACS are generally more representative due to the higher temporal resolution.

Furthermore, as indicated in Section 3.3, the fact that the radar did not detect a certain amount of shallow low-level clouds underneath the aircraft during several flight periods (e.g. in RF03), as the backscatter signal of the low and small clouds is too weak, leads to an undersampling of small cumulus clouds.

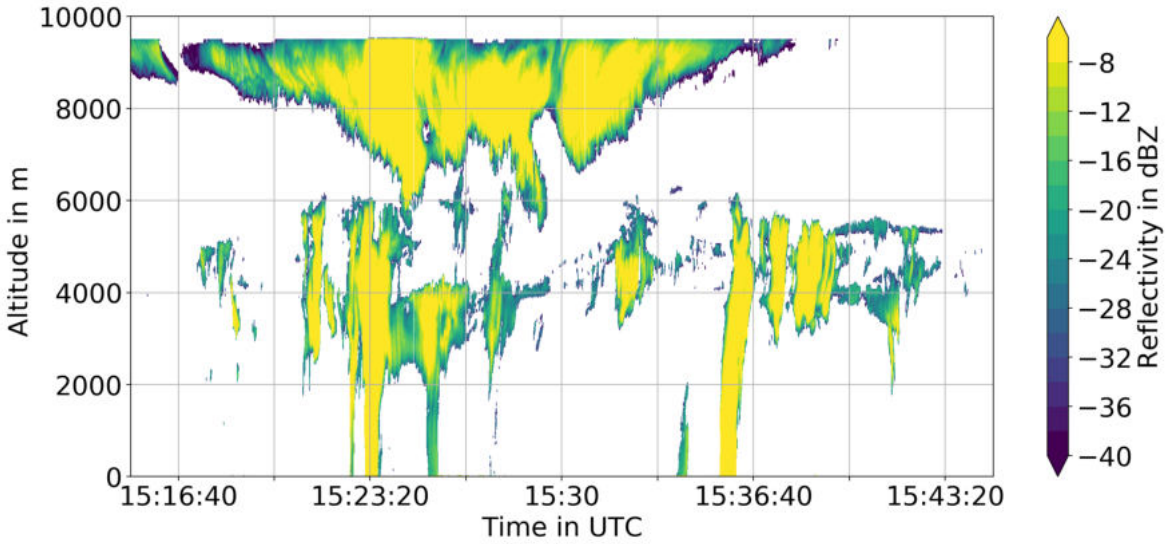

Figure 4.3: Radar equivalent reflectivity measurements in dbZ of a cloud scene from 15:15 to 15:45 UTC during RF07, showing the vertical cloud composition in the along-track profile.

Regarding the clouds extending into the radar FOV, the length of which is only measured in the narrow strip up to here, the across-track perspective of specMACS enables the determination of their maximum cloud length as depicted in Figure 4.4. If clouds are only captured at their outer edge from the radar, their determined length can deviate significantly from the actual extension. Thus, as indicated by the blue-dashed lines in Figure 4.4, the consideration of the cloud shape in two-dimensions and in the entire along-track is an improved representation of the along-track cloud size.

Apart from the across-track benefit to determine the maximum along-track length for clouds extending into the unanimous FOV, one further strength of specMACS arises out of its across-track view. As described in Section 3.3, the detection of clouds that are completely outside the radar FOV causes a significant increase in the cloud sampling. Its effect on the cloud size statistics for the standard and coarser regridded specMACS cloud mask respectively is demonstrated in Figure 4.5. The light-coloured histograms (plotted as step functions) again approximate the cloud size distribution based on the 1D consideration in the FOV of the radar. The dark spectra here consider all clouds detected within the overall specMACS across-track FOV. A linear least-square fit is applied to the distribution to obtain the slope parameter β of the power law, as stated in Equation 4.2. Accordingly, the magnitude of the decay in the relative distribution is more sensitive to the along-track length determination method than to the resolution of the cloud mask, which can be identified from the slopes of radar and specMACS.

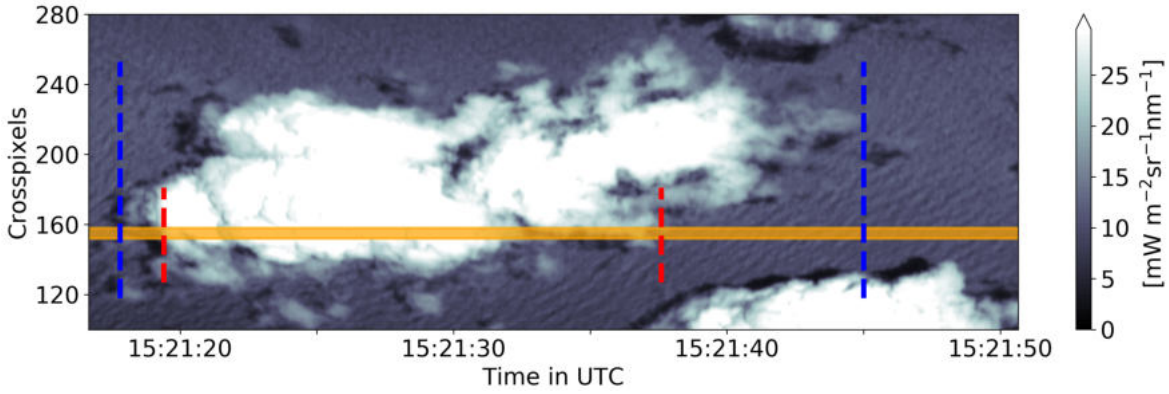

Figure 4.4: One cloud partly extending into the FOV of the radar (orange line) measured by specMACS (1600 nm radiance given in the colour bar) from RF03. Dashed lines indicate the along-track cloud length within the radar FOV (red) and the whole along-track cloud length for the entire across-track extension (blue).

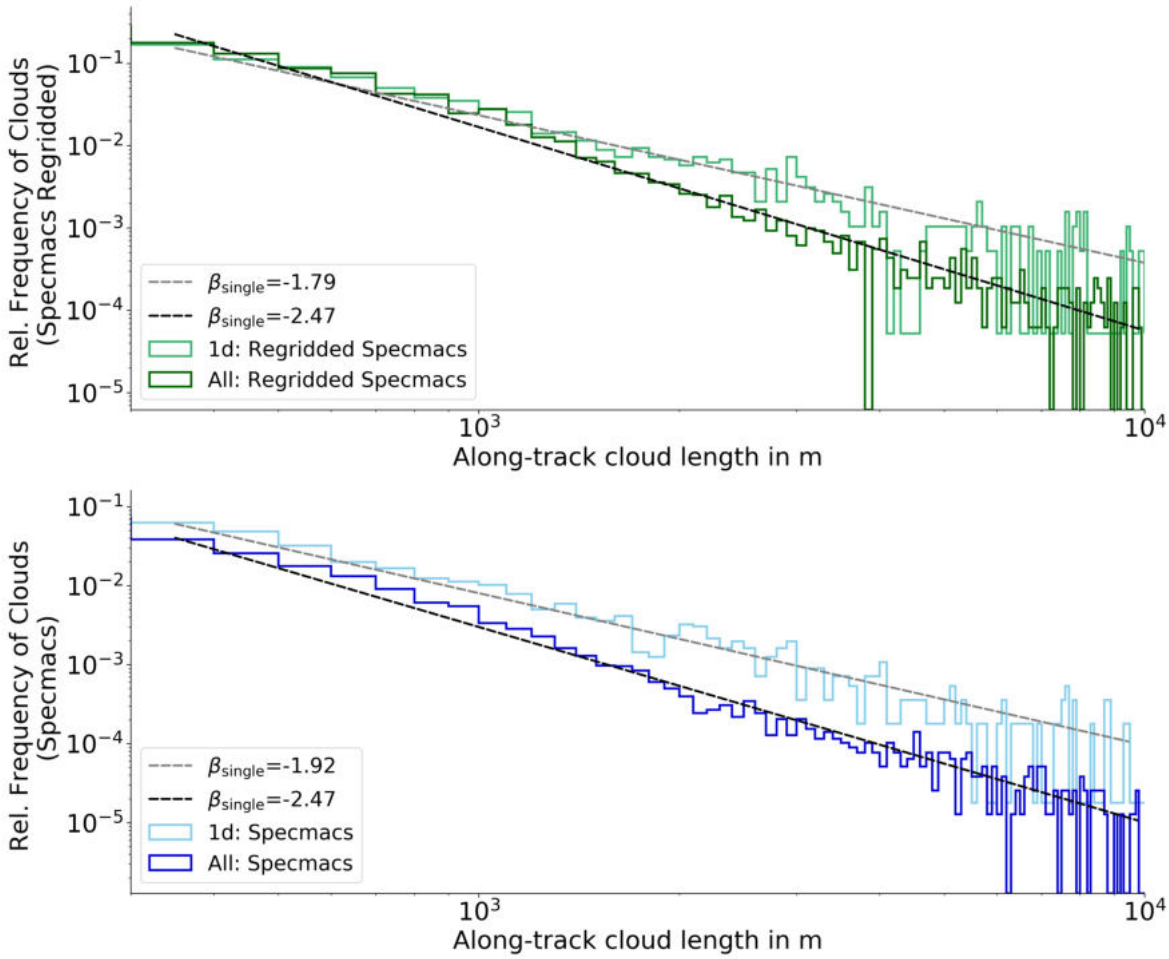

Figure 4.5: SpecMACS along-track cloud size distribution for clouds within the radar FOV (light colours) and the overall along-track cloud length for all clouds within the entire FOV from specMACS under consideration of the across-track view (dark colours). Statistics of both cloud mask resolutions are shown. β_{single} denotes the slope from the linear fit for each distribution.

Intercomparing both specMACS resolutions, the distributions of the regridded cloud mask are again shifted rightward compared to the standard specMACS cloud mask for the same reason explained for Figure 4.2. Within one viewing perspective, the slope parameter β has similar values. It is notable that β has a value of -2.47 for both cloud mask resolutions if all clouds from the entire FOV are considered. Under consideration of all clouds in the across-track and their whole along-track length, the relevance of the cloud mask resolution on β hence becomes negligible.

The decay of the distribution is much stronger if the entire across-track field is considered. Even if for single clouds, the respective along-track lengths can vary strongly due to the narrow swath, they should cancel each other out under random sampling with respect to the overall statistics. The substantial decrease of the larger cloud contribution in the cloud statistics can instead be explained by the fact that larger clouds in the along-track direction generally tend to be larger in the across-track direction. Hence, they often extend to the edges of the across-track field and cover the whole FOV, as it can be seen in Figure 4.6 for the two large clouds in the scene. Since the FOV from the radar only represents a narrow strip, just a minor portion of the small clouds are captured, whereas the largest clouds are captured in every case.

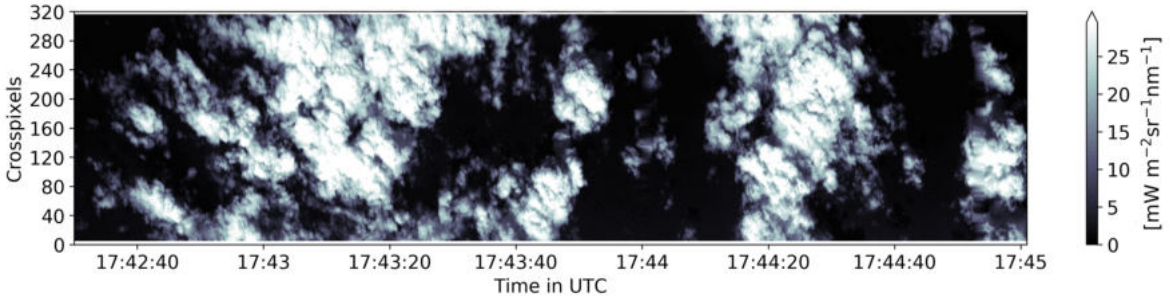

Figure 4.6: Cloud scene captured by the SWIR camera from 17:42:30 to 17:45:00 during RF06. The measured radiance of the 1600 nm channel is shown.

4.1.3 The Role of Logarithmic Binning on Cloud Sizes

The noisy upper part of the cloud size distribution in Figure 4.5 affects the linear fit and β. Zhao and Girolamo (2007) and Gödde (2018) prevent this sensitivity by only including cloud sizes up to 7 km. Since they applied constant bin widths, the step function displays smaller steps in logarithmic space and the area below the plotted distribution hence does not represent the integral over the probability density. Instead, Mieslinger et al. (2019) recommended to adopt bins with exponentially increasing width, designated as logarithmic binning, so that bins are equidistantly displayed.

The variable transformation of the cloud size distribution to logarithmic bin widths $n(\log(D))$ thereby has the following effect on the slope parameter β:

$$n(\log(D)) \propto D^{\beta+1}. \tag{4.5}$$

Hence, the slope parameter in logarithmic space $\beta_{\log}$ is increased by one. Mieslinger et al. (2019) proved that the sensitivity of the cloud size distribution to bin size and fitting ranges can be significantly limited if the distribution is analysed with logarithmic binning. On top of that, the exponentially increasing bin widths allow the full range of the cloud size distribution to be taken into account. The effects of switching from linear binning, as in Zhao and Girolamo (2007) and Gödde (2018), to logarithmic space on the entire along-track cloud size distribution from the specMACS are illustrated in Figure 4.7.

Additionally considering the smallest clouds, the linear binned distribution in Figure 4.7 reveals that 60 % of all clouds observed have a measured cloud length below 200 m in specMACS which is lower than the proportion in Zhao and Girolamo (2007), who found that around 90 % of shallow cumulus clouds have this size. Nonetheless one bin holds the size information of more than half of the clouds, but has a minor impact on the power law fit. Besides shallow cumulus clouds, however, additional cloud regimes contribute to the specMACS statistics especially stemming from RF02 and RF07, which were performed in deep convective regimes.

In contrast to linear binning, the use of logarithmic binning resolves the frequency of the smallest clouds more accurately. Since the decay of the distribution is weaker for smaller clouds, a double-power law fit determined by the least residuals has been applied to the data (orange line). The slope of the cloud size distribution in logarithmic binning has values of $\beta_{\log_1} = -0.47$ and $\beta_{\log_2} = -1.7$ for smaller and larger clouds, respectively. The interception of both fits, having a value of 503 m, is referred to as scale break in literature, e.g. in Sengupta et al. (1990) and Zhao and Girolamo (2007). Mechanisms that affect the location of the scale break are widely discussed in current research. It is argued by some that the scale break is related to physical phenomena such as dynamical processes due to interactions with the boundary-layer, e.g. Sengupta et al. (1990) and Mieslinger et al. (2019). Others claim that scale breaks have an artificial origin that results from undersampling (Heus and Seifert, 2013). Regarding this dataset, the latter argument is not valid, as the decay in the size distribution slightly decreases with large clouds above 2 km. The identified scale break at around 500 m corresponds well to scale break values of around 600 m found in Zhao and Girolamo (2007) and Mieslinger et al. (2019).

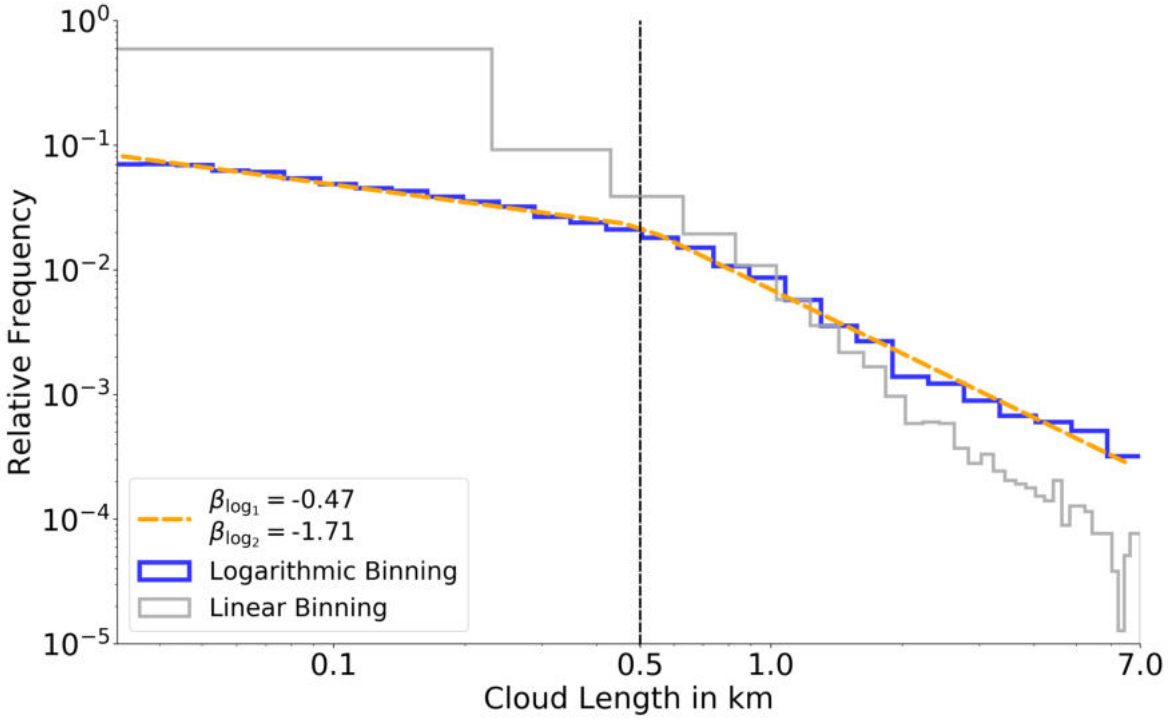

Figure 4.7: Along-track cloud size distribution based on linear binning (grey steps) and logarithmic binning (blue steps) including all clouds detected by specMACS. A double power law fit is applied to the logarithmic binning histogram indicated as orange dashed-lines. The vertical dashed line represents the scale break. The slope a double power law fit before ($\beta_{\log_1}$) and after the scale break ($\beta_{\log_2}$) are depicted in the legend. The grey histogram is equivalent to the dark-blue curve in Figure 4.5 and thus considers all specMACS clouds with linear binning but cloud sizes down to along-track lengths of 30 m are included in this plot.

4.2 Cloud Area Size Distribution

While the cloud size distributions are of high relevance in modelling shallow cloud fields in LES, e.g. Vogel et al. (2016), the effective cloud covererd area is very relevant in climatology, as it locally influences Earth's radiation energy budget. In- and outgoing radiative fluxes from the earth are significantly influenced by cloud-covered areas (Bony et al., 2015). Investigating global cloud cover from MODIS images, Wood and Field (2011) found that 15 % of the total cloud cover results from cloud sizes below 10 km. As measured by specMACS, these are the dominant size scales in the trade-wind regions, wherein the majority of clouds is even smaller. Since satellite products from MODIS are restricted to spatial resolutions between 250-1000 m (Ackerman and Frey, 2015), the contribution of subpixel clouds to the total cloud-covered area is of major interest. Although the cloud fraction seems to constitute a simple quantity, Zhao and Girolamo (2006) observed cloud fraction overestimates up to 0.18 within their case study comparing MODIS and ASTER cloud masks in trade-wind

cumuli regimes. The reasons for these differences vary from scene to scene. Using high-resolution ASTER images with 15-m resolution in Zhao and Girolamo (2007) and additional satellite images with 30-m resolution in Koren et al. (2008), it turned out that about 30% of the total cloud cover in marine trade-wind cumuli results from clouds with an area below $1\,\mathrm{km}^2$.

Even though the cloud length statistics from Section 4.1 deliver a fundamental understanding of the dominant tropical cloud sizes, the results are not necessarily representative for actual 2D horizontal cloud sizes. The reason for this is that the along-track cloud size is dependent on the flight direction and therefore cannot be used to infer the cloud area. This is one weakness compared to the definition of the area-equivalent diameter D. Since the horizontal dimension of the radar is restricted to one, the across-track view of specMACS provide an essential contribution to cloud size analysis. For that, clouds are transferred into a cartesian coordinate system in order to obtain the horizontal 2D cloud projection (Section 3.4).

In the following, this section deals with the cloud area characteristics from the specMACS cloud mask during NARVAL-II. This section is split into two parts. Before specifically analysing cloud area values, mathematical background is required, as the applied calculations are based on several assumptions and simplifications. The theoretical mathematical relations in cloud area distributions are outlined and the area calculation methods for every cloud in specMACS are described. In the second part, the results of the cloud area distribution are presented.

4.2.1 Cloud Area Determination

According to the power law characteristics of cloud size distribution based on the 1D cloud-area equivalent diameter (Equation 4.1), Mieslinger et al. (2019) verified in detail that the cloud area distribution is also based on a power law. Using the slope parameter β, the cloud area size distribution $n(A)$ is described as:

$$n(A) = a'' \cdot A^{\frac{\beta-1}{2}}, \tag{4.6}$$

where a'' differs to a by a constant factor. Referring to the Appendix for the mathematical derivation, Equation 4.6 transfers in logarithmic space to:

$$n(\log(A)) = a''' \cdot A^{\frac{\beta+1}{2}}. \tag{4.7}$$

As typical from satellite images and model simulations, cloud sizes are frequently derived by counting the number of cloud pixels. Since these cloud masks are often provided on a fixed grid with a specific resolution, e.g. 250 m for MODIS down to 15 m for ASTER (Yamaguchi et al., 1998), cloud area is determined by the product of the number of cloud pixels from each cloud and the spatial pixel resolution. Regarding downward-pointing airborne imagers however, the approach strictly fails, as spatial resolution in meters strongly depends on the flight attitude and the distance of the cloud to the aircraft. This constraint motivates the coordinate transformation applied to the specMACS cloud mask (Section 3.4) to achieve 2D geometrics for each cloud. In order to investigate the horizontal 2D cloud size distributions for the specMACS clouds, consistent methods to calculate the area of clouds are required.

In the Cartesian coordinate system, cloud contours are described as polygons with the aid of the Python library *scikit-image* (van der Walt et al., 2014). The area of each polygon is then calculated using the Shoelace formula (Braden, 1986). The Shoelace formula is a mathematical algorithm which is capable to derive the area of polygonal shapes that are described by their vertices in Cartesian coordinates. The method consists of cross-multiplying corresponding coordinates of the different vertices of a polygon to find the area of the polygon. The mathematical expression for the polygon's area A from all vertices of (x_n, y_n) is given as:

$$\begin{aligned} A &= \frac{1}{2}\Big|\sum_{i=1}^{n-1} x_i y_{i+1} + x_n y_1 - \sum_{i=1}^{n-1} x_{i+1} y_i - x_1 y_n\Big| \\ &= \frac{1}{2}\big|x_1 y_2 + x_2 y_3 + ... + x_{n-1} y_n + x_n y_1 - x_2 y_1 - x_3 y_2 - ... - x_n y_{n-1} - x_1 y_n\big| \end{aligned} \tag{4.8}$$

The fact that the constant cross-multiplying for the polygon vertices resembles tying shoelaces explains the formula's name. The reader is also addressed to Lee and Lim (2017) verifying the expansion of the Shoelace formula to a n-sided polygon through induction. Regarding specMACS, the applicability of the Shoelace formula is assured for clouds not having complex peculiarities such as internal holes within their structures. These clouds are flagged and excluded from the cloud area statistics.

Another area description is given by the elliptical fit applied to every single cloud (Section 3.7). Knowing the length of both elliptical axes, that are defined as major axis a connecting both vertices and the minor axis b perpendicular to the major axis connecting both co-vertices, the elliptical area A_ϵ is calculated as $A_\epsilon = \pi \cdot ab$. The consideration of both area definitions and their comparison also gives an assessment of the quality of the ellipse fit with regard to a valid representation of cloud shapes.

In contrast to the cloud size investigation provided by the along-track cloud size, the values of the cloud area are highly dependent on the estimated cloud height due to the coordinate transformation (Section 3.4). According to Section 3.5, the cloud projection lacks of knowledge about the across-track CTH and is set constant in the across-track direction resulting in uncertainties. Too high CTH estimates lead to smaller projected clouds, as the directional viewing vectors are multiplied by a too small scalar value and vice versa (see Section 3.4). However, if only those clouds were considered that were at least partly detected by the radar, the cloud sample would decrease by a factor of up to 80 (Figure 3.5). This justifies why, the simplifications made are still reasonable, in particular for shallow convection regimes in which CTH variability is limited due to the trade-wind inversion layer. During the crossing of the ITCZ where clouds in all heights are detected, the across-track constant CTH assumption is arguable.

4.2.2 Results of Cloud Area Size Distribution

In this section, the cloud area size distribution is analysed similar to the distribution of 1D along-track cloud size. Figure 4.8 shows the cloud area distribution from the polygonal and elliptical approach. Both distributions are based on the across-track constant height assumption. In addition, the influence of the cloud height assumptions on cloud area uncertainties is examined. In order to provide a range of very likely cloud areas values, the area of clouds is calculated for the initial estimate of CTH and for $+-$ its uncertainty of CTH defined as U_{CTH} (Section 3.6). A precise description of the robustness on individual cloud geometries to U_{CTH} follows in Chapter 7.

Inspecting cloud area size distribution based on the cloud polygons and comparing them to that of elliptical clouds, it can first concluded that both cloud area determinations reveal similar tendencies. Their resulting ranges of cloud numbers within a certain area bin is indicated by the grey-shaded pattern. Lowest mean values of U_{CTH} occur during RF03 and RF06 in shallow convection, while U_{CTH} can increase to values larger than 1000 m during RF07.

Three sectors can be identified. Focussing on both blue histograms, the distribution of cloud area values above $1000\,\mathrm{m}^2$ show characteristics similar to the double power law shape of the along-track cloud length distribution (Figure 4.2). However, for increasing cloud areas, the amplifying decay of the distribution is less abrupt and rather follows a curve than two distinct lines, so that a scale break is not that clearly pronounced and cannot be localised exactly in the cloud area distribution. Nonetheless, for cloud areas above $0.3\,\mathrm{km}^2$, the decay of the distribution amplifies significantly again.

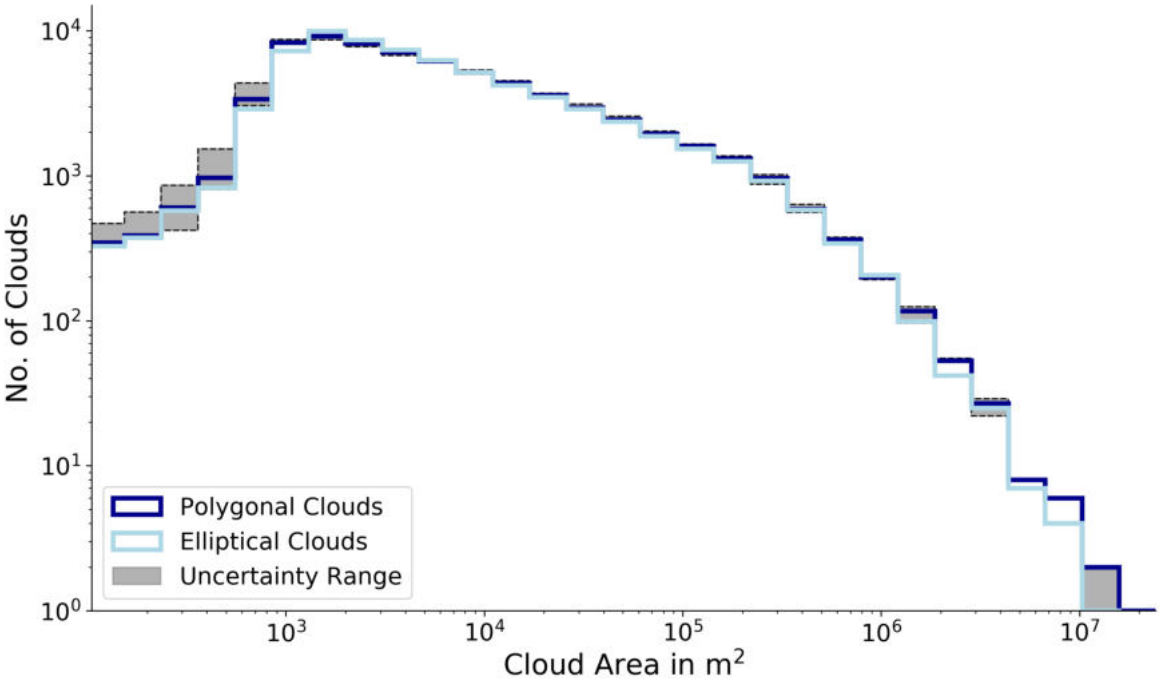

Figure 4.8: Cloud area size distribution $n(\log(A))$ during NARVAL-II with absolute number (No.) of clouds on the y-axis. The polygonal cloud area (dark-blue distribution) is calculated via the Shoelace formula. The area of its elliptical fit is also considered and its size distribution is plotted as the light-blue step function. The grey shaded pattern illustrates the variability due to the CTH uncertainty U_{CTH}.

Under the idealised assumption of circular clouds, however, a scale break would also appear in the area size distribution. According to the scale break of 500 m in the along-track distribution, the scale break in the cloud-area size distribution then should have a value around $\pi \cdot (500\mathrm{m})^2 \approx 0.75\,\mathrm{km}^2$ for circular clouds. The different locations of the decay amplification result from two reasons:

1) The along-track cloud length can significantly differ from the actual area-equivalent diameter of the clouds (on which Equation 4.5 and 4.7 are based on), as it is not evident from the along-track coordinate system how intensively clouds are elongated or oriented in a certain direction and hence differ from a circular shape.

2) Even though the along-track cloud length is just a 1D size quantity of the clouds, it has the advantage that all clouds detected by specMACS are included in the statistics. In turn, clouds extending to the edges of the FOV have to be excluded from the area determination. In particular, the larger the clouds, the higher the chance that clouds range out of the FOV in specMACS (see also Figure 4.6). This leads to an undersampling of larger clouds in the cloud area statistics, so that the increasing decay is shifted towards smaller clouds.

Regarding the uncertainty ranges for cloud area values above $1000\,\mathrm{m}^2$, it is found that, despite of high uncertainties of CTH leading to strong changes in individual cloud size, the impact on the overall cloud size distribution is minor due to the increasing bin widths. For larger clouds ($A > 1000\,\mathrm{m}^2$), where the absolute number of clouds within a bin width is comparable to the best estimate, the sensitivity to CTH is less found.

Besides the two sectors for cloud area values above $1000\,\mathrm{m}^2$, the smallest clouds ($A < 1000\,\mathrm{m}^2$) represent the third sector. On the contrary to previous sectors, U_{CTH} has a very strong effect on the statistics, as the number of clouds in a certain bin varies by several hundreds due to lower bin widths. Another question that arises is, where do these very little clouds come from. Due to the coordinate transformation, very small cloud area values do not necessarily arise from clouds consisting of one or a few pixels. For instance, at a distance between HALO and clouds underneath of 10 km, which is typically the case at a cruising altitude of 12 km and a CTH around 2 km in shallow convection, the along-track resolution of specMACS is about 18 m and 38 m in the across-track direction of each pixel. As the footprint of each specMACS pixel has an elliptic shape (Figure 3.2), the lowest cloud areas detectable for a ground speed of 200 m/s are around $\pi \cdot 7\,\mathrm{m} \cdot 38\,\mathrm{m} = 835.6\,\mathrm{m}^2$, if one considers the overlap of consecutive specMACS frames. Very small cloud area values ($A << 1000\,\mathrm{m}^2$) hence only occur if the distance between clouds and aircraft is short. This is given at low cruising levels, that were only performed close to the airport of Barbabos, and when high-level clouds were captured below the aircraft.

One corresponding example from RF07 measured by the radar and specMACS is depicted in Figure 4.9. This cloud scene represents typical conditions during RF07, as multi-layer cloud scenes were very dominant. The radar reflectivity clearly indicates a dominant cirrus cloud layer in a height of 9 km, whereas the signal of the cirrus clouds is very weak in the SWIR 1600 nm channel. This specMACS measurement period was already presented by Gödde (2018) as an instance of weaker performance of the specMACS cloud mask in multi-layer cloud scenes. Since the cirrus clouds are optically thin, shallow clouds can be visually identified below. Although the cirrus cloud radiance in specMACS is rather weak for this channel, it is dominant enough that the specMACS cloud mask shield the shallow clouds with one opaque cirrus cloud. Interestingly, these shallow clouds are also completely undetected by the radar, which also shows strong difficulties in determining the real cloud scene. Regarding the cloud area determination, the focus is on the distinct cloud patterns at the edges of the cloud mask (e.g. around 16:15:00 UTC).

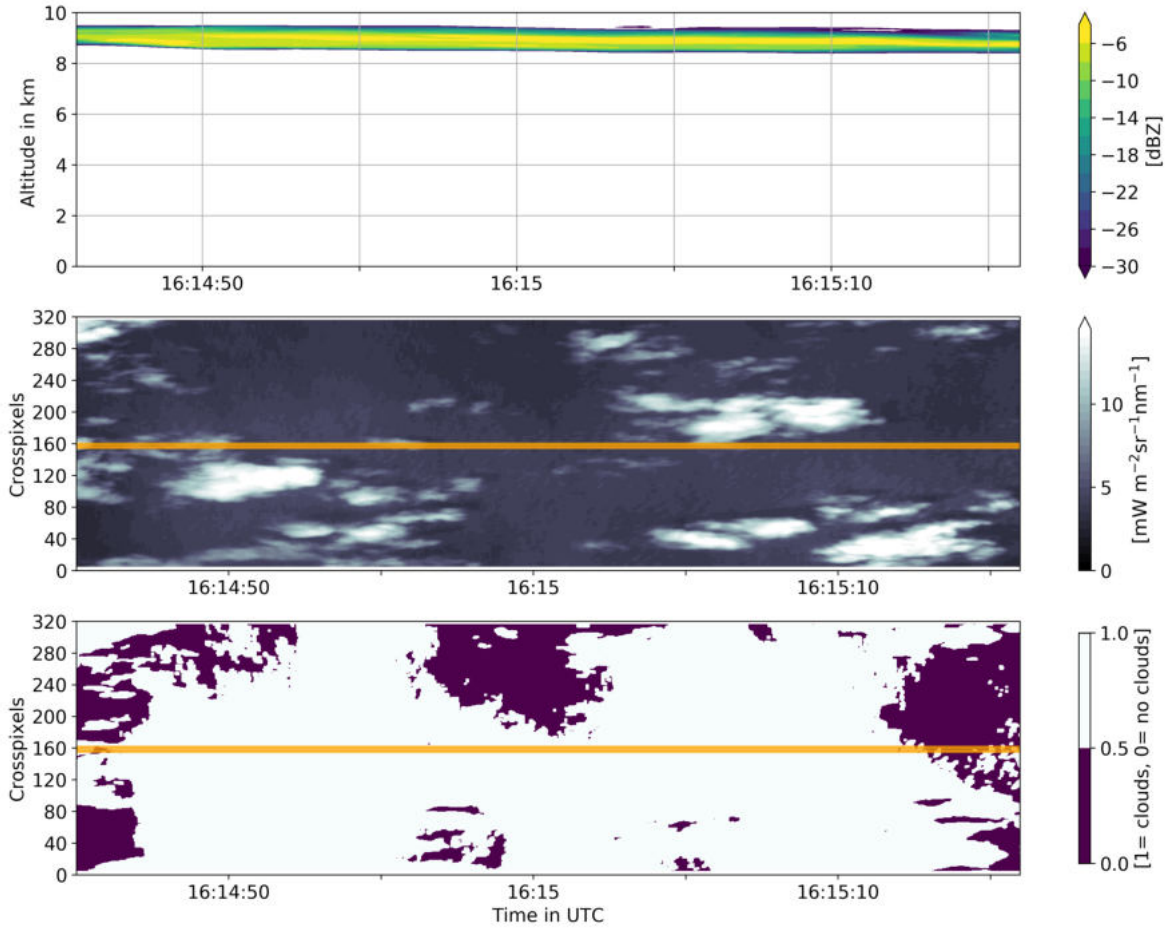

Figure 4.9: Cloud scene from RF07 for a short time period of 30 s measured by the radar and specMACS. The radar reflectivity in dBZ is depicted in the top figure. The radiance measurements from the SWIR 1600 nm channel together with the corresponding cloud mask are shown below. The orange line indicates the FOV from the radar in the specMACS cloud mask.

These fragments actually belong to the shallow clouds underneath the cirrus clouds. Since the radar did not capture them, the projection within the coordinate transformation fails due to the assumption that they lay at an altitude of 9 km and these small clouds become very small. Such situations are responsible for the very small assumed clouds. Besides, the CTH variability is very high during this flight as RF07 was partly performed in deep convection close to the ITCZ.

Motivated by the fact that around 60 % of clouds have an along-track length below 200 m (Figure 4.5) which primarly stems from shallow cumulus clouds (CTH $<$ 3000 m), the contribution of small shallow low-level clouds to the total shallow cloud coverage is investigated in Figure 4.10. According to the shown cumulative area distribution of shallow clouds, cloud sizes up to the mean area equivalent diameter only contribute 9 % to the total cloud area. The minor role of small clouds in total cloud area stands out even more for the median area equivalent diameter of 100 m.

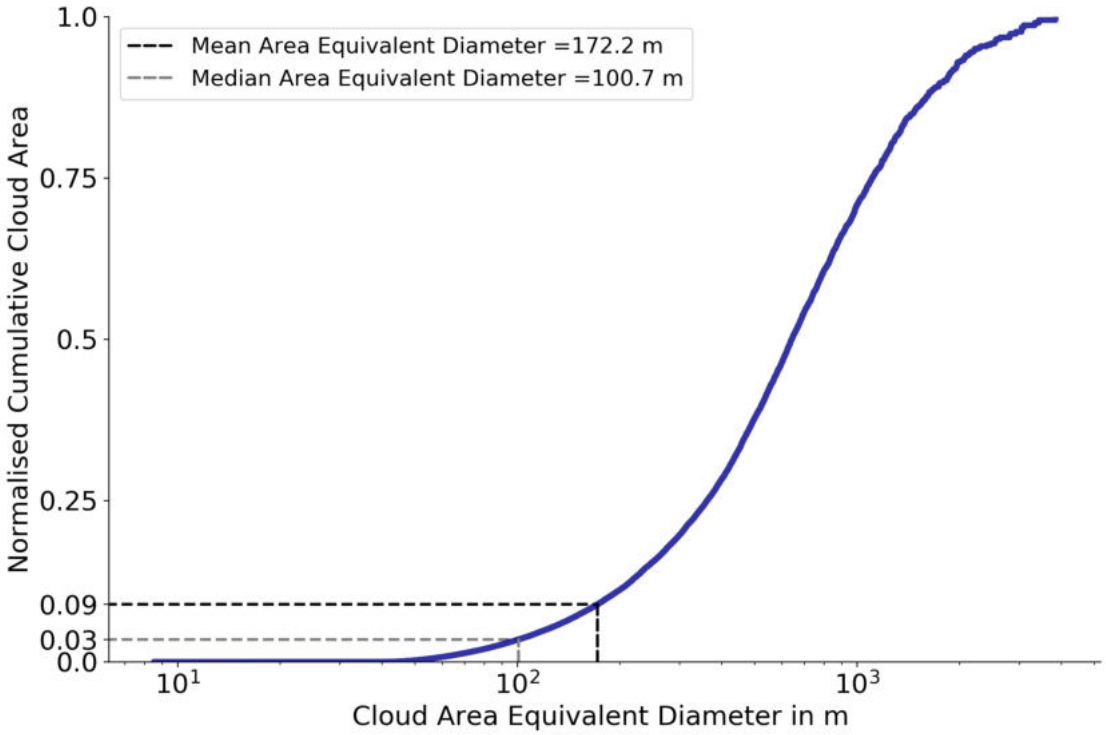

Figure 4.10: Cumulative-distribution function of the total cloud area as a function of the area-equivalent diameter D in m. The contribution of cloud sizes up to the mean (black dashed line) and the median (gray dashed line) to the total cloud cover is specified.

50 % of all observed clouds have a size of $D < 100$ m but only represent 3 % of the total cloud-covered area. In contrast to Zhao and Girolamo (2007) and Koren et al. (2008), clouds below an area of 1 km^2 ($D \approx 1129$ m) contribute more than 90% to the total cloud-covered area. However, since this analysis is confined to the fully detected clouds and hence neglects cloud areas ranging out of the across-track FOV, it must be noted that this high contribution is overestimated as largest clouds were not included. As listed in Table 4.1, the contribution to the total cloud cover area by the smaller half of clouds is rather constant during all shallow convection flight scenes.

Table 4.1: Statistics of D for shallow clouds (CTH below 3000 m) for the considered RFs based on mean and median area-equivalent diameter D_{mean} and D_{median} respectively, and their contribution Con to the cumulative area.

Research Flight	Number of clouds	D_{mean} in m	D_{median} in m	Con D_{mean}	Con D_{median}
RF02	4658	132.4	75.9	0.08	0.03
RF03	13805	200.0	117.2	0.09	0.03
RF04	5500	168.7	97.9	0.09	0.03
RF05	2632	156.6	85.5	0.09	0.03
RF06	9884	167.5	102.9	0.1	0.04
RF07	4208	151.7	94.3	0.1	0.04

Based on mean and median values of Table 4.1, larger shallow low-level clouds are present during RF03. The high number of shallow cumulus clouds and the frequent dropsonde releases during RF03 and RF06 awakes the interest for further studies of the interaction between shallow clouds and their environment in the trade-wind BL.

4.3 Single Cloud Shape

The increasing resolution of meteorological satellite products enhances the interest in cloud shapes and especially in the interaction of tropical cloud structures with the BL. Simple descriptions of cloud shapes, however, still facilitate investigations on the coupling between clouds and circulation and enable the intercomparison of different cloud scenes. The tropical cloud scene study based on MODIS images from Stevens et al. (2019c), labelling mesoscale cloud patterns as *Sugar*, *Flower*, *Gravel* and *Fish* represents one current study about classifying tropical marine cloud shapes.

Referring back to the airborne observations during NARVAL-II, this section deals with the individual cloud structure by investigating the shape complexity of the tropical shallow low-level clouds. Section 4.3 investigates whether individual clouds have mostly similar shapes as claimed in Stevens et al. (2019c) and reveals the impacts of the elliptical cloud shape simplification from another shape perspective.

4.3.1 The Relevance of Individual Cloud Shape Complexity

Mesoscale cloud patterns as examined in Stevens et al. (2019c) are too large for the FOV of specMACS. However, since mesoscale clouds develop from small-scale clouds, an investigation of the individual cloud shapes represents a scientifically relevant component, i. e. as the small cloud structures in specMACS are unresolved in MODIS. The characterisation of single cloud patterns is here established in a more mathematical sense than in the phenomenological approach of Stevens et al. (2019c), as clouds from specMACS are also described as ellipses. Although the elliptical fit facilitates further geometrical cloud analysis and although the cloud-area size distributions (Figure 4.8) point out that the elliptical fit marginally affect the overall statistics, the cloud shape complexity subsequently disappear from the specMACS cloud dataset. For several clouds, an ellipse certainly does not fit to their actual shape. Three of those shallow cumulus clouds are paradigmatically illustrated in Figure 4.11. While the area of the clouds and their ellipses are similar, the actual shapes are far from their elliptical fit. This also lead to questionable orientations of the semi-major axis.

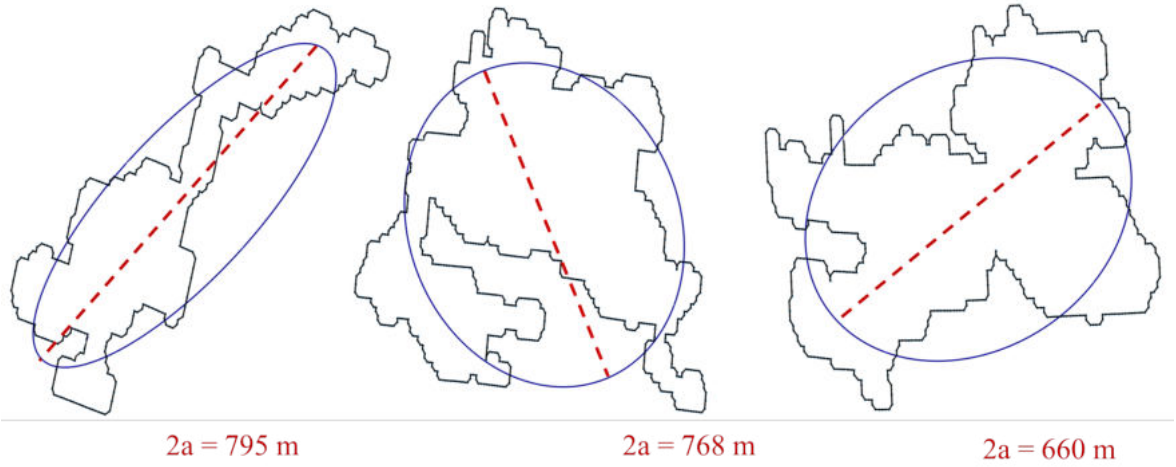

Figure 4.11: Polygons of three exemplaric clouds detected during RF06. Black curves represent cloud contours from the specMACS cloud mask. The blue curve are the least-square fitted ellipses from the vertices of clouds. Depicted clouds are not true to scale, although of similar size as the values of the elliptical major axis $2a$ (red dotted line) show.

On the scale of individual clouds, cloud complexity is an essential field of research regarding Earth's radiation budget. The sharp distinction between cloud-free and cloudy pixels (the shift between clear and cloudy skies) is relevant due to the twilight zone – a gradual transition zone that depends on both the presence of nearby clouds and aerosols that show subordinary reflectance effects.

In that context, Zuidema et al. (2008) focusses on the shortwave radiation impacts from marine shallow cumulus clouds, using typical cloud structures for shallow cumulus and stratiform marine clouds based on the ATEX and Barbados Oceanographic and Meteorological Experiment (BOMEX) campaigns. As highlighted in Hinkelman et al. (2007), geometric anisotropies of cloud fields can cause substantial impacts on the domain-averaged solar fluxes. In addition to the impact of 2D inhomogenities, Song and Min (2011) found significant impacts of three-dimensional (3D) cloud structures in predominant wind shear on atmospheric heating-rate profiles.

Basically, shape complexity represents a subjective term. The question is which cloud shape can be classified as complex and what is its actual degree of complexity. Mathematical definitions are required to distinguish between degrees of cloud complexity and which accord well with humans intuitive understanding of shape complexity. In the following, the cloud shape complexity is investigated by two approaches.

4.3.2 Cloud's Fractal Dimension

The fractal analysis method is a powerful mathematical tool to determine the complexity of geometrical objects and was first provided by Lovejoy (1982). It quantifies the general shape complexity and self-similarity of clouds by scaling the relationship between the cloud perimeter U and the cloud area A, as follows:

$$U \propto A^{\frac{\delta}{2}}, \tag{4.9}$$

with the exponent δ being the fractal dimension.

Regular shapes such as circles have a fractal dimension of 1. A cloud field consisting of circular clouds would hence reveal a fractal dimension value of 1. Values around two, however, would be found for very complex and furrowed clouds. With the aid of the fractal dimension, the geometrical complexity of tropical clouds has recently been investigated in several studies using satellite images, e.g. Benner and Curry (1998), Zhao and Girolamo (2007) and Mieslinger et al. (2019). While older studies were constricted to the coarser resolution of satellite products (around 1 km), Zhao and Girolamo (2007) and Mieslinger et al. (2019) examined cloud geometries from ASTER. Due to the similar resolutions, their study motivates an analogue geometrical cloud analysis using the specMACS. Coming from a meteorological perspective, δ may provide insights into the underlying dynamics influencing the cloud shapes, although it does not uniquely define the cloud shapes.

According to Equation 4.9, the cloud perimeters are required from specMACS. Making use of the polygonal description of the cloud border, the perimeter is derived as the length of the polygon. The vertices of the cloud polygon are sorted clockwise, so that the perimeter is discretised by the distances between the consecutive vertices. From this, the fractal dimension of the entirely captured clouds is derived by displaying both geometric quantities A and U in a double logarithmic scatter plot. A least-square fit is applied to the points whereby the slope reveal an approximination of the fractal dimension δ.

The results of the fractal dimension analysis for specMACS are illustrated in Figure 4.12. Focussing on the left plot at first, the distribution of A and D values shows a dependency on the CTH. The distribution of cloud perimeter and area values indicates multimodal characteristics. For low-level clouds having a CTH below 3000 meters, the distribution shows a clear pattern and regularity.

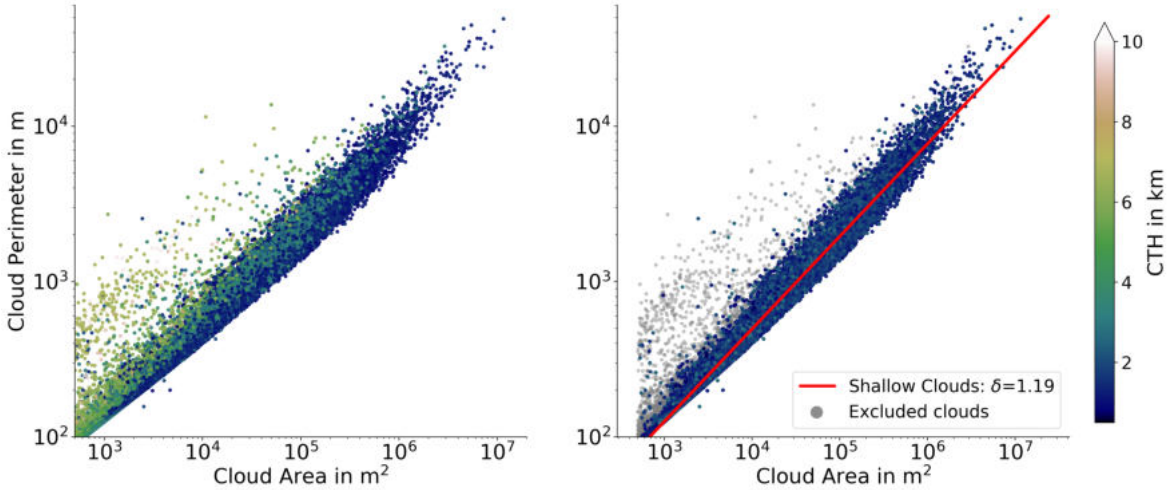

Figure 4.12: Left: area in m^2 and perimeter in m relation both on logarithmic axes for each cloud. The colourbar indicates the CTH. Right: Same clouds and fractal dimension for clouds with CTH below 3000 m (blue dots) from least-square linear fit (red line). Grey dots represent the clouds excluded from the fractal dimension analysis.

For higher clouds, on the other hand, the perimeter is larger compared to equivalent cloud area values in lower altitudes. Higher clouds are supposed to have more complex patterns compared to those of same area in lower levels. However, this is a misinterpretation and is more related to the across-track CTH projection error - especially if clouds overlap each other. If low-level clouds, primordially having a cumulus structure, are erroneously projected to high levels, the coordinate transformation (Section 3.4) leads to unrealistic and small cloud patterns. Together with the height-decreasing observation domain, this restricts the representativity of δ for clouds in higher altitudes. The FOV from specMACS is fast limited to less than one kilometre at great CTH. The sample size of high-level clouds being detected in their complete extent is an underestimate due to the lower probability of appropriately recording high clouds without their edges being cut of.

Hence, although Batista-Tomás et al. (2015) found promising differences of the fractal dimensions between different cloud types by observing satellite images of tropical marine cloud fields, this fractal dimension study only focusses on clouds with CTHs below 3000 meters. For the shallow low-level clouds, the linear regression analysis derives a fractal dimension of $\delta = 1.19$, which is equivalent to that found by Mieslinger et al. (2019). For the smallest clouds, however, the fractal dimension is sensitive to the pixel shape and to the perimeter algorithm. As the polygons are created from the contours of the cloud mask with a threshold of 0.5, the shape of clouds is different if, for example, the cloud border is defined as the line segments connecting the centres of cloud edge pixels. For cloud areas $> 1\,km^2$, δ increases to 1.35.

Although the fractal dimension values from specMACS during NARVAL-II and Mieslinger et al. (2019) are rather low compared to other studies, e.g. Sengupta et al. (1990), their match reveal the representativity of tropical low-level cloud geometries from specMACS. However, it has to be kept in mind, that the sample from NARVAL-II is considerably smaller than those of the ASTER studies. Specifically, the number of clouds analysed from specMACS is more than two orders of magnitude smaller than those of Zhao and Girolamo (2007). Compared to their study, the pearson correlation coefficient between cloud area and perimeter is rather low with a value of 0.60. The lower correlation results from the low-level clouds during RF02. The exclusion of the clouds from RF02 lead to higher correlation value of 0.9 similar to the correlation coefficient of 0.87, found by Zhao and Girolamo (2007). The low δ implies that clouds are rather compact and smooth in shape.

4.3.3 Complexity of Single Clouds

The fractal dimension only provides an overall statistic of the cloud shape similarity. Instead, cloud complexities can vary significantly between individual clouds. If all clouds would ideally have a elliptic shape, the fractal dimension would have a value of $d = 1.0$ in turn. An ellipse represents a compact and convex geometric object and is of course only a simplification of the cloud shape. Thus, this section investigates the deviation of the cloud shapes to their convex hulls.

The analysis makes use of the methods provided by Brinkhoff et al. (1995) who developed a quantitative description of spatial complexity referencing to their convex hull. Specifically, Brinkhoff et al. (1995) established a combined quantity that takes into account the deviation of a given object to its convex hull (area comparison), the frequency of vibration (counting the concave connections between vertices) and the amplitude of the vibration (comparing the perimeter of the object to its convex hull). In the following the relevant parameters from Brinkhoff et al. (1995), namely the amplitude of vibration, the convexity and the frequency of vibration are shortly introduced:

The amplitude of vibration AP: AP is defined as the relative difference between the perimeter of the considered object and the perimeter of its convex hull. Equivalent to convexity, a convex object has an amplitude value of $AP = 0$, whereas $AP = 1$ represents the unreachable upper limit.

Convexity *CV*: CV is defined as the relative area error of the polygonal object to its convex hull. High deviations lead to convexity values theoretically rising up to 1.

Frequency of vibration *FQ*: The vibration of polygonal objects is quantified by the changes in direction of the lines between vertices. Assuming clockwise sorted vertices, then the changes in the directions of lines between consecutive vertices will always be right-directed for a ideal convex object and the interior angle at the edge is larger than π. If however the change is left-directed and interior angle larger than π and the vertex is labelled as a notch (Figure A.1). The frequency of vibration hence considers the number of notches normalized by the number of vertices minus three being the upper limit of possible notches for a compact object. Extremely, the vibration is a continuous change in direction from left to right so that the normalized number of notches $notches_{\text{norm}}$ is 0.5 in a maximised frequency of vibration. If no notches are present, the polygon is convex and smooth. But also high values of $notches_{\text{norm}} > 0.5$ can indicate smooth cloud contours.

Combining the parameters, Brinkhoff et al. (1995) empirically defines complexity C as:

$$C = 0.8 \cdot AP \cdot FQ + 0.2 \cdot CV, \tag{4.10}$$

where the combined effect of FQ and AP is considered by their product.

The algorithm has the main advantage against δ that every cloud can be individually analysed regarding its complexity. Zero values of C represent trivial convex objects, whereas a complexity above 0.4 already appears for very complex objects. Brinkhoff et al. (1995) applied the algorithm to the polygonal border lines of the countries on Earth, finding that 98 % of the European countries (with a mean number of vertices of 84) have a complexity below 0.4.

For the purpose of this cloud analysis study, complexity characteristics on clouds are exemplary illustrated in Figure 4.13. The depicted clouds are identical to those in Figure 4.11, but the vertices are enlarged. The values of the complexity parameters are given. While the second cloud also has the highest AP, the first cloud has the highest CV. Regarding the individual parameters, it is found that FQ exceeds 0.9 for all three clouds, having the highest value for the last cloud. The second cloud has the highest overall complexity with a value of $C = 0.427$.

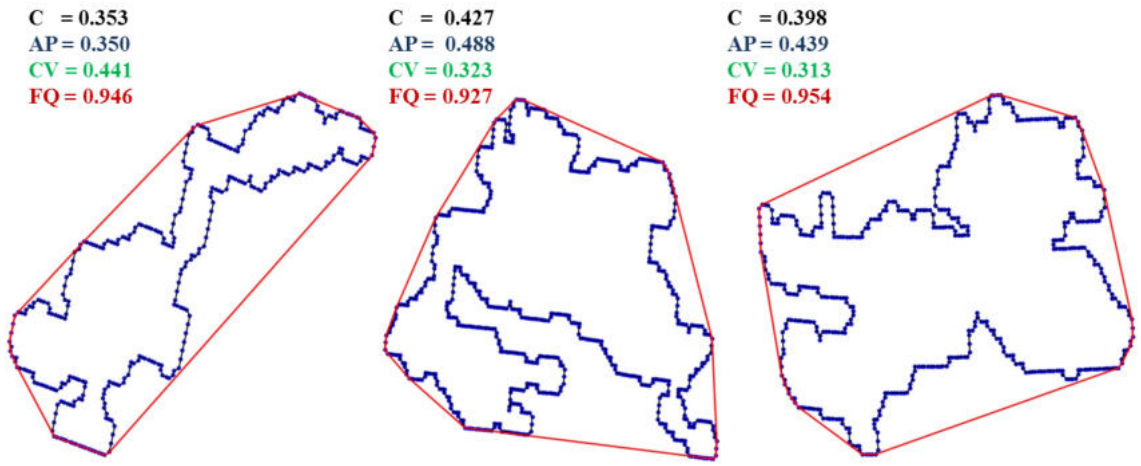

Figure 4.13: Cloud complexity values for the clouds depicted in Figure 4.11 based on their convex hull plotted as red lines. The vertices of each polygonal cloud are enlarged and indicated as blue dots. The complexity parameters follow the terminology of Equation 4.10.

From the exemplary complexity values it is concluded that the complexity algorithm presents a suitable tool to characterise the complexity of individual clouds, as it distinguishes between different parameters on shape complexity and accords well with the intuitive and visual understanding of shape complexity. The three parameters allow detailed identifications on the dominant deviations to a non-complexe cloud, may it be an ellipse or any other convex hull.

The overall complexity statistics for all shallow low-level clouds (CTH $< 3000\,\mathrm{m}$) having an area-equivalent diameter D above 100 m are presented in Figure 4.14 as kernel density (KDE) plots. As visible from the upper distribution of C (defined in Equation 4.10), cloud complexity values above 0.4 are barely found in the dataset, so that the exemplaric clouds of Figure 4.13 rather represent extreme cases. The mean complexity of the clouds has a value of 0.15. The overall distribution of C resemble a Weibull distribution.

The distributions AP and CV also show Weibull characteristics, wherein the fitting Weibull coefficients depend on the lower threshold of the included cloud sizes. For $D > 100\,m$, the curves of the individual parameters are similar to that of C. Including all clouds, however, the probability distributions of complexity values decay exponentially. This results from the fact, that small clouds with $D < 100\,\mathrm{m}$ represent half of the data set and their shape complexity is restricted due to the resolution of specMACS. Polygonal clouds having less pixels which is aligned with less vertices. They cannot have as high complexity values as the clouds presented in Figure 4.13.

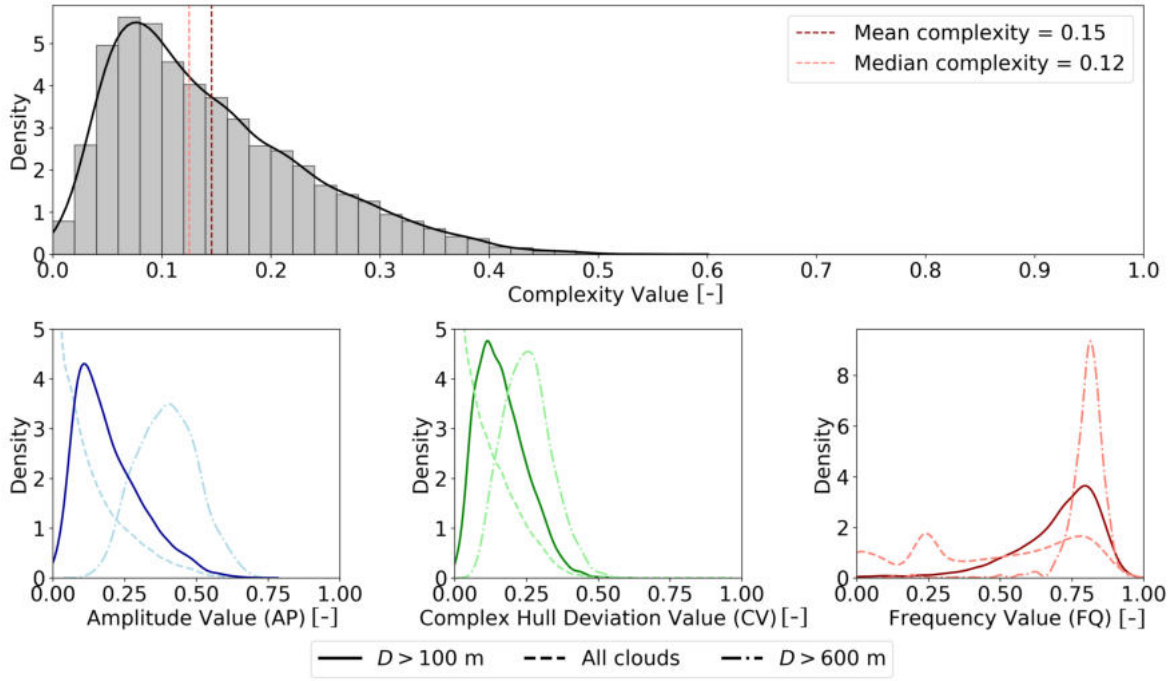

Figure 4.14: Distribution of shape complexity values for the shallow low-level cloud sample from specMACS during NARVAL-II illustrated as KDE plots. The upper plot shows the probabilty distribution of the complexity values C for all clouds . The three lower plots depict the kernel distribution estimates for the individual complexity parameters AP, CV and FQ given on the x-axis. Solid lines are distributions based on clouds having an area-equivalent diameter $D > 100\,\mathrm{m}$, dashed lines on the whole cloud sample and the dashed-dotted lines on clouds with $D > 600\,\mathrm{m}$.

The pearson correlation coefficient between cloud pixel number and complexity C hence has a value of 0.51. In particular, the probability distribution shifts to higher AP values for larger clouds (as depicted for $D > 600$ larger than the scale break found in Figure 4.7). This correlation has to be taken into account for further analysis, where the geometrical cloud structure is investigated with respect to the atmospheric boundary conditions. It is assumed that the dominant wind-field, i.e. wind speed and wind shear, have a dominant impact on geometrical cloud structures as found in LES, e.g. Neggers et al. (2003) and Chen et al. (2015). However, this is insignificant in the specMACS data, as the resolution effects dominate.

Chapter 4 quantified the cloud geometries during NARVAL-II with a focus on the shallow low-level clouds, mainly consisting of shallow cumulus. Cloud sizes have been quantified in one dimension based on the along-track coordinate system. The two-dimensional cloud size analysis with regard to cloud area size distribution required the specMACS clouds to be projected into the Cartesian coordinate system.
Main findings of this chapter are summarised:

- The across-track FOV from specMACS significantly affects along-track cloud size statistics. In particular, the contribution of small clouds increases. The vast majority of clouds is very small. 60 % of all clouds from specMACS have an along-track cloud length below 200 m (at sub-grid scale for the radar).
- Along-track cloud size and cloud area distributions have double power law characteristics with a pronounced scale break around 500 m in the along-track perspective.
- The median area-equivalent diameter of shallow low-level clouds has a value of 100 m but the smaller half of clouds only contribute less than 10 % to the total cloud area in shallow convection regimes.
- Cloud shapes can simplified by ellipses. Overall, the elliptical fit of clouds well represents the cloud area characteristics.
- Clouds are rather smooth in shape. Their fractal dimension has a value of $\delta = 1.19$ but increases to higher values ≈ 1.3 for the largest fully detectable clouds.
- The complexity of cloud shape increases with cloud size and is mainly pronounced by deviations of the perimeter compared to a convex hull. The role of measurement resolution is not negligible.

5. The Cloud Field and its Organisation

Plank (1969) already observed from airborne measurements that the spatial distribution of shallow cumulus clouds becomes clustered during daytime. After Chapter 4 provided understanding of individual cloud characteristics and discussed their statistics, Chapter 5 now regards the cloudy scenery from specMACS as a coherent self-interacting system in order to examine cloud organisation. It discusses the capabilities of airborne remote-sensing from NARVAL-II for cloud organisation studies. Two of the most common satellite-based indexes to quantify cloud organisation are depicted. Their concept and applicability to airborne measurements from NARVAL-II is debated.

The horizontal FOV from specMACS, however, is restricted to less than 10 kilometres in the across-track direction, which is more than two orders of magnitude smaller than typical satellite products from spectral imagers. It is investigated whether the clouds show organisation phenomena such that clouds tend to appear in clusters or whether the sampled clouds are randomly distributed.

5.1 Quantification of Cloud Organisation

The quantification of cloud organisation enables comparability between different observational case studies of cloud scenes. This section deals with two common cloud organisation indexes, namely the Organisation Index (I_{org}), which was introduced by Weger et al. (1992) and found its current definition in Tompkins and Semie (2017), and the Simple Convective Aggregation Index (SCAI) from Tobin et al. (2012). Both indexes are widely used in satellite-based studies of 2D images. They consider the distance of cloud-pairs to determine the degree of organisation and are sensitive to the number of clouds. However, as sketched in Figure 5.1, the consideration of the connected cloud pairs differs between both indexes.

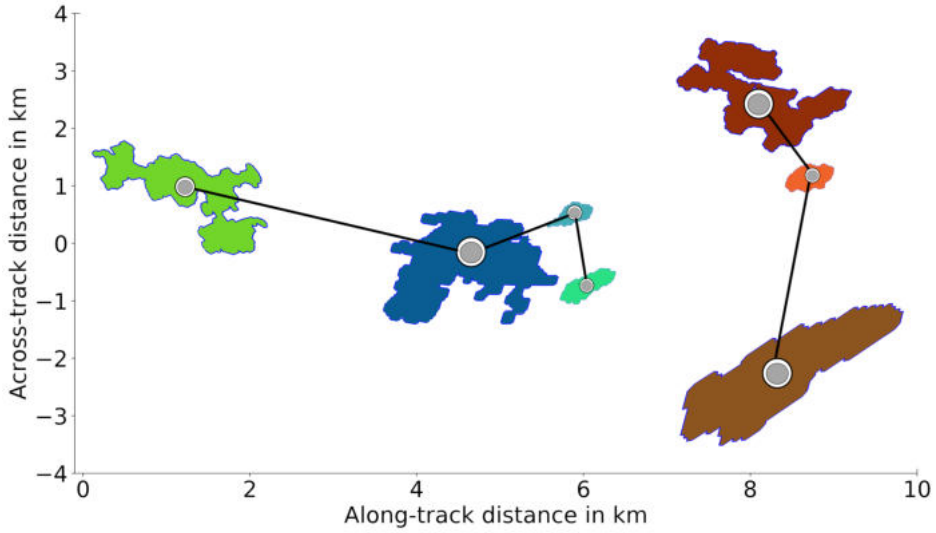

(a) Nearest Neighbour Connectivity (I_{org})

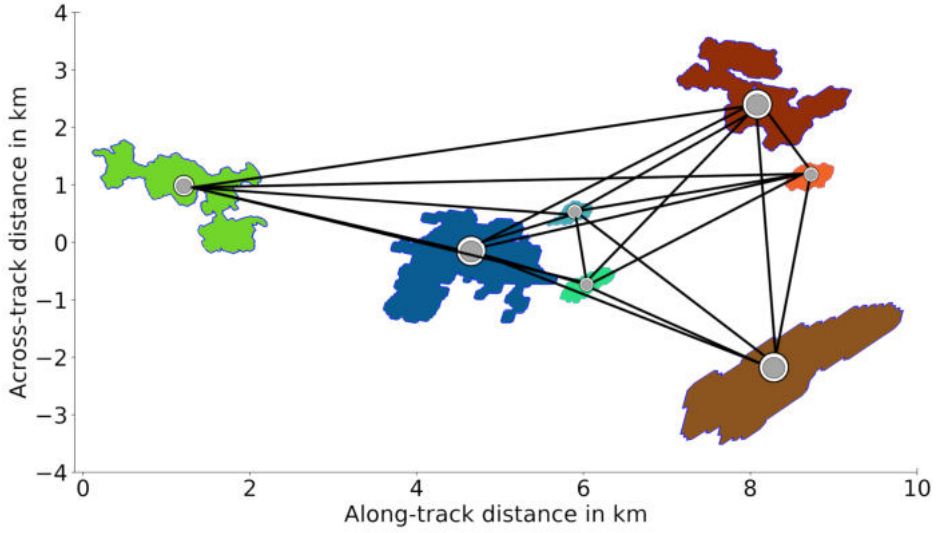

(b) Euclidean Distance Connectivity (SCAI)

Figure 5.1: Connectivity methods of cloud-pairs established in both organisation indexes, I_{org} (top figure) and SCAI (bottom figure), shown for a fictional cloud scene typical in the specMACS viewing perspective.

While the I_{org} examines the distance from the centroid of each cloud to its nearest neighbours (NN), the SCAI takes into account the average distance between all clouds, in a way that the euclidean distance is calculated for all possible pairs of clouds. This leads to a much larger number of cloud-pair distances considered from the SCAI.

The I_{org} aims to distinguish between several states of cloud organisation (namely clustered, aligned, regular or random cloud distribution) and to thereout describe its degree of intensity. In order to achieve this from the NN distances, the cumulative density function of nearest neighbour distances (NNCDF) is compared to that of a random process, as graphically indicated by the brown curve in Figure 5.2.

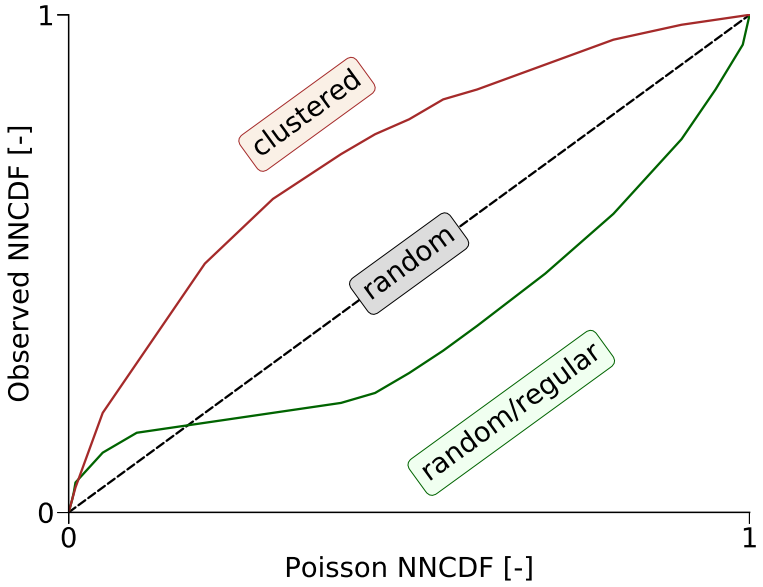

Figure 5.2: Graphical derivation of I_{org} from NNCDF for two fictive curves. The domains of the different organisation regimes are depicted with colours.

For a random process, the distribution of the NN distances of cloud-pairs can be described by a Poisson point process (Sengupta et al., 1990). Based on this assumption, the random $NNCDF_{\text{Poisson}}$ exhibits a Weibull distribution according to:

$$NNCDF_{\text{Poisson}} = 1 - \exp^{\lambda \pi l_n^2}, \tag{5.1}$$

λ is a normalisation factor and corresponds to the number of pixels per unit of area. l_n represents the NN distance of clouds referring to their centroid. The observed NNCDF of the cloud scene is hence compared to those of the random process from Equation 5.1. If the observed NN distances are on average larger than in the Poisson point process, the cloud scene is deemed regular. Otherwise, if distances are smaller than assumed from the random distribution, meaning that more clouds are very close to each other, the scene is considered to be clustered.

Inspecting Figure 5.2, the I_{org} is inferred from calculating the integral of the brown curve, ranging from zero to one. For randomly distributed clouds, the observed NNCDF lies on the diagonal. According to its integral, the I_{org} will hence have a value of 0.5. In clustered cloud scenes, the curve lies above the diagonal and the I_{org} is larger than 0.5. Regular cloud scenes are characterised by an I_{org} below 0.5. However, the I_{org} value can be misleading and may be the result of a cancellation as it is an integrated quantity. Therefore, Tompkins and Semie (2017) recommend examining the entire graph of the NNCDF due to the variability of cloud organisation on different scales, as shown by the green curve in Figure 5.2. Nonetheless, the I_{org} is unambiguous for different resolutions which allows the comparison among different datasets.

In contrast to the I_{org}, the SCAI considers the euclidean distances between clouds as decisive cloud organisation criterion and increases with the number of included clouds. Both parameters are normed by characteristic scale values as they depend on the investigated domain size and the spatial resolution. These are the maximum possible number of clouds within the domain and the diagonal length of the domain. A high degree of cloud aggregation leads to lower, and a disaggregated cloud scene to higher SCAI values, respectively (Tobin et al., 2012). Theoretically, as the SCAI can increase by one parameter independently from the other, different cloud scenes can merge into the same SCAI. In turn, both parameters partly counteract. On the one hand, if a cloudy shallow cumulus scene within a certain domain is composed of many clouds, the high number of clouds will significantly raise the SCAI, revealing a disaggregated cloud scene. On the other hand, a high number of clouds within a certain domain leads to lower cloud distances on average. This would rather cause the SCAI to remain stable or to even decrease. The comparison between several studies has nonetheless shown that the general magnitude of SCAI is significantly affected by the domain size and the resolution. In Tobin et al. (2012), SCAI values range from 0 to 30, whereas those of Mieslinger et al. (2019) are generally two magnitudes of sizes lower, although both studies investigate the spatial cloud distribution from horizontal satellite products. Mieslinger et al. (2019) and Kadoya and Masunaga (2018) critically highlight the significant alone-standing correlation of the number of clouds and the SCAI value, so that the SCAI is practically a measure of the cloud number.

For the sake of completeness, two other organisation indexes, using the concepts of I_{org} and SCAI in a modified version, are mentioned without further specification. These are the radial distribution function (RDF), used in Rasp et al. (2018), and the Convection Organization Potential (COP) (White et al., 2018).

5.2 Applicability of Organisation Indexes to Airborne Cloud Observations

Since both approaches, the SCAI and the I_{org}, are optimised for satellite-based observations, their applicability to quantify cloud organisation regarding airborne datasets from specMACS and the radar is discussed. The I_{org} is mostly used for horizontal satellite images in which the examined cloud scene consists of a large domain ($> 1000\,km^2$), either by one snapshot (geostationary) or during a fast overpass (polar-orbiting). Two general aspects have to be considered when comparing organisation indexes gained from specMACS to those from satellite products (e.g. Mieslinger et al., 2019):

- In the along-track, it requires a long time period to reach an observed distance similar to scales from satellite images. Thus, the resulting considered cloud scene can no longer be considered as one coherent system.
- The across-track FOV from specMACS is hardly ever above 10 km. Each index rather describes the organisation of clouds along the narrow flight path and not the actual organisation of the cloud scene in its entire horizontal extension.

Concerning both aspects, the SCAI analysis is not applied in the horizontal plane as its euclidean distance approach is not appropriate for the narrow flight path. The airborne-based cloud field strongly differs from cloud scenes in typical spatial domains of satellite images. The characteristic length scale L_c, being the diagonal line of the cloud scenery and necessary for the SCAI, becomes unrealistic high, as the sampling domain is narrow but very far-reaching. If the SCAI was instead calculated only for shorter temporal ranges (e.g 5-min periods), L_c would decrease.

However, projection errors resulting from erroneous CTH estimates within the coordinate transformation (Section 3.4) can significantly affect the results as the SCAI considers the geometrical distances between all clouds (Figure 5.1). Apart from that, the strong influence of the domain and pixel size on the SCAI values is always problematic for the comparison to different resolutions. In return, it is generally possible to apply the SCAI to the radar cloud mask in order to investigate the organization with respect to the vertical structure of the clouds as conducted to satellite images by (Stein et al., 2017).

Since the I_{org} only takes into account the nearest neighbour distances between paired clouds, the impact of projection errors and of the narrow flight path are reduced. Nonetheless, as sketched in Figure 5.3, limits for representative airborne-based values of NN distances occur in case of cloud streets orientated perpendicular to the flight heading. Such elongated wind-parallel cloud streets, which are frequently visible in mesoscale satellite images, are rather composed of small, distinct and similar clouds in zoomed perspective (Stevens et al., 2019c). Figure 5.3 sketches a fictional scene of such similar clouds forming two cloud streets above the ocean, while HALO overpasses this scenery, holding a constant flight level and heading. Since only one cloud from each cloud street is detected, the NN distance, which is obtained from the specMACS data (red distance) does not represent the actual distance between the clouds within the cloud streets (black distances).

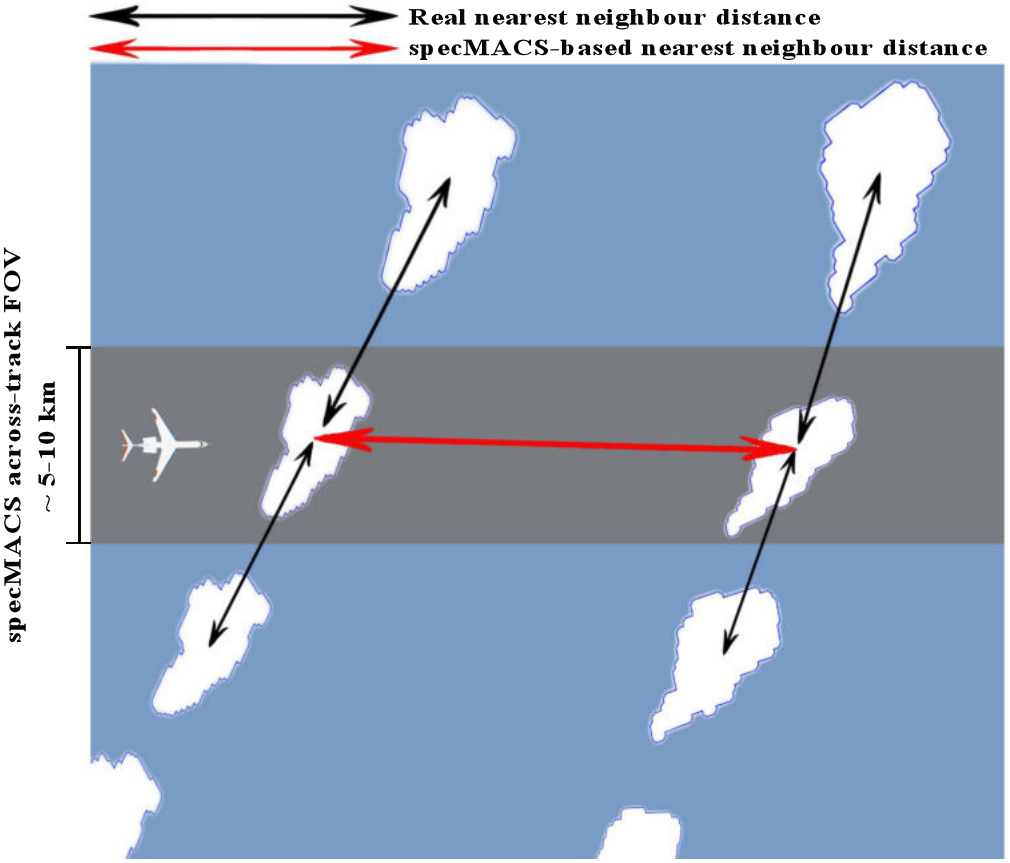

Figure 5.3: Scheme of cloud streets perpendicular to the flight course of HALO from satellite perspective.The FOV of specMACS is illustrated as grey rectangle. The NN distance calculated from specMACS (red arrows) is shown in contrast to the real NN distance of the clouds (black arrows).

Strictly speaking, the organisation analysis is hence directly dependent on the flight course and will lead to a sampling error if there is a tendency of aligned cloud streets. The formation of clouds streets is signifcantly enhanced by increasing wind speeds and wind shear. During NARVAL-II campaign the vertical structure of the trades in shallow convection regimes was however rather stable and wind shear was low (Figure 2.7), so that atmospheric conditions were not ideal for cloud streets.

This sampling error is decreased, the higher the aircraft and the lower the clouds. As discussed in Section 4.1.1, the vast majority of clouds is also significantly smaller than 5-10 km at least in the along-track direction, which is why the sketch of Figure 5.3 can be seen as a worst case revealing the limits of the perspective from specMACS. In addition, the unambiguousness of the I_{org} to domain size and resolution by its definition is the major strength of this index. For the I_{org}, the measure of the NN distance is pixel-based and not geometrical as for the SCAI. According to Equation 5.1, the Weibull distribution, which is related to the actual NNCDF, refers to the pixel number from the cloud mask.

Thus, the determination of the I_{org} for the specMACS cloud mask can be applied under consideration of the following aspects and uncertainties:

- If the distance between clouds and HALO is relatively constant, the pixel-based approach can be considered as valid, as the pixels correspond to rather similar distances and the projection error remains small. For RF03 and RF06, performed in shallow convection regimes, the I_{org} can be deemed as more accurate compared to RF07, where the CTH is more variable.
- For a constant CTH, the projection is still influenced by strong descent or ascent and also during flight curves. Data from critical flight manoeuvres is filtered out.
- Along-track pixel distances depend on aircraft speed. Apart from the critical flight manoeuvres, the aircraft speed varies little.
- In case of data gaps such as those resulting from window freezing, the pixel based approach neglects larger distances. The calculation is then split into periods.

In general, indexes focussing on distances between the centroids of clouds are crucial, as larger neighbouring clouds would be characterised by higher nearest neighbour distances even if the distances to their borders are very small (White et al., 2018). In other words, large clusters are always less aggregated than small clusters. Thus, it is recommended to slightly modify the cloud distance definition, by subtracting the sum of clouds radii from the distance between two clouds.

5.3 Results of Horizontal Cloud Organisation

In the following section, the spatial cloud organisation for the NARVAL-II flights is examined and compared to values from literature. The degree of cloud organisation in the horizontal perspective is quantified using the I_{org} with respect to the NNCDF defined in Section 5.1. The I_{org} is calculated following Equation 5.1, taking into account critical flight manoeuvres and checking for data gaps in the specMACS cloud mask. Accordingly, Figure 5.4 depicts the NNCDF for all flights and refers them to a random process, characterised by the Poisson cumulative density function. For all investigated flights and over all scales, the curves lie above the diagonal line representing the upper threshold to regular or random cloud arrangement. This indicates that the cloud fields are overall robustly clustered even in shallow convection (predominant during RF03 and RF06). As stated in Section 5.1, clustered organisation manifests in I_{org} values above 0.5. Between flights, the values vary only within a narrow range of ± 0.11.

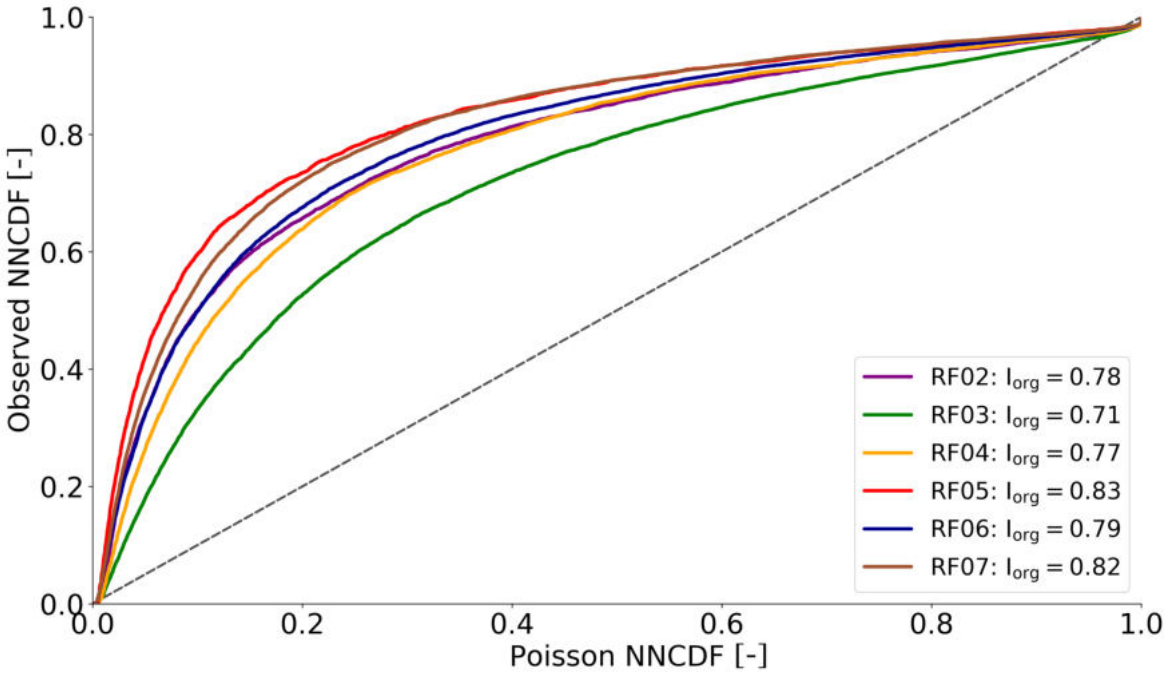

Figure 5.4: NNCDF considering the centroids of clouds related to Poisson NNCDF, analysed for each RF using specMACS. I_{org} values are listed in the legend representing the mean degree of cloud organisation for each flight.

The lowest mean I_{org} is found for RF03 having a value of 0.71, which was performed in a very dry atmosphere, and the highest mean values (I_{org}>0.80) are found for RF05 and RF07. Investigating the ASTER-based marine shallow cloud organisation over the Western Tropical Atlantic and the Eastern Tropical Pacific (within $10 - 30°$N and $40 - 180°$W), Mieslinger et al. (2019) also found stable I_{org} values but slightly above those from specMACS, ranging from 0.87 to 0.90 on average. On shorter time scales (10 mins), I_{org} values range from 0.6 to 0.96 in specMACS. The highest values frequently appear from artefacts in the cloud mask, when sun glint is not filtered out correctly or when high-level cirrus clouds overlap low-level clouds.

Two 10-minute scenes with low-level clouds in shallow convection, covering the range of I_{org} values from 0.6 to 0.9, are depicted in Figure 5.5. Showing measurements by specMACS together with the corresponding cloud mask, the first scene represents a shallow cumulus cloud scene from RF03. In the first minute of the measurement-period, the disturbing impact of sunglint on the radiation measurements is remarkable. The cloud mask algorithm of Gödde (2018) however performs well and filters out the sun glint. The second example analogously presents a 10-minute cloud scene from RF05. Both examples originate from flights on which the I_{org} averages lie above and below the overall average of the entire NARVAL-II campaign. With a I_{org} value of 0.61, the first cloud field (Figure 5.5a) is classified as less clustered and approaches random characteristics. A high number of cumulus clouds is arbitrarily

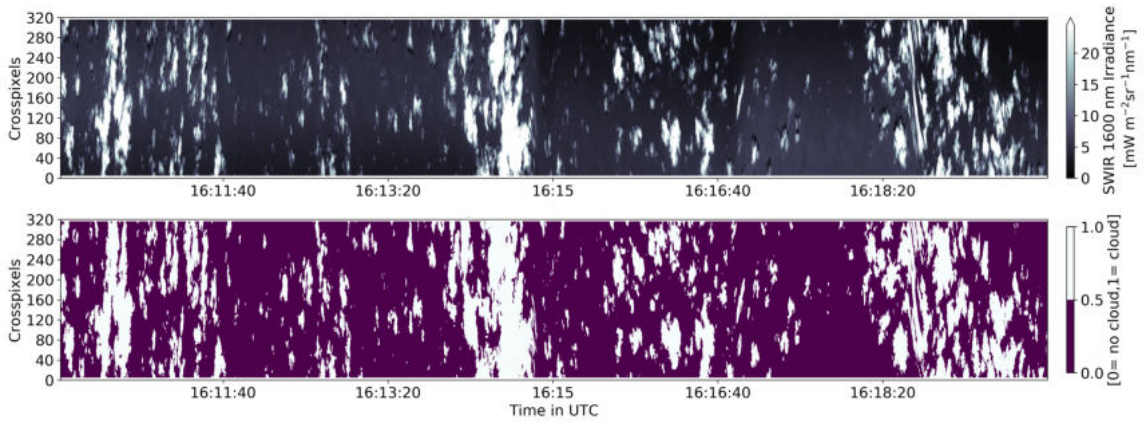

(a) Scene from RF03: I_{org}=0.61

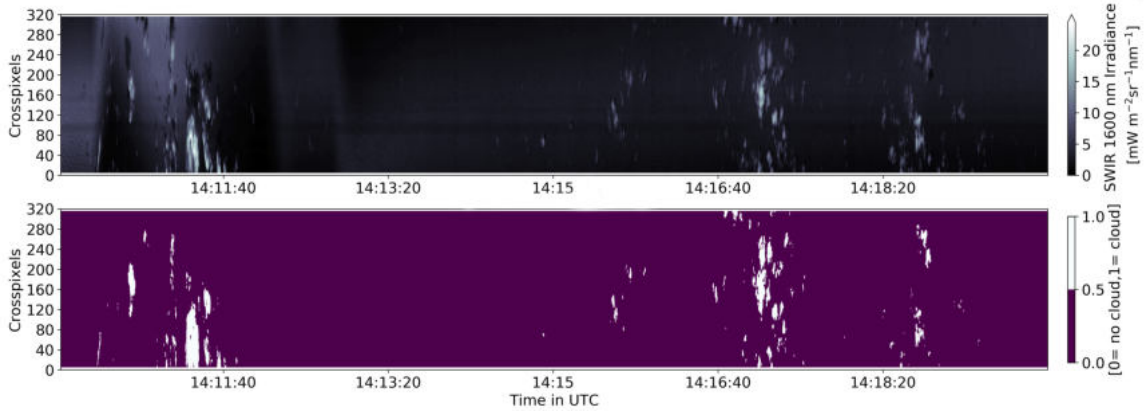

(b) Scene from RF05: I_{org}=0.89

Figure 5.5: Two different cloud scenes a) and b) from specMACS during the time given in UTC on the x-axis. The measurements of the SWIR 1600 nm channel are plotted in correspondance with the cloud mask. RF specifications and I_{org} values are given in the subcaptions.

distributed, e.g. around 16:12 and 16:16. Close to larger cloud structures, aggregation of small cloud fragments can be found especially in the second cloud scene from RF05 (Figure 5.5b). The second scene is characterised by a considerably lower cloud fraction and cloud number. The high I_{org} value results from clear-sky conditions around the larger cloud patterns and from the small cloud fragments surrounding larger clouds.

In the current literature, this aggregation of small clouds around larger shallow clouds attracts more attention with respect to its impact on cloud size statistics (Neggers et al., 2019). The observation of small cloud fragments regarding organisation is a crucial issue, as they are sub-grid scale for the airborne radar as well as for the most satellite devices. Accordingly, the regridded specMACS cloud mask (Section 3.2) investigates the impact of unresolved small clouds on quantifying cloud organisation. Analogue to Figure 5.4, the regridded cloud mask considers the I_{org} in terms of cloud organisation in Figure 5.6.

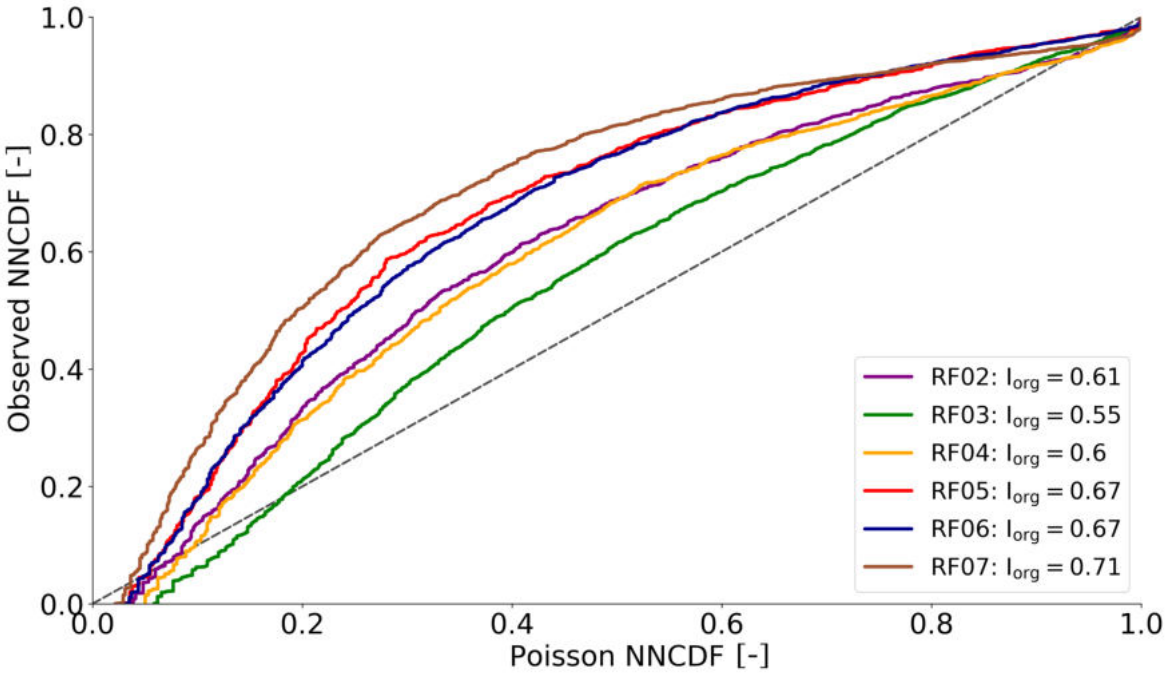

Figure 5.6: NNCDF considering the centroids of clouds related to Poisson NNCDF, analysed for each RF using the regridded specMACS. I_{org} values are listed in the legend for each flight.

According to the I_{org} calculated from the regridded cloud mask for each flight, cloud organisation is decreased for all flights within the coarser cloud mask. The flight-averaged I_{org} here ranges from 0.55 to 0.71. RF03 still shows the lowest clustering on average. RF06, which was also dominated by shallow low-level clouds, certainly remains in the clustered state. Comparing both resolution cases, it is also found that the order of NNCDF curves changes between both resolution. This means that days, which were initially classified as more clustered compared to other days, change in the coarser resolution to less clustering compared to the days under consideration. Due to the narrow FOV, the I_{org} is dependent on the cloud cover as high cloud cover influences the NN distances. However, it was found that the cloud cover in both resolutions shows similar values on minutely scale. Thus, the sub-scale wash-out of small cloud fragments is expected to have the strongest influence on the I_{org} differences between both resolutions, as small clouds preferably accumulate on the larger clouds (Figure 5.5). Interestingly, the intensity of the resolution impact on cloud organisation is variable between the different flights and thus depends on the actual cloud scene.

Analysing the geometrical NN distances also provides new insights in the required time-resolution of airborne devices to distinguish between single clouds. Within the Cartesian coordinate system (Section 3.4), the geometrical distances between NN cloud-pairs are calculated, excluding periods at which CTH $>$ 3000 m. The statistics of the NN distances for each flight are illustrated as a whisker plot in Figure 5.7.

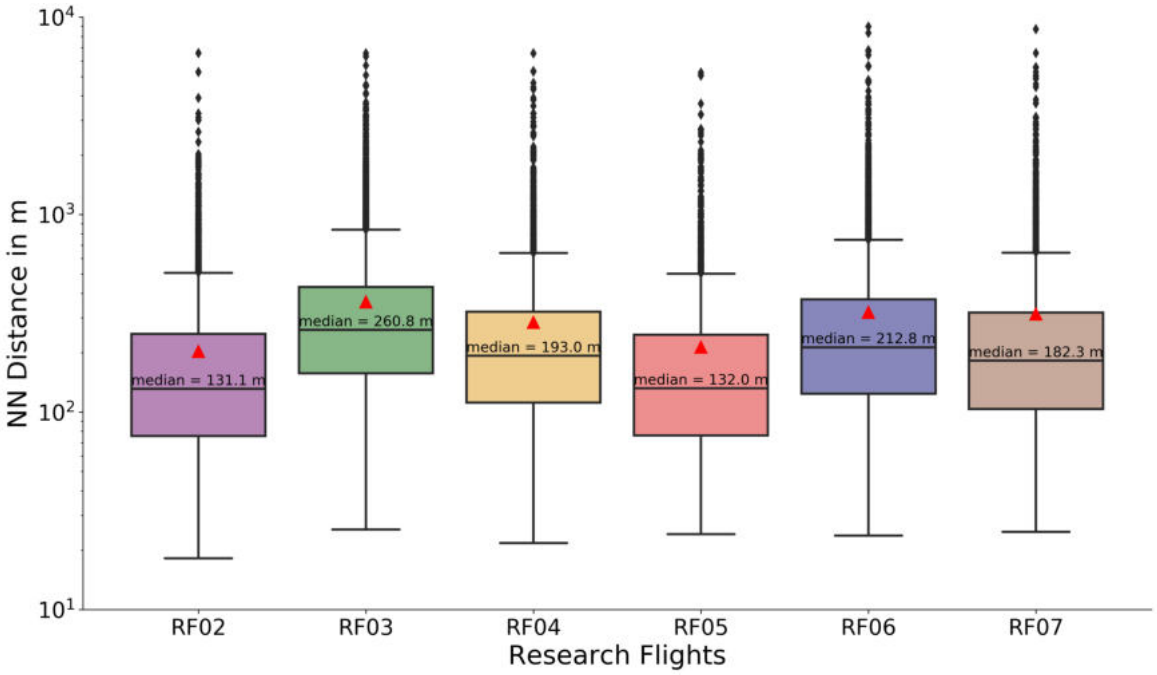

Figure 5.7: Whisker-boxplot showing the statistics of the NN distances for each investigated research flight. The median value is written inside each box. Mean values for each day are indicated as red triangles. Outliers which are outside the whiskers, representing the width of ±1.5 interquantile range (IQR), are depicted as black rhombi.

Besides the main interest in shallow low-level clouds, another reason to focus on periods with CTH < 3000 m is the lower uncertainty of the results. Erroneous CTH estimates in the projection to the Cartesian system can substantially affect the calculated distances between clouds (Section 3.4). For shallow clouds, their CTH variability is reduced which limits the downward projection errors (Section 3.6). In cases, where high-level cloud fragments infiltrate the specMACS FOV and lead to higher CTH in the radar dataset, the distances between lower clouds in the across-track field are erroneously underestimated, so that high-level cloud fragments also distort the results.

For all flights, median values of NN distances are below 300 m. Since the mean is generally more sensitive to outliers, here ranging up to 10 km, than the median, mean values are generally 100 m larger than the median distance values. Between the flights, median NN distances range from around 130 m up to 260 m, whereby RF03 and RF06, which have strongest trade-wind inversion, show the largest NN distances. Shallow convection close to the ITCZ (captured during RF02) reveals the lowest distances between clouds. These shallow clouds occurred in the outflow of dry air which kept the clouds relatively small. In the NN distance approach, the values are not independent from cloud size as the distance between centroids of cloud-pairs is considered.

Nevertheless, it can be concluded that the radar (having a time-resolution of 1 s) erroneously merges a significant part of clouds together for typical ground speeds around 250 m/s. This matter is consistent with the Section 3.3, showing the lower time-resolution to be one major reason for the lower number of clouds detected. Considering the gaps between clouds computed by assuming that all clouds are perfect circles, median gap lengths range from around 40 m to 100 m in shallow convection. While Wood and Field (2011) assume that the gaps between clouds also follows a power law distribution, the specMACS data rather reveals a bell-shaped curve on logarithmic scale with a maximum around 70 m (not shown).

From the RFs, the degree of shallow low-level cloud organisation is examined. Among common satellite-based indexes, the I_{org} is identified as applicable index in the scope of airborne measurements from specMACS, whereas the approach from the SCAI based on Euclidean distances is not suitable. This results from the narrow strip of the specMACS FOV and the uncertainties in geometrical distances due to the CTH estimate in the coordinate transformation. Main findings of the shallow cloud organisation from specMACS are:

- The entire flight-based I_{org} indicate clustered shallow cloud organisation for every RF having values between 0.7 and 0.82.
- Based on 10-minute intervals, the I_{org} reach reasonable low values down to 0.61 in cases of many small shallow clouds in the FOV showing an almost random distribution.
- High I_{org} primarily results from small clouds fragments that are closely orientated around larger patterns. In filtering out small cloud fragments the degree of organization substantially decreases.
- In a coarser cloud mask resolution, I_{org} values decreases but still lie above 0.5.
- Nearest neighbour distances between cloud-pairs mostly are below 300 m.
- Larger FOV are required to derive mesoscale cloud organization from NARVAL-II.

6. Low-Level Clouds in the Wind Field

This chapter deals with the interaction between low-level clouds and the dominant wind field during the NARVAL-II campaign. The focus here is on the influence of the trade winds on geometries of individual clouds, as the FOV from specMACS is too small to detect typical wind-induced phenomena affecting the mesoscale cloud patterns, such as arc-shaped cloud patterns from precipitation and cold pools, further investigated in Zuidema et al. (2017). Investigating the impact of the wind field on cloud geometries is motivated by Mieslinger et al. (2019), as they found the most intense and systematic variation of macrophysical cloud properties aligned with wind speed. Neggers et al. (2003) concluded from LES that increasing wind shear enlarges the projected cloud area. Wind speed is positively correlated with wind shear (Brueck et al., 2015) and aligned with enhanced cloud deepening (Nuijens and Stevens, 2012). It is expected hence that clouds from specMACS show a certain elongation into the wind direction with increasing wind speed. Within this investigation, the wind field is extracted from the dropsondes. This emphasises the capabilities of airborne measurements. The elaborated methods to obtain the wind field in cloud height and to determine the orientation of clouds are described in the following sections. Out of this, the tendency of clouds to elongate or tilt into the predominant wind direction is quantified.

This analysis focusses on shallow low-level clouds with CTHs below 3000 m during RF03 and RF06. This limitation has decisive advantages: The lower and shallower the considered clouds are, the less they are observed from the side at the given VZAs from specMACS which reduces errors in the horizontal projection of clouds. Secondly, when only examining shallow cloud regimes, the sources of error arising from the uncertainty of the estimated CTH are lower, as the CTH variability is generally kept lower (Section 3.6). Thirdly, both RF are characterised by frequent dropsonde releases (50 per flight) and thus provide a good representation of the wind field (Section 2.6).

6.1 Wind Field in Cloud Height

This section describes how the wind field in cloud height is obtained using the dropsonde data. During each dropsonde release, the vertical wind profile is supposed to be well-known with the given device-specific uncertainties (see Section 2.4). Especially in periods of frequent dropsonde releases, as assured during RF03 and RF06, the vertical structure of the troposphere is thus known much more accurately than from reanalysis data. As described in Section 2.4, dropsonde data was transferred to a unified vertical grid having a resolution of 30 m within the CERA database (Konow et al., 2018).

In order to refer the cloud geometries to a continuous series of wind profiles between the releases, the wind field has to be interpolated in time and synchronised to specMACS timestamps. This interpolation is generally crucial as the wind field can be highly variable in space and time. For instance, dropsonde measurements could have been affected by intense fluctuations which are then inferred on the interpolation causing artefacts in the time series. However, since measurements are taken over the ocean, disturbing turbulent features are reduced. The dropsonde wind profiles show consistent tendencies during the flights. In agreement to this, Bony and Stevens (2019) verified the small-scale variability of the wind field being negligibly low for large-scale applications. Nonetheless, the more distant any timestamp is from a dropsonde release, the more uncertain the interpolation is.

During RF03 and RF06, typical trade-wind conditions are found. As further discussed in Section 2.6, a moist layer up to 1.5 km is predominant and wind robustly blows from easterly directions in the lowest 3 km. For the specific heights of each cloud, the overall wind field statistics are illustrated in Figure 6.1. At CBH (Figure 6.1a), the predominant wind direction is from east. Wind speeds are mostly below 10 m/s whereas higher wind speeds up to 12 m/s are recorded from north-east. At CTH (Figure 6.1b), the dominant wind direction turns to a slight north-easterly component. The frequency increase of north-easterly wind directions primarily stems from a slight northern rotation of the wind above the LCL during RF03 (see Figure 2.6). Wind speeds exceeding 12 m/s rarely occured and the dominant winds at cloud height are rather weak. The mean absolute vertical wind shear within a cloud, being the absolute difference between wind speed at CTH and CBH, has a value of 0.77 m/s. The surface wind field, here denoting the mean wind field in the lowest 100 m, consists of easterly winds which barely exceed a wind speed of 8 m/s (Figure A.2).

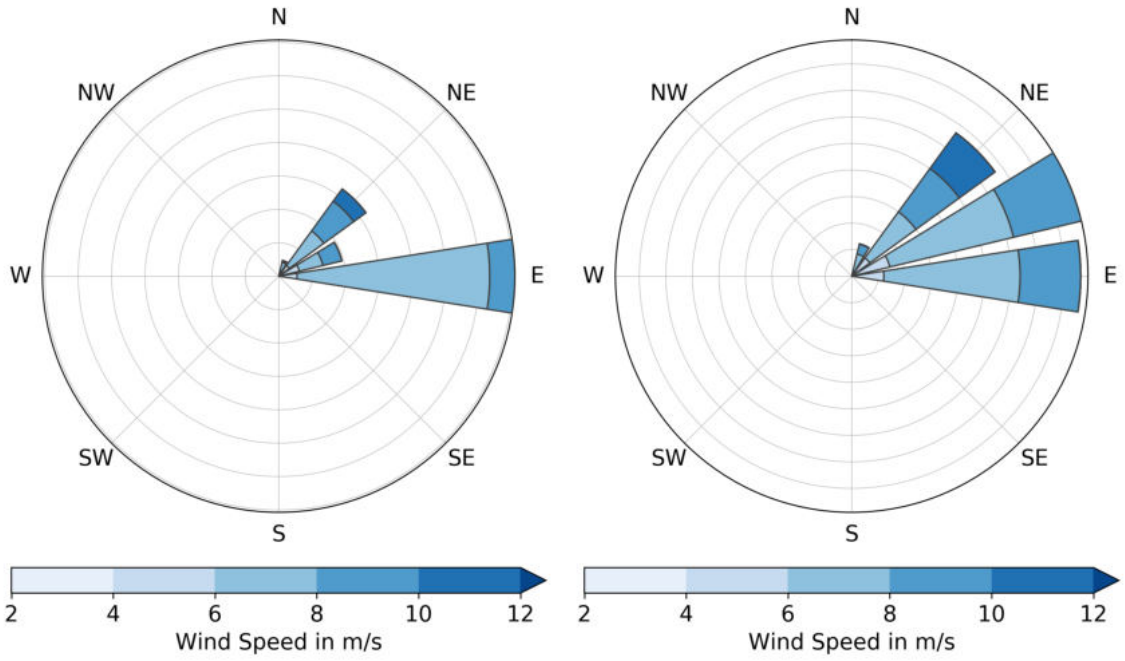

(a) CBH **(b)** CTH

Figure 6.1: Windroses describing the wind field in cloud base height (a) and cloud top height (b) during RF03 and RF06. Wind speed is colour-coded and the frequency of wind direction is normalized by the dominant direction.

6.2 Determination of Orientation of Clouds

To determine the orientation of a shape, it is necessary to quantify its rotation relative to a reference shape with a fixed orientation. Cloud patterns becoming certainly more complex with increasing cloud size (Section 4.3) impede this determination. Therefore, the elliptical fit (Section 3.7) is used, whereof all cloud patterns are interpreted as similar shapes. This facilitates the comparison and classification of several cloud cases. The rotation of the ellipse can be described as the rotation of its semi-major axis a. However, the focus is here on the combined effect of elongation and tilting of clouds due to the wind field. The interest is less in which direction the individual ellipse is oriented, but to what extent in the wind direction.

Figure 6.2 illustrates the application quantifying the cloud orientation. For each cloud in specMACS, the ratio of cloud extension in the wind direction to that of its maximum length is considered and defined as the normalised radius r:

$$r = \frac{R_{\mathrm{WindDir}}}{R_{\mathrm{MajorAxis}}}, \tag{6.1}$$

where R_{WindDir} is the radius of the ellipse in wind direction, and $R_{\mathrm{MajorAxis}}$ is the length of the elliptical semi-major axis. If the cloud is fully tilted into the wind direction, it follows $r = 1$. The lower r, the less the cloud relatively extends in wind direction.

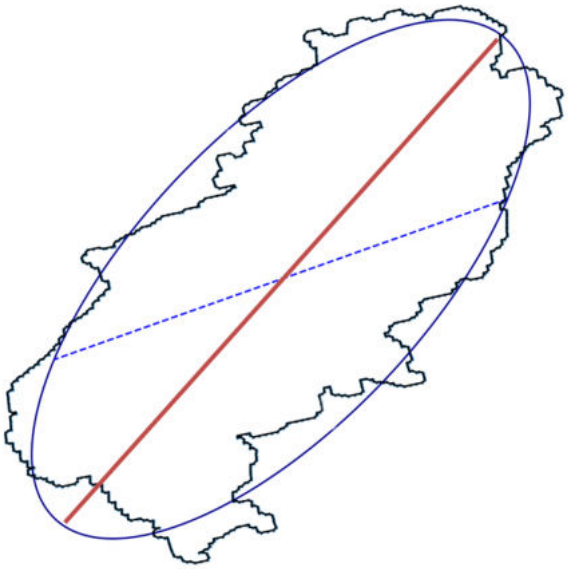

Figure 6.2: Elliptical fit in blue around one cloud from the cloud mask which border is described as a polygon and plotted as black contours. The blue dashed line is the diameter of the ellipse in wind direction. The red bold line is the major axis of the ellipse. The normalised radius is calculated as the ratio between the length of the blue-dashed line and the red line.

However, $r = 0$ cannot always be achieved, as the value of the r is limited by the aspect ratio of clouds (dependency on the aspect ratio in the Appendix). Imaging a circular fitted cloud, r is always 1. If this cloud is elongated with a certain aspect ratio, defined as the length of semi-minor axis b divided by the length of semi-major axis a of the ellipse, the lowest possible value of r is always the aspect ratio.

For the orientation analysis, several clouds have to be excluded due to additional sources of errors that cannot be identified and quantified trivially. In particular, only clouds having an along-track cloud length exceeding 200 m are considered, even though this substantially decreases the sample of clouds. One reason is the high sensitivity of the elliptical fit to small clouds. As already described in Chapter 3, specMACS pixels are not uniformly gridded due to the measurement characteristics. The across-track FOV of each pixel and the along-track frame rate of specMACS lead to different geometric resolutions on the across-track and the along-track axis. For clouds composed of just a few pixels, the fit and thus the orientation of the ellipse is very dependent on the flight direction. Examining the dependency of cloud direction within the flown circles during RF03 and RF06 (not shown here), the influence of the flight heading on the fit decreases considerably for cloud diameters above 100 m and was no longer identifiable above 200 m. Secondly, these small clouds significantly affect the statistics due to their large number (Figure 4.2), whereas their climatologic role is weaker due to their rather small contribution to the total cloud-covered area of 25 % (Figure 4.10).

6.3 Eccentricity of Clouds

Up to this point, 1D cloud sizes were quantified using either the along-track cloud length (Section 4.1) or the area-equivalent diameter D (Section 4.2) which relates each cloud to a circular shape. While along-track detecting devices, such as the radar or WALES, are limited to determining the cloud size along the flight path, specMACS allows the detection of the horizontal cloud size in all directions. The elliptical fit (introduced in Section 3.7) facilitates the determination of cloud sizes in certain directions. In particular, the eccentricity (Equation 3.8) allows to quantify the directional extension of clouds. The stronger the directional extension of clouds is, the bigger the chance is that the along-track cloud length, or D, do not consider the dominant extension of the clouds. Thus, particularly for clouds with high eccentricity, cloud size statistics inferred from the along-track length can significantly deviate from statistics inferred from the length of the major axis of clouds with a high eccentricity. The following paragraphs elaborate the eccentricity statistics of shallow low-level clouds which have an along-track size above 200 m from RF03 and RF06.

For these captured shallow clouds, the mean eccentricity $\overline{e}$ has a value of 0.744. This can be translated to an aspect ratio of roughly 3 : 2. Thus, the clouds show a significant directional extension. The fact that clouds are less circular highlights the benefit of 2D horizontal cloud observations from specMACS for cloud geometry analyses. As mentioned above, clouds having an along-track size below 200 m are excluded from the statistics. In doing so, the relative number of clouds having eccentricities above 0.95 decreases by one half. For clouds smaller than 200 m, the elliptical fitting is based on a poorly resolved cloud structure and the smallest clouds show higher eccentricities due to the irregular specMACS pixel resolution.

The findings of Neggers et al. (2003) and Brueck et al. (2015) lead to the hypothesis that the stretching of clouds, in terms of the eccentricity, is related to the prevailing wind field. In particular, shallow cumulus clouds which are caused by surface-driven evaporation can not rise fully vertically under dominant horizontal winds together with increasing wind shear. Hence, Figure 6.3 investigates the influence of increasing wind speed on the clouds' eccentricity. Therefore, the eccentricity distribution for clouds that underlie low and high wind speeds at CTH (Figure 6.1b) is depicted. The choice of the wind speed thresholds with 5.5 m/s and 10 m/s for both cases represents a statistical compromise. On the one hand, the respective cloud sample sizes remain large enough and are of similar size. On the other hand, both wind field cases remain clearly distinguishable in their intensity.

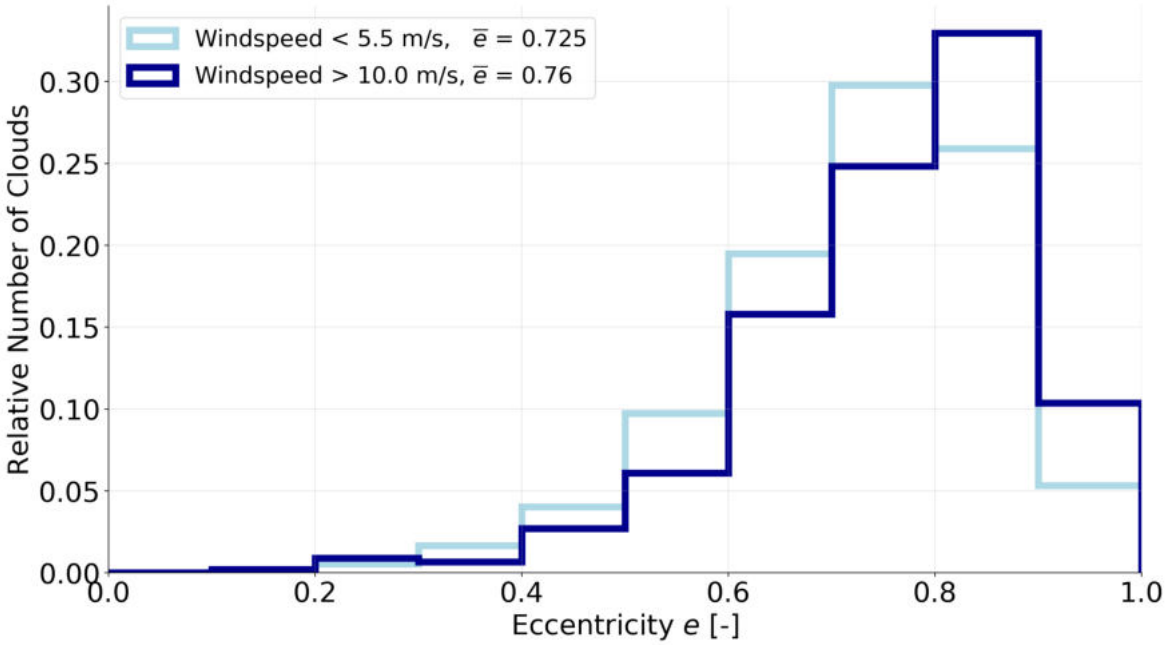

Figure 6.3: Eccentricity distribution of shallow clouds from RF03 and RF06. The barplot shows the relative frequency of eccentricity bins, having a width of 0.1. Shallow low-level clouds (CTH< 3000 m) are considered under low wind speeds below 5.5 m/s and high wind speeds above 10 m/s.

To rule out that both cloud samples stem from an unanimous distribution, the two-sample Kolmogorov–Smirnov test is applied to both samples. The test reveals a p-value of 0.6 % which verifies that both samples are statistically not drawn from the same continuous distribution. Both samples thus represent different cloud conditions.

Comparing the cloud eccentricity distributions for both wind speed cases, it becomes apparent that eccentricity values below 0.4 are found for less than 2 % of the clouds, regardless of the strength of winds. Based on this and according to Equation 3.8, the length of both elliptical axes differ by more than 10 % for 98 % of the clouds. For higher eccentricity values, both distributions reveal different characteristics. At lower wind speeds, more clouds have an eccentricity < 0.8 than at high wind speeds. The maximum relative number of clouds is located around an eccentricity value of 0.75 for low wind speeds and around $e = 0.85$ for high wind speeds. According to the mean eccentricity, increasing from $\overline{e} = 0.725$ at low wind speeds to $\overline{e} = 0.76$ at higher wind speeds, a stretching of clouds can be found for increasing wind speeds.

Thus, the observed low-level shallow clouds from RF03 and RF06 do not have a circular shape but are rather elliptical. This is even more pronounced in the case of higher wind speeds. In particular, it is pointed out that around 45 % of the clouds have an eccentricity higher than 0.8 in the case study of high wind speeds.

If all along-track cloud measurements were based on the semi-minor axis of clouds, the mean maximum underestimation of the dominant cloud length would be 31 % at low and 35 % at high wind speeds according to the mean eccentricity.

6.4 Orientation of Clouds in the Wind Field

From the high eccentricities of clouds, the question arises whether or not the elliptical cloud shape underlies a dominant orientation. Since the cloud stretching increases with stronger winds, it is hypothesised that clouds tend to tilt into the wind direction. For periods during which the flight heading is perpendicular to the wind direction, this would cause cloud length underestimations approaching the worst-case calculations, being larger than 30 %, as given in Section 6.3. Therefore, this section quantifies the intensity of the clouds' orientation into the wind direction, using the normalised radius r (Equation 6.1). Concerning the clouds of the two wind speed cases during RF03 and RF06, discussed in Section 6.3, this approach provides additional information about the wind-based impact on the cloud sizes from different viewing perspectives.

For both wind speed cases considered within the eccentricity analysis, Figure 6.4 illustrates the relative number of clouds for a given r based on binwidths of 0.1. The proportion of clouds with $r < 0.4$ is very small (below 5 %). However, this does not necessarily mean that most of the clouds are orientated in wind direction, as the value of r is always limited by the aspect ratio for mathematical reasons. r values below 0.4 require an aspect ratio of the cloud smaller than 0.4, or in terms of the eccentricity $e > 0.91$. Even if all clouds were tilted perpendicular to the wind direction, $r < 0.4$ could only include 10 % of the clouds according to Figure 6.3. Thus, the eccentricity distribution is partly responsible for the increasing number of clouds with higher values of r in both wind speed cases.

This increase is stronger under high wind speeds. When clouds are exposed to higher wind speeds, there is a higher proportion of clouds having a geometric extension orientated in the wind direction. For more than 40 % of clouds, r exceeds 0.9 at high wind speeds. For low wind speeds this is only given for less than 30 % of the clouds. The average value of r is also higher at high wind speeds than at low wind speeds. Considering the cloud length in wind direction overall causes a mean underestimation of the actual length of the major axis by 21.7 % for low wind speeds and by 17,2 % for high wind speeds, respectively. Hence, the major axis of clouds is likely to be more tilted into the wind direction at higher wind speeds.

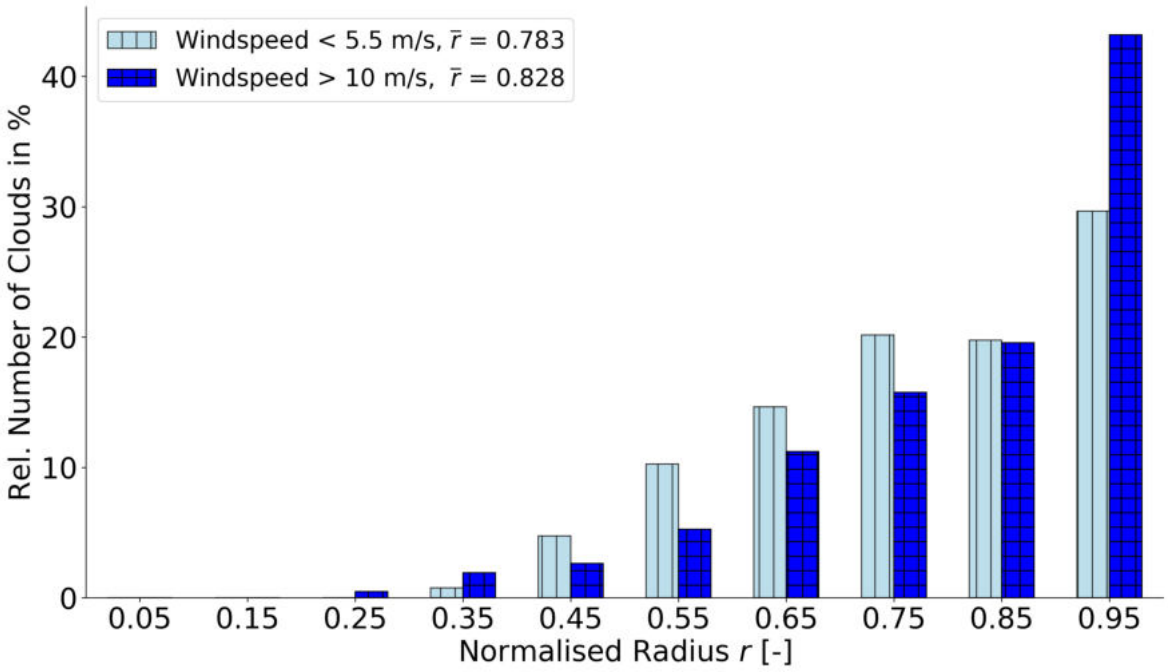

Figure 6.4: Frequency distribution of r of shallow low-level clouds from RF03 and RF06, describing their orientation into the wind direction for low wind speeds below 5.5 m/s (light-blue bars) and high wind speeds above 10 m/s (dark-blue bars) in CTH. Values on the x-axis indicate binmids. Bars are shifted left- and rightwards for visual purposes but refer to same bins having a width of 0.1. Mean values $\overline{r}$ are given in the legend.

Even though these findings support the stretching theory and support the theory that the major cloud axis tilts into the wind direction under stronger winds, the normalised radius r cannot unambiguously characterise the effective extension of clouds in wind direction. Coming back to the issue of the eccentricity dependency of r, high values of r can theoretically result from clouds having a high aspect ratio (being more circular), causing low eccentricity values below 0.5. For mathematical reasons, r cannot decrease below 0.85 in this case. This motivates an eccentricity adapted normalised radius, further on quoted as r^*, defined as the product of e and r for each cloud:

$$r^* = r \cdot e. \tag{6.2}$$

To quantify the effective cloud orientation into wind direction, this product combines the magnitudes of cloud stretching and of the major axis tilting in wind direction, including their counteracting effects; If the axis length in wind direction for one cloud is similar to its major axis length (e.g. $r = 0.9$), but its eccentricity small (e.g. $e = 0.1$), $r^* = 0.09$ will reveal a weak effective orientation in wind direction. If a stretched cloud ($e > 0.9$) is also strongly tilted into the wind direction ($r > 0.9$), r^* will exceed 0.81. The maximum effective orientation is given by $r^* = 1$. Figure 6.5 presents the frequency distribution of r^* for clouds from RF03 and RF06.

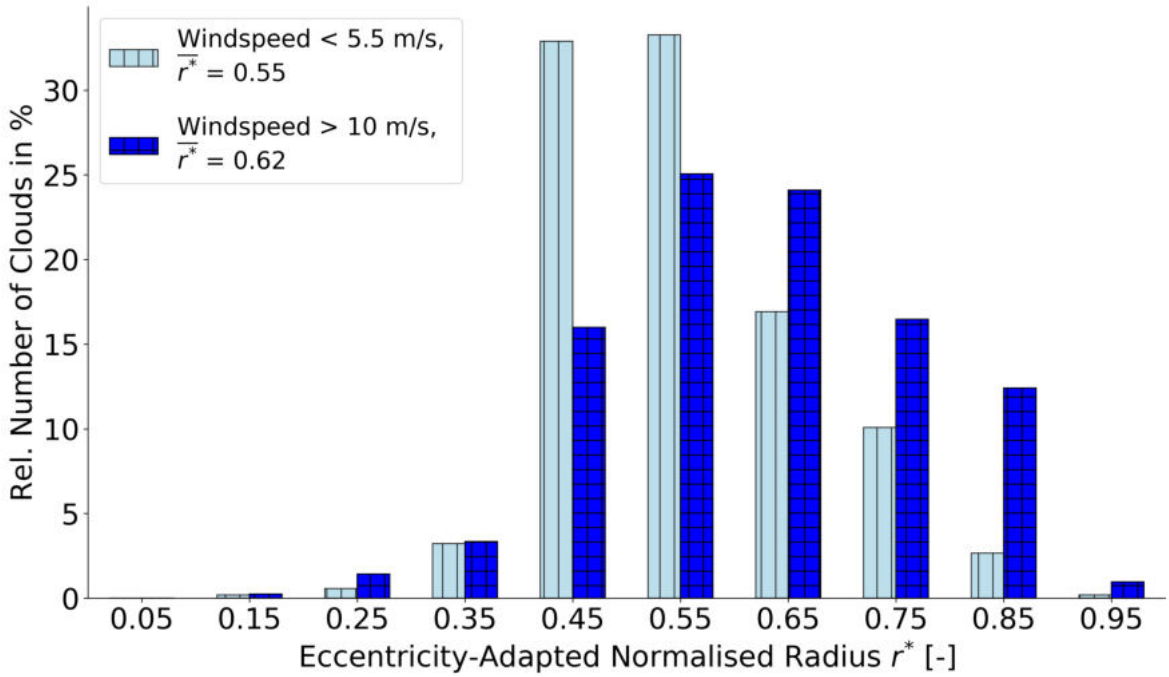

Figure 6.5: Effective orientation of shallow low-level clouds (CTH < 3000 m) from RF03 and RF06 described by the eccentricity-adapted normalised radius r^* for low wind speeds below 5.5 m/s (light-blue bars) and high wind speeds above 10 m/s (dark-blue bars) in CTH. Further specifications are given in the legend in the same way as in Figure 6.4.

For both wind cases, the product leads to skewed distributions of r^* with a local maximum near $r^* = 0.55$. At higher wind speeds, the distribution shifts to the right, manifesting in an increase of the mean value $\overline{r^*}$ from 0.55 to 0.62. The relative number of clouds for $r^* > 0.6$ absolutely increases by more than 10 % to high wind speeds. The increase reveals that clouds are more stretched and their major axis tilts more intensely into the wind direction. This supports the hypothesis that potential sources of error in determining major cloud lengths from along-track observations increase with higher wind speeds, as clouds extend towards the wind direction.

The vertical wind shear, being positively correlated to wind speed, constitutes an important component in that context. While a mean vertical wind shear between CBH and CTH of about 0.7 m/s is found for the low wind speed case, the mean vertical wind shear between both cloud levels has a value of 1.7 m/s at high wind speeds. The radar data consistently shows a deepening of clouds by 30 % at higher wind speeds. As presented in Section 1.2, this deepening supports the bulk equilibrium theory of Nuijens and Stevens (2012) and is similar to observations in Mieslinger et al. (2019). However, these results from NARVAL-II stand partly in contrast to the ASTER framework, created by Mieslinger et al. (2019), showing an increase in CTH of 400 m with increasing surface wind speed from below 2.5 m/s to above 10 m/s. While the cloud deepening

during NARVAL-II primarily results from a lowering of the mean CBH from 1050 m to 940 m, the CTH remains in about 1300 m on average. However, ranges of surface wind speeds are considerably lower for the given cases. Furthermore, this limited response of tropical shallow cloud deepening with higher wind speeds was also found by Bretherton et al. (2013), using LES. Therein, shallow clouds reach a certain depth with increasing wind speed until precipitation becomes more efficient. The aligned dry-out tends to reduce liquid water supply and blocks further lifting of the inversion layer.

6.5 Cloud Size Dependencies on the Wind Field

Based on NARVAL-II, this section further examines to what extent the wind field affects the horizontal cloud size. In a next step, the role of the viewing direction in determining 1D cloud sizes under the influence of the wind field is elaborated.

According to Brueck et al. (2015) and the ASTER-based study from Mieslinger et al. (2019), the horizontal extent of tropical marine low-level clouds depends on the surface wind speed and is coincident with a higher amount of large clouds. In regard to the cloud area-equivalent diameter D, defined in Section 3.7, Figure 11 in Mieslinger et al. (2019) reveals a shift in the cloud size distribution towards larger clouds for higher surface wind speeds together with a scale break increasing from 440 m to 1300 m for wind speeds from below 2.5 m/s to above 10 m/s. Making use of the cloud geometries from the Cartesian coordinate system, the first part of the section investigates whether the cloud size response to increasing surface wind speed can also be identified within the specMACS observations. In order to consider comparable shallow cloud conditions to Mieslinger et al. (2019), the analysis focusses on RF03 and RF06. This, however, strongly reduces the included cloud sample. Furthermore, the surface wind speed variability during both flights is considerably lower (Appendix). To guarantee large enough samples, the regimes of surface wind speed need to be chosen below 5.5 m/s and above 6.5 m/s representing the 25th and 75th percentiles. Only effectively recorded clouds with $D < 4$ km are included in the analysis.

Figure 6.6 represents a replica of Figure 11 in Mieslinger et al. (2019), adapted to the specMACS clouds and to the sectors of surface wind speed given above. It shows the cloud size distributions based on D for both surface wind speed domains to which a double power-law fit is applied. From this approach, larger clouds are detected more frequently with increasing surface wind speed and the scale break shifts from 620 m to 720 m. $\overline{D}$ is about 150 m for low and 175 m for high wind speeds.

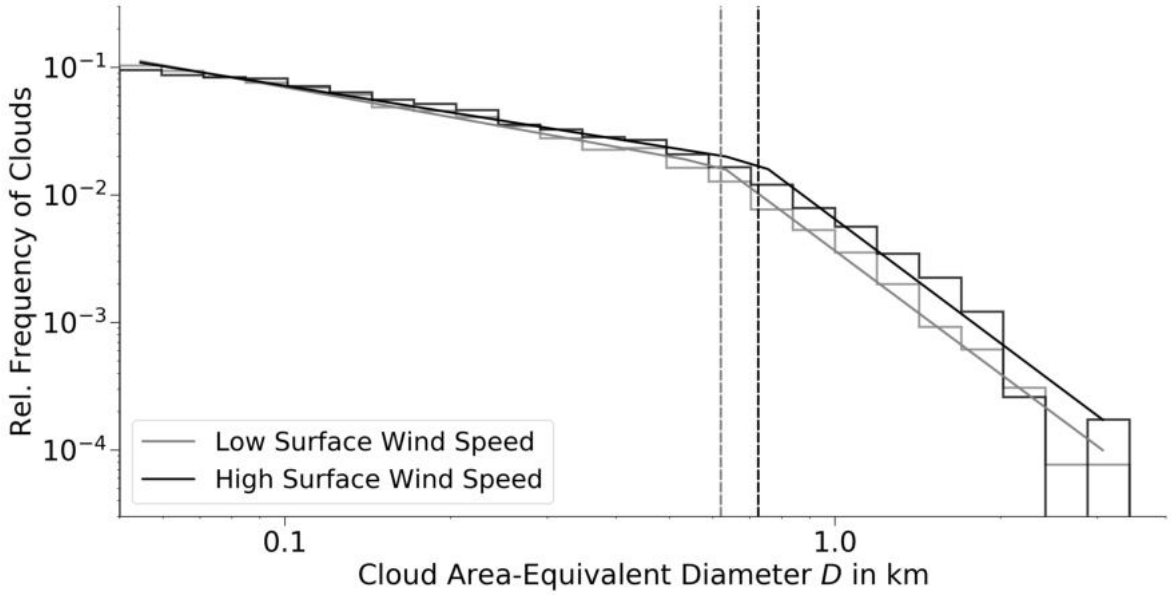

Figure 6.6: Shallow cloud size distributions based on D from RF03 and RF06 for low surface wind speeds $< 5.5\,\mathrm{m/s}$ and high surface wind speeds $> 6.5\,\mathrm{m/s}$.

Although these characteristics are similar to those in Mieslinger et al. (2019) for surface wind speeds between $5.0\,\mathrm{m/s}$ and $7.5\,\mathrm{m/s}$, the wind-induced cloud size increase, identified from Figure 6.6, is uncertain. First, mean values of D differ only slightly between both wind cases. In turn, this can result from the narrow range of wind speeds and does not necessarily counteract the findings. Secondly, the relative errors of the fitted slopes are rather high, up to $10\,\%$. The statistics and slopes are affected by small sample sizes. Taking into account all shallow low level clouds from all RFs during NARVAL-II, the postulated wind impact is more pronounced (not shown) and more large clouds are measured under increasing surface wind speed. However, other flights are characterised by higher CTH uncertainties, potentially causing Cartesian projection errors, as clouds were dominantly observed in variable heights.

The second part of the section relates the previously identified trade-wind induced changes in cloud geometries to the overall 1D cloud size distributions from RF03 and RF06. The impact of the wind field on 1D cloud size statistics can be crucial for different viewing directions. Since clouds tend to become larger (Section 6.5), more stretched (Section 6.3) and more tilted into wind direction (Section 6.4) with increasing wind speed, the question arises to what extent the 1D measurement of cloud sizes from different viewing perspectives affects the overall statistics. Figure 6.7 examines the 1D cloud size distributions in different directions of the cloud axis based on the elliptical fit. Figure 6.7 considers the cloud size along their major axis $2 \cdot R_{\mathrm{MajorAxis}}$, along their axis in wind direction $2 \cdot R_{\mathrm{WindDir}}$ as well as the cloud area-equivalent diameter D. In addition, it includes the along-track cloud length L (Section 4.1.1).

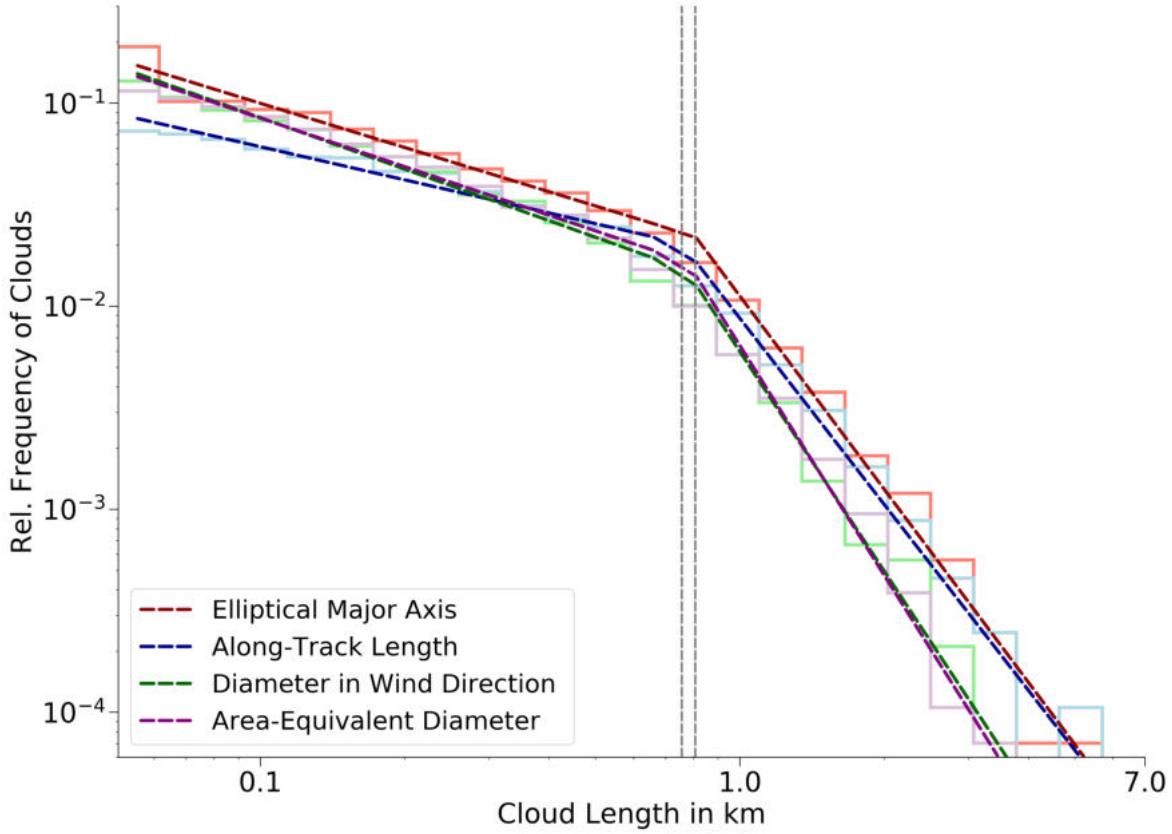

Figure 6.7: Shallow cloud size distribution from RF03 and RF06 for different viewing perspectives with double power-law fits (coloured dashed lines). These are the length along the elliptic major axis (red), the along-track length (blue), the diameter in wind direction (green) and the area-equivalent diameter (violet) including cloud sizes of $2 \cdot R_{\mathrm{MajorAxis}} < 7000\,\mathrm{km}$. Grey dashed-lines show the minimum and maximum scale break.

Regardless of the viewing direction, all cloud size distributions follow a double power law distribution, revealing a scale break around 800 m. Between the viewing perspectives however, different slopes can be identified (Table 6.1). Based on the size distribution, the diameter in wind direction shows similar tendencies as for the area-equivalent cloud size definition. The error from analysing clouds based on their area-equivalent diameter D, as frequently done in literature, is low when the interest is on the diameter of clouds in wind direction. Compared to the shallow-cumulus cloud study of Mieslinger et al. (2019), the slope parameter $\beta_{\log_1}$ has a similar magnitude of size for all perspectives (Mieslinger found a value -0.68). For cloud sizes above the scale break, $\beta_{\log_2}$ is rather high in all perspectives, having values below -3.0 for the specMACS dataset. Mieslinger et al. (2019) calculated a slope parameter $\beta_{\log_2}$ of -2.12. This is mainly caused by the effect that, especially for larger clouds over one kilometre, the probability of clouds being detected as a whole in the FOV of specMACS decreases significantly during the overflight. As a consequence, this analysis could include fewer large clouds than were actually present. The undersampling results in a more negative slope parameter.

Table 6.1: Statistics of Cloud Size Distributions from different perspectives during RF03 and RF06

Size Quantity	Slope Param. $\beta_{\log_1}$	Slope Param. $\beta_{\log_2}$	Scale Break [m]	Mean Value [m]	P25 Value [m]	P75 Value [m]
$2 \cdot R_{\text{MajorAxis}}$	-0.72	-3.16	807.8	205.3	71.3	231.9
$2 \cdot R_{\text{WindDir}}$	-0.84	-3.59	772.0	154.3	53.5	172.1
D	-0.79	-3.76	776.4	159.0	54.5	177.9
L	-0.54	-3.04	756.2	162.3	36.6	180.6

The choice of the viewing perspective is always a trade-off when analysing 1D cloud size characteristics from specMACS. On the one hand, the elliptical approach can be used which is capable to derive the dominant cloud extent for most of the clouds, apart from the largest clouds. On the other hand, the along-track characterisation can be used, covering all overflown clouds but misinterpreting the dominant cloud extension.

The trade winds being the major cloud-controlling factor on tropical shallow low-level cloud properties motivated Chapter 6 to examine the wind-induced impact on clouds, regarding their extension and orientation. While considering the wind field in cloud height, gained from the dropsondes, key findings to be pointed out are:

- RF03 and RF06 show trade-wind typical conditions with dominant easterly winds. In turn, windy conditions with wind speeds above 12 m/s are rare.
- For both flights, the shallow clouds overall have a stretched structure, manifesting in a mean eccentricity value of $\overline{e} = 0.74$.
- Higher wind speeds affect the directional extension of clouds in a way that clouds become less circular. Higher cloud eccentricity values become more frequent.
- The relative cloud extension into the wind field increases to higher values with increasing wind.
- Considering the combined effect of stretching and tilting, single clouds are more orientated into the wind field with stronger winds.
- The orientation of the clouds has to be considered, regarding the measured cloud size. Elongated cloud shapes lead to deviations against the along-track cloud size. Within all the cloud size distributions, the effect of cloud orientation is visible through different slope parameters but less pronounced than expected.

7. Cloud Geometry Robustness

This chapter investigates the robustness of the cloud geometry results from Chapter 6. The determination of geometry quantities in the trade winds, such as R_{WindDir}, requires three measurement devices, namely specMACS (horizontal cloud extent), radar (cloud height) and the dropsondes (vertical wind profile) which lead to various sources of error. For the dropsondes, the measurement uncertainties are already specified in Section 2.4. For the cloud-detecting devices, their uncertainties consist of several factors, such as spectral response regarding specMACS (Ewald et al., 2016) and receiver sensitivity of the radar (Mech et al., 2014). Since their cloud masks underwent several quality checks and post-processing in advance of the thesis, this chapter, however, does not prioritise device-specific measurement uncertainties.

Instead, following JCGM (2008), Chapter 7 focusses on the robustness of the results to uncertainties in cloud top height U_{CTH} and wind direction U_{WindDir} which are identified as main sources of error due to the simplified assumptions carried out in Chapter 3. As described in Section 3.6 and illustrated for the cloud area (Section 4.2), the analysis within the Cartesian coordinate system is reperformed for $\pm$ the expected U_{CTH}, as well as for U_{WindDir}. In the along-track coordinate system, the specMACS cloud mask remains unchanged to only consider the contribution of U_{CTH} and U_{WindDir}.

7.1 Uncertainties due to Cloud Height Errors

The most crucial assumption made in Chapter 3 is the across-track constant CTH. The resulting derivation of U_{CTH} is already delineated in Section 3.6. In order to thereout determine the individual impact of U_{CTH} on cloud geometries, the coordinate transformation for both research flights RF03 and RF06 is reperformed with U_{CTH}, assuming a constant wind-field that is simply the mean wind-field in initial CTH. While Section 3.6 just presents values of U_{CTH} for a short time period, the histogram in Figure 7.1 summarises the distribution of U_{CTH} for the entire RF03 and RF06.

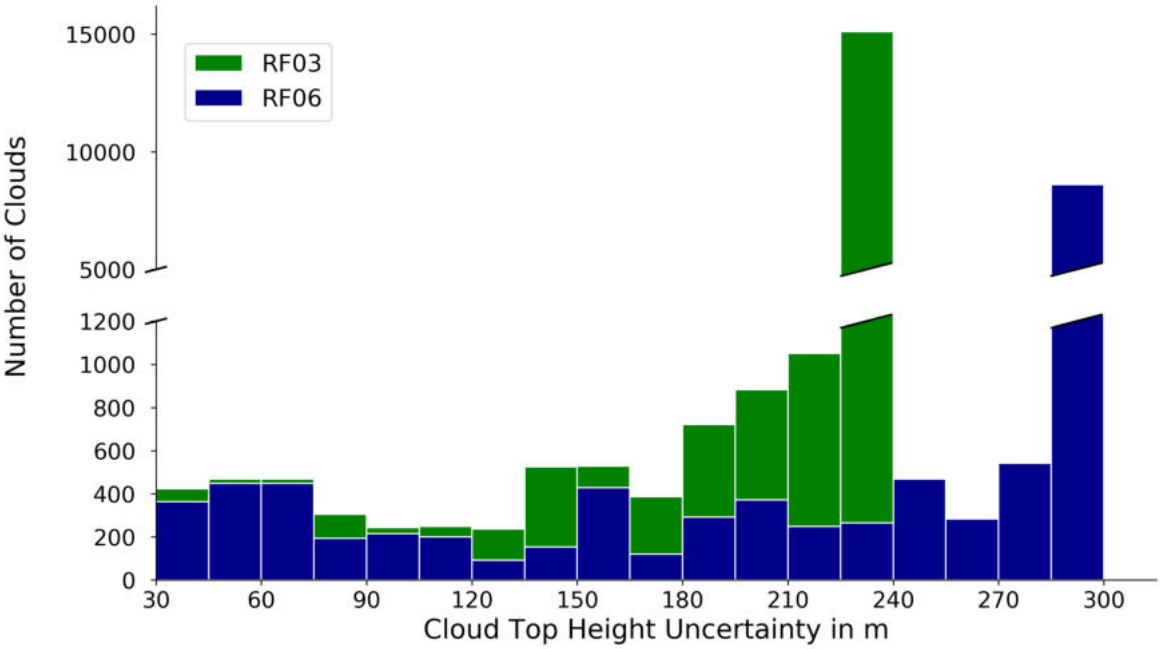

Figure 7.1: Stacked histogram of U_{CTH} showing the distribution of uncertainty values for the entire cloud dataset, gained from RF03 and RF06. The y-axis scale is broken in order to precisely illustrate the distribution for lower uncertainty values and for values above 200 m. Bin witdhs are 15 m.

For CTH uncertainty values below 135 m, most of the clouds are characterised by an uncertainty between 30 and 75 m. Within these bins, the majority of the clouds stem from RF06. These clouds were captured by the radar during the overpass. The bigger these clouds are, the larger their uncertainty is due to their extent in the across-track direction, as the radar just detect a narrow strip of the cloud. The total number of clouds, having an uncertainty from 75 m to 135 m, becomes smaller, whereas the number of clouds from RF03 increases. Higher values of U_{CTH} stem from across-track clouds that are located in the vicinity from radar-detected clouds, being less than 4 km away. For them U_{CTH} increases linearly with distance. The number of clouds having uncertainties between 75 m and 135 m is hence relatively uniform. For $U_{\mathrm{CTH}} > 120$ m, the proportion of clouds from RF03 starts dominating.

Mainly the number of clouds, having $U_{\mathrm{CTH}} > 180$ m, strongly increases for RF03. Almost 15,000 clouds are in the 232.5 m bin, constituting more than 75 % of all clouds captured during RF03. They represent the clouds being not detected by the radar and even not located in the vicinity of radar-detected clouds. For these clouds, their uncertainty is defined as the radar-based 30-minutes mean variability of CTH, having a value of 229 m during RF03. For RF06, the variability of CTH is higher, so that higher U_{CTH} occur compared to RF03. Similar to RF03, most of the clouds (almost 10,000) are too distant from radar-detected clouds and have a high uncertainty of 298 m.

In the scope of this uncertainty assessment, the coordinate transformation and its precedent analysis are performed for the initial CTH estimate $\pm U_{\mathrm{CTH}}$. For the relevant cloud geometries, which are examined in Chapter 4 and 6, the relative error to the initial value is calculated for each id-labelled cloud. From that, the 95 % confidence interval of the relative error is calculated. This represents a quite conservative approach, as the confidence interval considers a broad range of variability. Furthermore, this approach neglects that values might cancel out in the overall statistics, as the errors in CTH change from cloud to cloud. Nevertheless, since the ranges of variability are chosen carefully, the calculated uncertainties serve as an useful assessment of the robustness of the cloud geometry results. The uncertainty results are illustrated in Figure 7.2 with regard to the relative error in cloud area A and R_{WindDir} for both flights separately. Since the eccentricity e and the normalised radius r constitute relative quantities, their absolute errors due to U_{CTH} are depicted.

During both flights, the magnitude of the uncertainties in cloud geometries is different (Figure 7.2). The relative errors generally show a larger dispersion during RF06. This is mainly caused by higher U_{CTH} during RF06 due to a stronger variability in time compared to RF03 (Figure 7.1). Concerning the cloud area, higher U_{CTH} increases the differences in the distance d between HALO and the cloud and lead to larger changes in cloud size within the Cartesian projection (Equation 3.4).

In particular, the uncertainty values are dependent on the cloud size. For larger clouds, the projection error, affected by the shifts in CTH, has less impact on the uncertainties of all quantities than it is the case for small clouds consisting of several pixels. The shape of small clouds is significantly affected by the ratio of the specMACS pixel distance in across- and along-track. Slight changes in CTH affect the across-track distance between the pixels, while the distances in the along-track remain unchanged. The larger the cloud, the less the cloud shape is sensitive to U_{CTH}. This is mainly pronounced in the eccentricity error and the aspect ratio. While the eccentricity of the smallest clouds can change by up to 0.4, the change is marginal for large clouds. This cloud size dependency affects the calculation of the 95 % confidence interval. Due to the cloud size dependency, the 95 % confidence levels are fitted by rational functions. According to the confidence fits for both flights, the relative error of cloud area decreases below 0.1 for cloud areas above $10^4\,\mathrm{m}^2$. The absolute uncertainty in eccentricity as well as the relative error of R_{WindDir} decline below 10 % for clouds having a major axis length above 200 m. These decreasing uncertainties justify the exclusion of clouds with $D < 200\,\mathrm{m}$ in the analysis of Chapter 6.

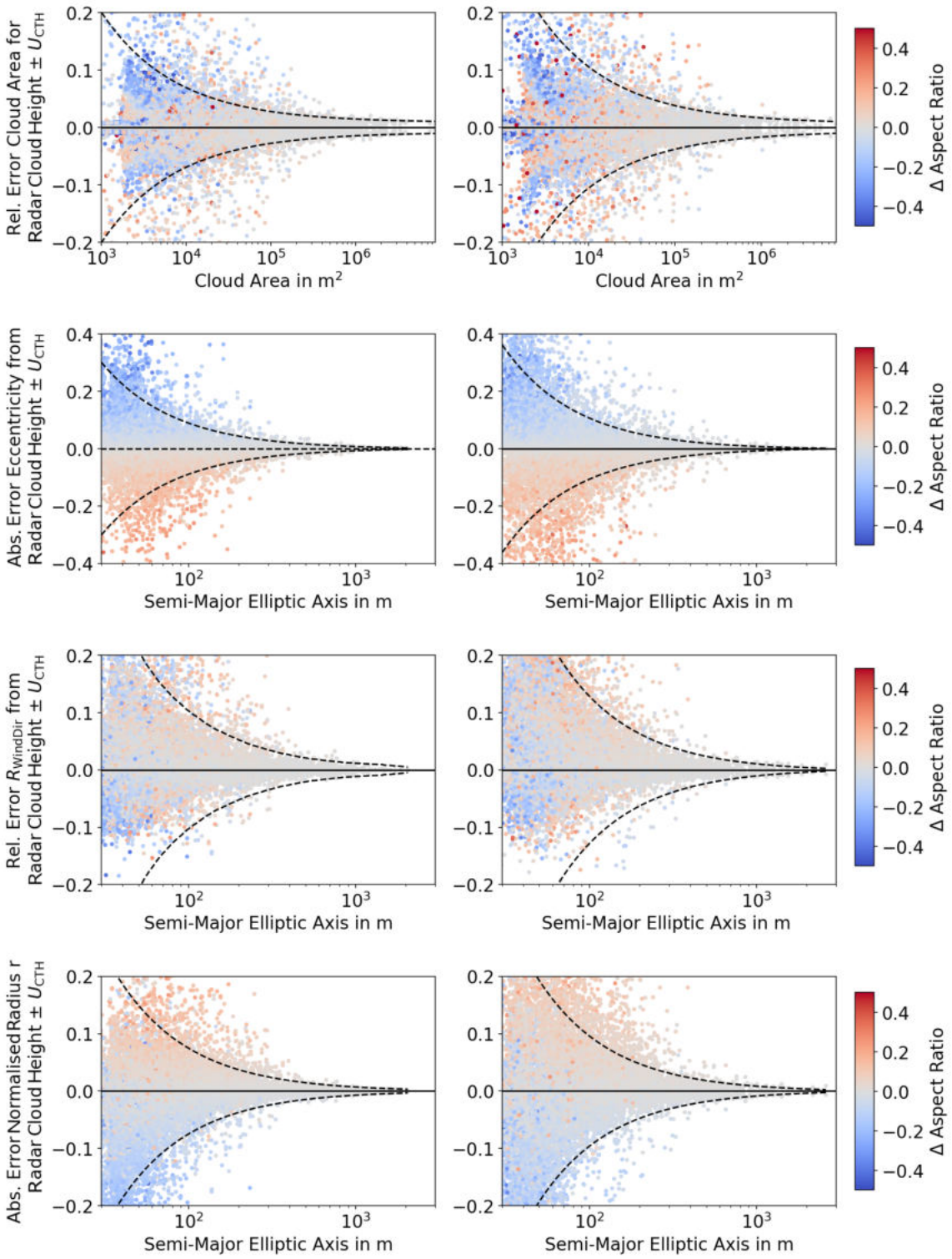

Figure 7.2: Robustness of cloud geometries to estimated uncertainty of CTH from RF03 (left column) and RF06 (right column) showing the relative error of geometry quantities as a function of cloud size specified on the x-axis. Considered cloud quantities are: cloud area A, eccentricity e, radius in wind direction R_{WindDir} and the normalised radius r. Dots represent the relative error for each cloud and are colour-coded with the relative error of the cloud axis aspect ratio. The black dashed lines represent the 95 % confidence intervals of the relative error, fitted as rational functions.

Based on the confidence intervals, the normalised radius r robustly deviates with less than 0.1 for clouds having a major axis length larger than 200 m. As already discussed in Section 6.2, r strongly depends on the eccentricity. While the 95 % confidence interval exceeds 0.2 for the smallest clouds, the errors in r can grow above 0.4 for those of the small clouds having an eccentricity above 0.9.

This uncertainty assessment neglects the systematic error of too low projected clouds resulting from the low sensitivity of the radar. Further analysis of this CTH underestimation requires supplementary CTH information such as given by the LiDAR measurements from WALES. WALES detected a higher cloud fraction in shallow convection (Pavicic, 2018) and can improve the CTH estimate in time.

7.2 Uncertainties due to Wind Error

RF03 and RF06 represent the flights with the most frequent dropsonde releases and thus the highest accuracy of wind field data at cloud height. Nonetheless, wind direction constitutes a strongly fluctuating quantity so that its impact on the relevant cloud geometry results is depicted in this section.

To investigate the influence of erroneous wind direction data, an estimate on its uncertainty is required. This uncertainty does not only result from the dropsonde accuracy of $\pm 1°$, but also from the interpolation in time. Therefore, the standard deviation of the wind direction in CTH is calculated and considered as a proxy of uncertainty. This can be applied to the dataset as the wind profiles exhibit no shifts in wind direction over the critical values (0, 180, or 360°) up to the trade-wind BL, so that no decomposition of the wind direction into the u- and v-component is required.

Similar to Figure 7.2, Figure 7.3 demonstrates the error of the cloud geometries with regard to the wind direction uncertainty U_{WindDir} for the relevant quantities, namely the R_{WindDir} and the normalised radius r. Since the variability of wind direction during RF06 is higher with $U_{\mathrm{WindDir}} = 5.78°$ against $U_{\mathrm{WindDir}} = 3.82°$ during RF03, the geometries show larger deviations for RF06. Due to the elliptical geometry, the cloud size has no mathematical relation to the magnitude of geometry uncertainties for changes in wind direction. Instead, the magnitude of the error at a single cloud strongly depends on its eccentricity. With increasing eccentricity, the higher aspect ratio of the cloud leads to a greater sensitivity to the angle at which the directed cloud length is measured. Nonetheless, in most of the cases, the errors lie below 0.1 for U_{WindDir}.

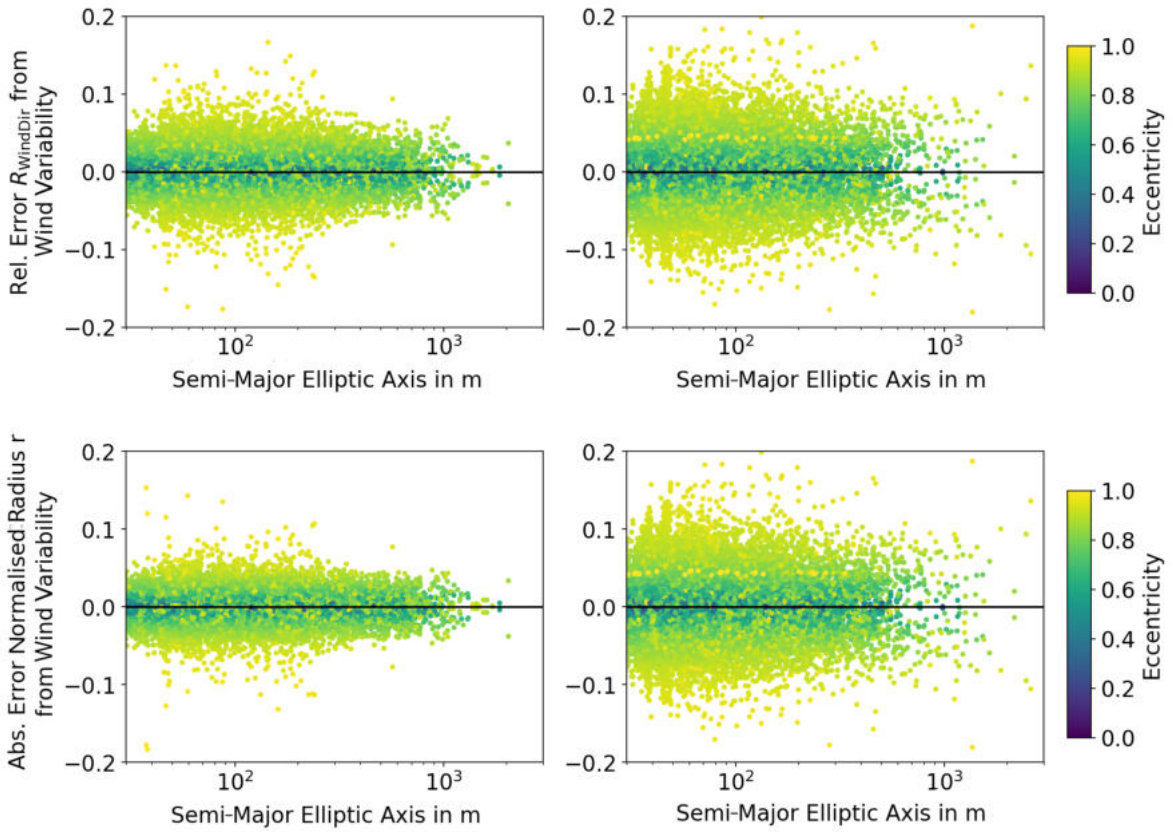

Figure 7.3: Uncertainties of cloud geometries R_{WindDir} and r from assumed $U_{WindDir}$ for RF03 and RF06 showing their relative and absolute error, respectively. Each dot represents the error for one ID-labelled cloud. Error values are depicted as a function of cloud size, as specified on the x-axis, and of the eccentricity for each cloud as specified by the colourbar.

7.3 Robustness of Cloud Orientation

After identifying the major sources of error within the methods applied to investigate shallow cumuli in the trade winds, the cloud orientation examination is recapitulated with regard to U_{CTH}. The main purpose is to verify if the presented cloud-wind coupling (Sections 6.3 and 6.4) still persists under consideration of the uncertainties.

As found in Section 6.3 clouds tend to have a higher eccentricity under increasing wind speed and becomes more stretched and less circular. Since the eccentricity is only affected by the cloud structure, which itself is sensitive to the CTH estimate, the postulate of increasing eccentricity from Figure 6.3 is again examined for the CTH uncertainties. Similar to Figure 6.3, the frequency distribution of eccentricity values is illustrated for low wind speeds (below 5.5 m/s) and high wind speeds (above 10 m/s) in Figure 7.4 and now includes the calculations from the projection errors due to the uncertainty of CTH.

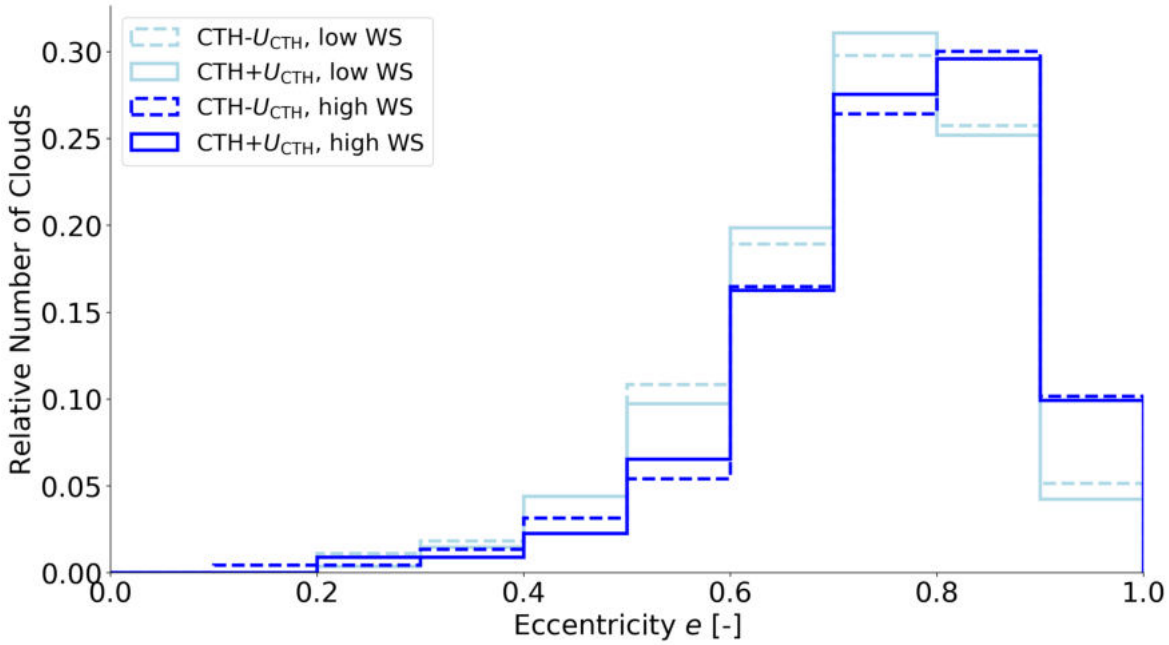

Figure 7.4: Histogram of the eccentricty values for shallow clouds (CTH $< 3000\,\mathrm{m}$) from RF03 and RF06, considering the sensitivity of the eccentricity distribution to uncertainties in CTH, U_{CTH}. Equivalent to Figure 6.3, clouds are considered at low wind speeds below $5.5\,\mathrm{m/s}$ and at high wind speeds above $10\,\mathrm{m/s}$.

The two wind speed cases are still clearly distinguishable regardless of the U_{CTH} and higher values of e appear more frequent at higher wind speeds. In particular, the number of clouds within the largest eccentricity bin remains twice as high at high wind speeds. In conclusion, the cloud stretching is robust under consideration of the uncertainties due to erroneous projections within the coordinate transformation.

Regarding the effective orientation of clouds into the wind direction, quantified by r^* in Section 6.4, both sources of error wind direction and CTH become relevant. Sections 7.1 and 7.2 conclude that especially the smallest clouds with high eccentricity values are affected the most by U_{CTH} and U_{WindDir}. In the real case, the wind direction is also variable with height, which is neglected in Section 7.1, where the wind field is kept constant. Thus, U_{CTH} also leads to deviations of the wind direction. The errorbars in Figure 7.5 here describe the robustness of the effective cloud orientation into the wind field r^* (from Figure 6.5) to the combined impact occuring from U_{CTH} in the vertically variable wind profil. Since clouds smaller than $200\,\mathrm{m}$ are excluded, the uncertainties lead to small deviations in the distributions. As shown, the distributions still shift to higher values of r^* with increasing wind speed. Taking into account the uncertainties, it can hence be concluded that clouds tilt into wind field the higher the wind speed, which is aligned with increasing wind shear. Larger cloud samples are in turn desirable to obtain more universal results.

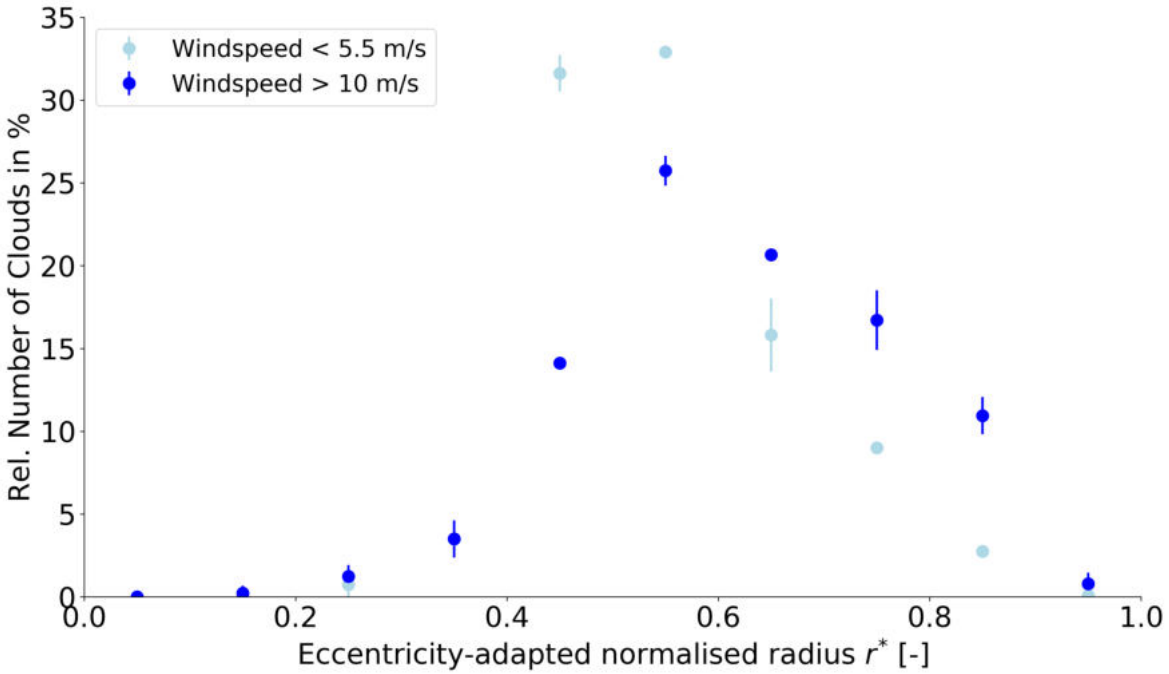

Figure 7.5: Robustness of shallow cloud orientation tendency into the wind-field. Errorbars show the deviations in the distribution for the given CTH uncertainties at bins of eccentricity-adapted normalised radius r^*. Low-level clouds (having a CTH below 3000 m) are considered from wind speeds below 5.5 m/s and above 10 m/s.

7.4 Recommended Improvements

This section sketches the capabilities of a supplementary method to estimate the across-track cloud height with the aid of an exemplary cloud scene consisting of two precipitating shallow cumulus clouds, depicted in Figure 7.6. For this scenery the assumption of across-track constant CTH is inaccurate as the smaller clouds are expected to have lower CTHs than the precipitating clouds which themselves are uneven in the across-track direction. In order to improve the CTH approximation, future research could apply the method of Barker et al. (2011). Their 3D cloud construction algorithm distributes active measurement products from the nadir pixels (denoted as donor pixels) to the across-track pixels (recipient pixels) in the swath of the imager. Recently applied to satellite measurements (Ham et al., 2014), this algorithm is equivalently suitable for the measurements taken from HALO.

Concerning specMACS, the sum of all spectral radiances in 256 channels for the SWIR camera is computed for each pixel. Since the radiances are sensitive to the daily cycle of the atmospheric conditions and the solar illumination, only pixels within a certain distance and solar position range can be considered as potential donor pixels.

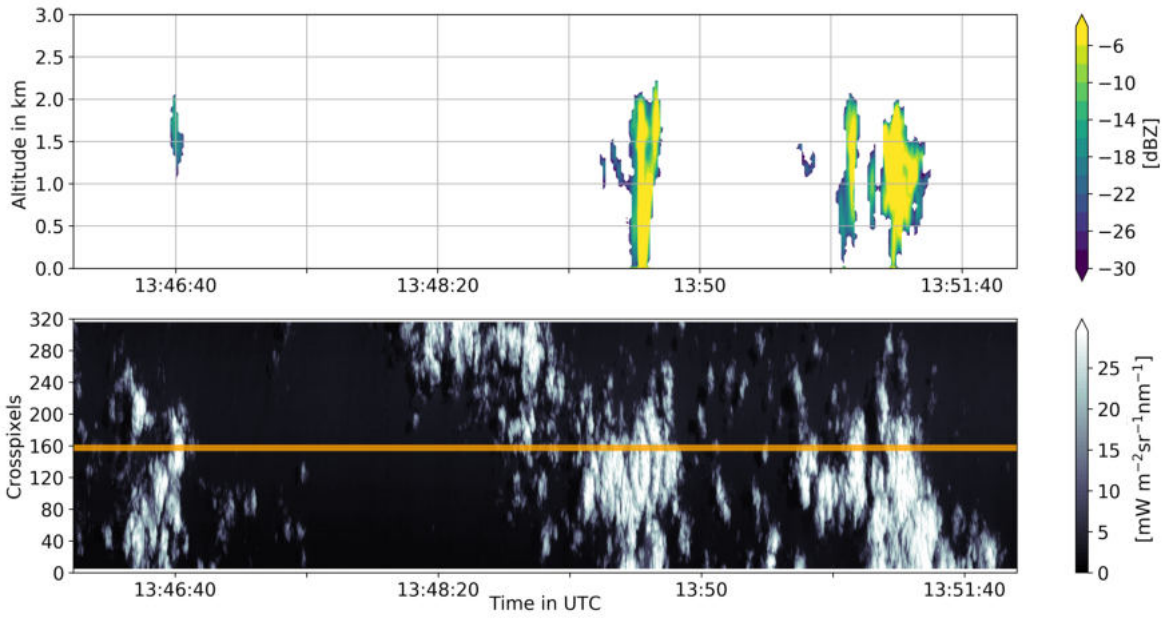

Figure 7.6: Cloud scene during RF05 from 13:46 to 13:52 UTC, measured by the radar reflectivity (upper panel) and specMACS (lower panel) depicting the SWIR 1600 nm radiances. Orange line indicates the radar FOV.

Following (Barker et al., 2011), the actual donor pixel in the across-track axis is identified via a cost-function. Spatial domains restricted to given thresholds in the distance between donor and recipient pixel and solar position change are considered. For each across-track pixel (recipient pixel), the pixel within the FOV of the radar providing the minimum difference in summed radiance and the minimum distance to the recipient pixel is identified and labelled as the donor pixel. The radar profiles of cloud properties at the timestamp of the donor pixel are then replicated to the recipient pixel. Linking the passive radiance measurements with the active radar measurements, the CTH becomes variable in the across-track direction.

As a trial, the algorithm is applied to the regridded specMACS cloud mask and then upsampled to the actual specMACS resolution. The obtained across-track CTH for the cloud scene of Figure 7.6 is shown in Figure 7.7. At first glance, across-track CTHs show plausible values. However, several artefacts can be found which supposedly result from the averaging over valuable measurements due to the regridding of the specMACS values. Nevertheless, for the simplifications presented in this section, the algorithm already significantly enhances vertical representation of cloud structure in the across-track field. In the standard resolution, the implementation of this algorithm data in turn requires high computational costs, as specMACS provides $256 \cdot 320 \cdot 30$ measurements per second. Moreover, including all channels in the approach of Barker et al. (2011) can cause issues, as channels have different levels of sensitivity to clouds, as demonstrated in the SWIR spectra in Figure 2.3.

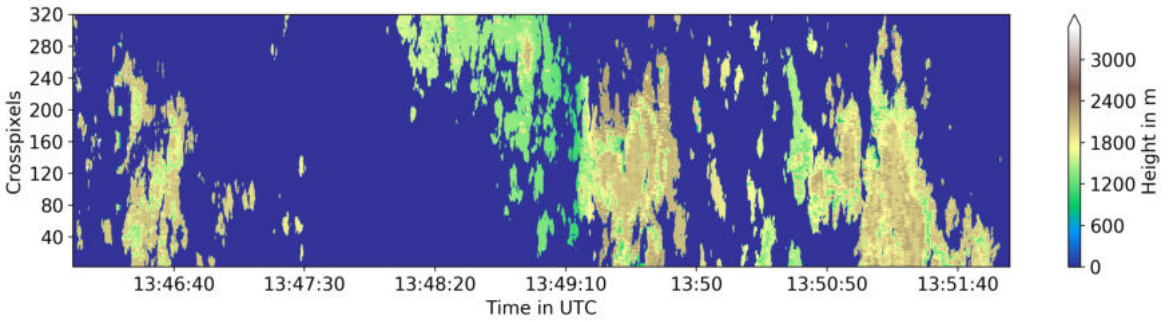

Figure 7.7: Across-track CTH (colour-coded) obtained by a simplified approach of Barker et al. (2011) for the cloud scene seen from specMACS, given in Figure 7.6.

For further interest on the capabilities of the Barker algorithm, this thesis addresses the reader to the upcoming doctoral thesis of Lucas Höppler in which he makes use of an improved version of the Barker algorithm. Synergizing specMACS, WALES and radar measurements, he derives microphysical cloud properties for the quantification of diabatic cloud heating and cooling.

Since the radar product partly lacks of cloud information in the nadir perspective, subsequently including the LiDAR measurements from HALO into the cloud geometry analysis is recommended. During NARVAL-II, the radar particularly did not capture a relevant number of overpassed shallow clouds, which were in turn measured by WALES. Such an example of missed clouds from RF05 is presented in Figure 7.8. As already mentioned, RF05 is characterised by strong winds (Section 2.6). In addition, strong wind shear above the CBH occurred according to the dropsonde profiles. The illustrated cloud scene nicely shows cloud streets aligned in wind direction, which is relatively parallel to the flight heading here. The radar, however, has difficulties to capture the clouds and only resolves one cloud edge which is far from a realistic representation of the CTH. Small cloud fragments within the FOV are not captured.

The frequency of dropsonde releases was relatively low for this flight. As a result, the wind-profile is considerably known less accurate than for the other RFs. This highlights the importance of many dropsonde releases to characterise cloud-wind coupling. For this flight, model simulation data could at least achieve an improved representation of the wind field regarding vertical wind shear. Making subsequent use of the LiDAR data, the analysis based on the Barker algorithm of such atmospheric conditions might provide more details about the behaviour of clouds in wind shear from their base height to their top.

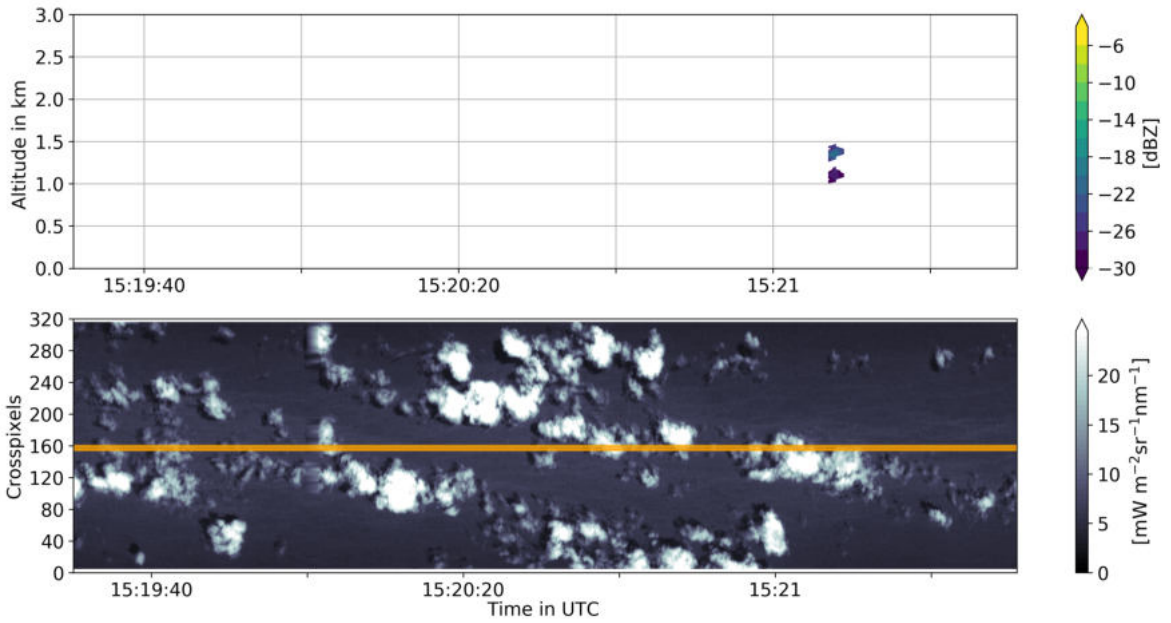

Figure 7.8: Cloud street scene during RF05 from 15:19:30 to 15:21:30 UTC measured by the radar in dBZ (upper panel) and specMACS (lower panel depicting the radiance of the 1600 nm channel).

Chapter 7 assessed the robustness of the cloud geometries, presented in Chapter 6 from RF03 and RF06, against the uncertainties in CTH U_{CTH} and wind direction U_{WindDir}. Within the framework of the coordinate transformation (Section 3.4), U_{CTH} and U_{WindDir} have the following major impacts on the considered cloud geometries:

- Higher uncertainties of U_{CTH} and U_{WindDir} occur during RF06 and overall cause higher uncertainties in cloud geometries for RF06.
- Small clouds consisting of just a few pixels and in particular those that have a high eccentricity are the most sensitive to U_{CTH} and U_{WindDir}.
- The magnitude of the cloud geometry errors due to U_{CTH} considerably decreases with cloud size. For clouds with $D > 200\,\mathrm{m}$, the deviations of the geometry results are significantly below 10 %.
- In terms of the uncertainties considered, the major findings of Chapter 6 – the tendency of cloud extension and orientation into the wind direction with increasing wind speed – remain robust.
- Further across-track representation of cloud height, such as provided by Barker et al. (2011) can subsequently enable more insights into vertical cloud and wind field coupling.

8. Conclusions and Outlook

This thesis analyses airborne-based observations of marine shallow low-level clouds within the trade-wind region using data captured during NARVAL-II on board of the research aircraft HALO. This chapter recapitulates the methods applied, summarizes the results of the macrophysical cloud properties and states conclusions drawn from the results. Ideas for improvements regarding upcoming campaigns are outlined.

8.1 Summary and Conclusion

NARVAL-II was the first flight campaign over the Tropical Atlantic which was equipped with the hyperspectral 2D-imager specMACS – a useful component in addition to along-track profiling devices like the radar. Gödde (2018) established a cloud mask for specMACS and provided a framework for further cloud analysis within the tropical region. As an extension, this thesis reveals the wide-ranging capabilities of such airborne cloud products by analysing the cloud geometries and their spatial arrangement. From LES and BCO measurements, Nuijens and Stevens (2012) and Brueck et al. (2015) designated trade winds as the dominant driver on shallow low-level clouds. Satellite-based findings of Mieslinger et al. (2019) showed the interacting role of the trades and motivated the investigation of the cloud-wind coupling based on the clouds from specMACS. Research questions set to be answered within this thesis were:

- What are the new capabilities of 2D airborne-based cloud observations by specMACS compared to the radar observations regarding cloud geometries?
- Are the macrophysical properties of tropical shallow low-level clouds consistent with previous satellite-based statistics?
- Can simple shapes well represent complex cloud structures?
- Can shallow cloud organisation phenomena be identified from specMACS measurements? Does the spatial arrangement of the clouds reveal certain patterns?
- To what extent do the trade winds represent a controlling factor on the cloud geometries?

In order to pursue these scientific questions, a number of technical aspects need to be considered. In particular, the merging of the horizontal cloud mask from the hyperspectral imager specMACS with the along-track and vertical cloud information from the cloud and precipitation radar is fundamental for the acquisition of horizontal cloud geometries. However, this requires further processing of the cloud masks:

While 1D along-track cloud geometries are inferred from the time axis with consideration of the flight speed, the specMACS across-track axis is initially provided in camera pixels. Since these pixel sizes are dependent on the flight attitude, clouds are individually transferred into a geometric distance-based Cartesian coordinate system. The coordinate transformation considers the direction vectors of each across-track pixel from specMACS and takes into account the flight attitude. This is based on the yaw, pitch and roll angles which are obtained from the BAHAMAS dataset. Clouds are hence projected into Cartesian coordinates by tracking down the vectors to the cloud top height (CTH) which is gained from the radar cloud mask. Due to different fields of view (FOV) of the radar and specMACS, this requires a time-dependent time shift of the radar observations so that the same clouds are related to equivalent time steps in both devices. Since the radar is only capable to detect clouds underneath the aircraft, its derived CTH is approximated to be constant in the across-track direction. CTH values being below the lifting condensation level (LCL) from the nearest released dropsonde are filtered out. Such false CTH retrievals can arise from fall streaks ranging into the FOV of the radar. Finally, the CTH time gaps are closed through interpolation. From this reference system, Chapter 4 analyses individual clouds for their geometrical properties such as their along-track length, cloud area and cloud shape complexity.

As presented in Chapter 5, the across-track FOV of specMACS enables an investigation of horizontal shallow cloud arrangement, even if the FOV is restricted to less than 10 km. The applicability of common indexes to quantify the degree of organisation, however, is crucial for airborne measurements from specMACS. Thereby, the Organization Index I_{org} is identified to be best suited for this analysis when no strong flight manoeuvres are performed. According to the definition of the I_{org}, cloud organisation is classified as clustered if the integral of the observed cumulative density function of nearest neighbour distances between cloud-pairs, plotted against that of a random Poisson point process, exceeds a value of 0.5. The relevance of the cloud mask resolution on the I_{org} values is examined in order to specify the degree of organisation for different cloud size regimes.

For the investigation of the interactions of shallow low-level clouds and the wind field, RF03 and RF06 are best suited. First, flight tracks are located far from deep convective regions providing conditions similar to the more intense winter trades. Secondly, highly frequent releases of dropsondes supply a high-resolution representation of the prevailing vertical wind field in space and time. The wind profiles are interpolated in time to have continuous data. An elliptical fitting of clouds facilitates the examination of the interplay between the structure of shallow cumulus clouds and the predominant trade winds. The ellipses enable the cloud orientation to be viewed against a reference, allowing different cloud patterns to become comparable. Using the eccentricity based on the aspect ratio for each cloud, the directional extension of clouds under the impact of the wind field is analysed. Considering the inclination of clouds in the prevailing wind direction, the influence of the wind field on cloud shape is elucidated in Chapter 6. To examine the cloud-controlling role of wind speed, two cases are depict, namely wind speeds below 5.5 m/s and above 10.0 m/s in CTH.

Based on this broad framework of analytic tools, the major answers regarding the mentioned questions can be given as follows: Concerning the first two scientific question on specMACS-radar intercomparison and macrophysical cloud properties, the thesis points out the main benefit of airborne-based cloud statistics from specMACS compared to the radar. specMACS substantially increases the sample of observed clouds through its larger FOV. Capturing 80,000 clouds during simultaneous measurements with the radar on the six investigated RFs, specMACS sees 80 times more clouds than the radar. For these clouds, it is found that their along-track length underlie double power law characteristics together with a pronounced scale break in the size distribution around 500 m similar to findings of Mieslinger et al. (2019) from satellite images of similar spatial resolution. The across-track perspective in turn allows to detect the entire horizontal extension of clouds that is not necessarily aligned with the flight heading. Restricted to shallow convection regimes and based on the cloud-area equivalent diameter D, the scale break in the cloud size distribution appears at larger cloud sizes of 776 m. This difference partly results from an undersampling of larger clouds as the chance of large clouds to be detected entirely decreases with increasing size. However, as the along-track distribution based on shallow convection also reveal a scale break above 700 m, the lower scale break found from all six flights possibly results from additional cloud regimes in different height levels reaching into the FOV. Moreover, the size investigation reveals that the vast majority of clouds is subgrid-scale ($D < 200$ m) for the radar measurements. Their contribution to the total cloud cover is, however, minor. While for all clouds captured in their whole extent, the median value of D is 101 m, the contribution of the smaller half of clouds to the total cloud-covered area is below 10 %.

Regarding the research question of typical cloud shape, the elliptical fit represents a valid simplification in most cases, as clouds mainly consist of a certain aspect ratio. Shallow cumuli clouds overall underlie similar shape tendencies which was found using the fractal dimension. Having a value of 1.19, the fractal dimension reveals that clouds overall have rather smooth shapes which is equivalently found in Mieslinger et al. (2019). Individually comparing cloud shapes to their convex hulls based on Brinkhoff et al. (1995), certain clouds, however, proved to strongly differ from a convex hull and thus from an elliptical shape. Apart from resolution effects, this is assumed to be related to up- and downdraft circulations and turbulence effects around clouds deformatting their shapes.

The cloud field geometry is examined by means of the organisation index I_{org}. For the six RFs06, entirely and on 10-minutely scale, I_{org} values above 0.5 robustly indicate clustered organisation of the cloud fields. Since the FOV of specMACS, however, is relatively small for mesoscale cloud organisation, the rather high I_{org} values above 0.7, averaged for each flight, primarily result from small cloud fragments that are close to the larger cloud patterns. Filtering out small clouds, the I_{org} persists in the clustered regime, especially also for RF06 in shallow convection, but is generally reduced by 0.1 compared to the initial resolution. On average, the nearest neighbour distances between paired clouds are similar to the cloud sizes with values between 200 and 350 m. Cloud gaps are significantly lower, with an average below 100 m.

In order to certainly answer if the trade winds impacts the cloud shape, the investigation on coupling between clouds and the wind field is restricted to the uncertainties of cloud top height and wind direction. This requires the exclusion of several flights and flight periods. For instance, BL-conditions during RF05 are favourable with high wind speeds above 12 m/s and with observed shallow clouds organised as cloud streets. However, the uncertainties of the wind field are high as only two dropsondes were released within a period of two hours. From considering RF03 and RF06 performed in shallow convection, clouds show a significant directional extension with mean eccentricity values above 0.7. Moreover, clouds are slightly more stretched at higher wind speeds. The combined effect of stretching and inclination of clouds into wind direction is also stronger found at higher wind speeds. In conclusion, 1D cloud size statistics are not necessarily invariant to direction due to the fact that clouds overall show a certain stretched orientation. Along-track cloud size spectra can hence be biased as they do not include the dominant axes of clouds. Intercomparing the 1D cloud size spectra in different perspectives for both devices, such as along the flight track, along their major elliptic axis and along their diameter in wind

direction, the effect of dominant cloud orientation under dominant winds on cloud size distribution is visible but lower than expected. Since the shallow low-level clouds are sensitive to several atmospheric processes within the trade-wind region, it is pointed out that several other cloud-controlling factors such as estimated inversion strength (EIS) (Myers and Norris, 2013) or Bowen ratio (the ratio of the surface sensible heat flux to latent heat flux) (Sakradzija and Hohenegger, 2017) can also have significant influences on the investigated cloud properties.

Finally, the thesis' findings expand those of Gödde (2018) by emphasising the applicability of specMACS data to derive macrophysical cloud properties, such as 2D horizontal geometries. Moreover, the properties are very similar those the large statistics of marine shallow clouds found by Mieslinger et al. (2019). This underlines the representativity of the clouds captured during NARVAL-II. The elliptical description constitutes a useful and representative view on the dominant cloud extension. The response of the cloud geometries to the wind speed is weaker than expected but robust under the assumptions made and does not contradict previous findings from literature. Nonetheless, the range of considered wind speed cases is limited due to the focus on two flights, as high wind-speeds above 12 m/s rarely occurred.

8.2 Outlook

While 1D cloud geometries along the flight path can more or less be directly inferred from the along-track coordinate system in specMACS (Section 4.1), limitations in analysing 2D single cloud geometries and organisation occur where the Cartesian coordinate system comes into play. This results from the CTH assumptions necessary for the projection to Cartesian coordinates in order to examine 2D cloud geometries. Robust wind-based cloud geometries (Chapter 7) are only gained for two RFs due to high uncertainties in CTH and wind field assumptions in all other cases. However, the exclusion of entire RFs strongly reduces the sample of clouds for the pursued research questions. Since the radar did not resolve several overpassed shallow clouds also due to a lower sensitivity, the lack of information could partly be filled by including the LiDAR measurements from WALES. By that, the along-track CTH values would be based on a higher cloud sample. Moreover, 2D geometries of low-level clouds could be examined from other RFs in shallow convection during which the radar was not in operation (Section 2.5), so that the measurements from WALES could have been very fruitful. Nonetheless, remaining uncertainties for the 2D cloud projection into the Cartesian system are subject of the simplified across-track constant cloud height,

so that there is still room for improvements. Therefore, the algorithm of Barker et al. (2011) (Section 7.4), distributing the nadir information of active measurements to the across-track, could provide much more accurate estimates. Making use of this across-track distributing algorithm, optimised for specMACS by Lucas Höppler, the across-track cloud height representation could also considerably increase the cloud samples, as fewer cloud would be excluded due to initially high uncertainties in CTH. Consequently, this would increase the representativity of the shallow low-level cloud properties. Including this algorithm can raise new capabilities for further research about the impact of cloud-internal wind shear on the 3D structure of clouds.

Furthermore, the interactions between the wind field and the precipitation in shallow convection are an ongoing field that is only touched in this thesis, as the radar-based sample of precipitating shallow clouds during RF03 and RF06 is rather small. The fusion of the single cloud characterisitics with the hydrometeor paths from Jacob et al. (2019a) can better set macrophysical cloud characteristics from specMACS in relation precipitation. Identifying precipitating clouds within the specMACS cloud mask through the algorithm of Barker et al. (2011), applying the geometrical methods of this thesis, and further including hydrometeor paths from (Jacob et al., 2019b), would enable the investigation of following questions:

- To what degree do 2D geometries of low-level clouds differ between precipitating and non-precipitating clouds in specMACS?
- Does a characteristic threshold in cloud area exist above that shallow cumulus clouds start precipitating (Nuijens et al., 2015)?
- To what extent do precipitating shallow clouds show wind-induced elongations or are internal precipitating-regulated dynamics (Zuidema et al., 2017) responsible for their shape?
- Is the controlling role of wind speed on the number of precipitating shallow clouds (Nuijens et al., 2009) also visible in specMACS measurements during NARVAL-II? Does the spatial arrangement of clouds change in the environment of precipitating clouds, e.g. towards more cluster as found in LES (Vogel et al., 2016)?

Results become more representative if there is a larger sample of collocated remote-sensing measurements and vertical information from dropsondes, which are otherwise hardly observed over the ocean. Apart from including more RFs from NARVAL-II by additionally using WALES, the EUREC^{4}A aircraft campaign being performed from January to February 2020 (Bony et al., 2017) represents a big

milestone for observational datasets of marine tropical clouds structures. While the NARVAL-II took place in the wet season, typically lasting from June to December, EUREC^{4}A is conducted during the dry season. EUREC^{4}A comprises tropical marine cloud measurements within a completely different meteorological scenario according to long-term observations (Medeiros and Nuijens, 2016; Stevens et al., 2016); During the dry season, relative humidity in high-levels and especially in mid-levels (between 4-8 km) is substantially lower. In the lower troposphere, however, shallow convection is more favoured and dominant due to stronger subsidence rates manifesting in stronger lower tropospheric stability than observed during NARVAL-II (Section 2.6). Speaking from the thesis' perspective regarding airborne measurements from specMACS, this is expressed through fewer clouds being overlapped by clouds in mid- and high-levels or deep convection. Consequently, more flight periods will be suitable to investigate shallow low-level clouds based on the elliptical approach. In addition, specMACS is equipped with improved cameras for EUREC^{4}A, having a higher resolution, so that cloud structures can be captured even more accurately. In particular complex techniques aiming to obtain the CTH, such as from Kölling et al. (2019), that reach beyond the scope of the thesis, will benefit from the improved specMACS.

Moreover, the trade winds are stronger during dry season which is correlated to the low-level cloudiness (Brueck et al., 2015). Consequently, EUREC^{4}A will increase the framework of tropospheric conditions favorable for the investigation of the coupling between clouds and the trade winds, and particularly broaden the range of wind speeds considered in this thesis. It remains to be seen whether or not the influence of the trades on the elongation of the clouds will be stronger during EUREC^{4}A. Out-coming key questions based on the thesis' findings may be:

- Are the cloud-wind couplings identified from both RFs in shallow convection during NARVAL-II representative and can they be reproduced in larger sample of shallow low-level clouds?
- Do characteristic differences in the wind-induced horizontal shallow cloud geometries appear between dry and wet season? Do shallow clouds respond to increasing wind speed similarly to the findings of this thesis?

Consequently, the potential of analysing the coupling between tropical marine cumulus clouds and the trade winds using airborne remote-sensing devices, such as specMACS, is far from being exhausted. A better understanding of these clouds, their geometries, their cloud field characteristics as well as their cloud-controlling factors from such aircraft-based observations might help to lower the uncertainties of shallow cumulus cloud feedbacks in current climate models.

Appendix

Mathematical Background on Cloud Size Distributions

As background information, the mathematical derivation of cloud size distribution parameters in logarithmic space assuming a power law distribution, that links the equations 4.1 and 4.7 are described. The mathematical steps are taken from Mieslinger et al. (2019) and will be briefly sketched as this point. From the definition of the area equivalent diameter D, it follows that the area of the cloud is described as $x = A = \frac{\pi}{4} \cdot D^2$ and $\frac{dx}{dD} = \frac{\pi}{2} \cdot D$. Hence, applying the variable transformation method leads to:

$$\begin{aligned} n(D) &= n(A) \cdot \frac{dA}{dD} \\ &= n(A) \cdot \frac{\pi}{2} \cdot D \end{aligned} \tag{8.1}$$

With term transformation follows:

$$n(A) = n(D) \cdot \frac{2}{\pi} \cdot D^{-1} \tag{8.2}$$

Using Equation 4.1 for $n(D)$ produces:

$$\begin{aligned} n(A) &= \left(a \cdot D^{\beta}\right) \cdot \frac{2}{\pi} \cdot D^{-1} \\ &= a \cdot \frac{2}{\pi} \cdot D^{\beta-1} \\ &= a'' \cdot A^{\frac{\beta-1}{2}}. \end{aligned} \tag{8.3}$$

Based on $x = \log(A) = \log(\frac{\pi}{4}D^2)$ and $\frac{dx}{dD}$ it applies:

$$n(\log(A)) = n(D) \cdot \frac{\ln(10)}{2} D \quad = a''' \cdot A^{\frac{\beta+1}{2}}. \tag{8.4}$$

Frequency of vibration Brinkhoff et al. (1995)

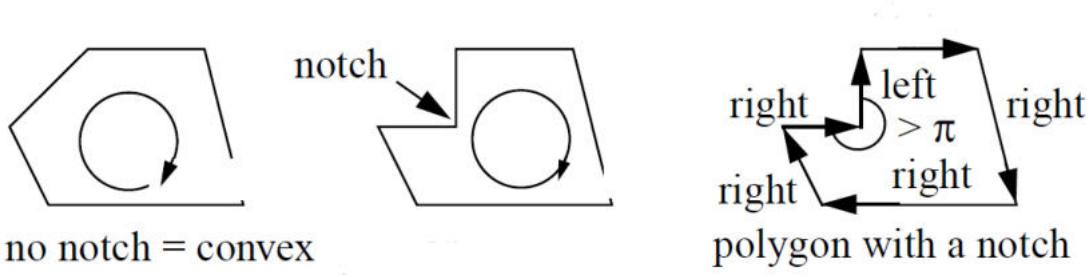

Figure A.1: Visualisation of notches and vertices adapted from Brinkhoff et al. (1995).

Surface Wind Speed

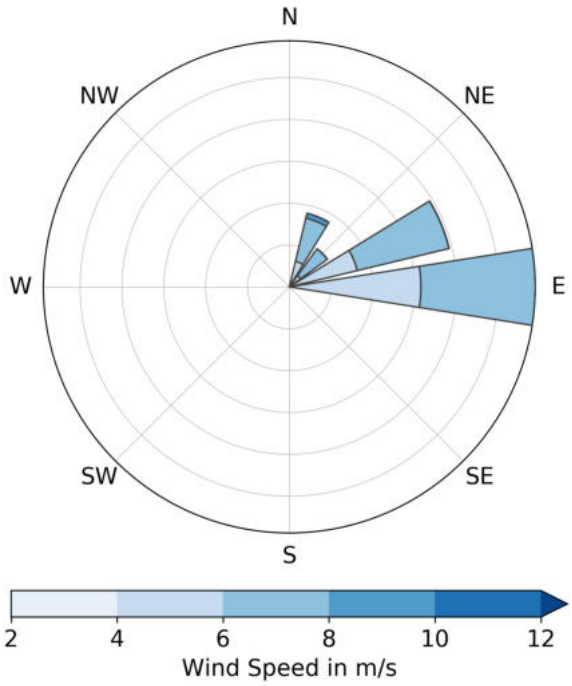

Figure A.2: Windrose describing the surface wind field from RF03 and RF06, which here represents the wind field averaged over the lowest 100 m above sea surface.

Eccentricity Dependency on Aspect Ratio

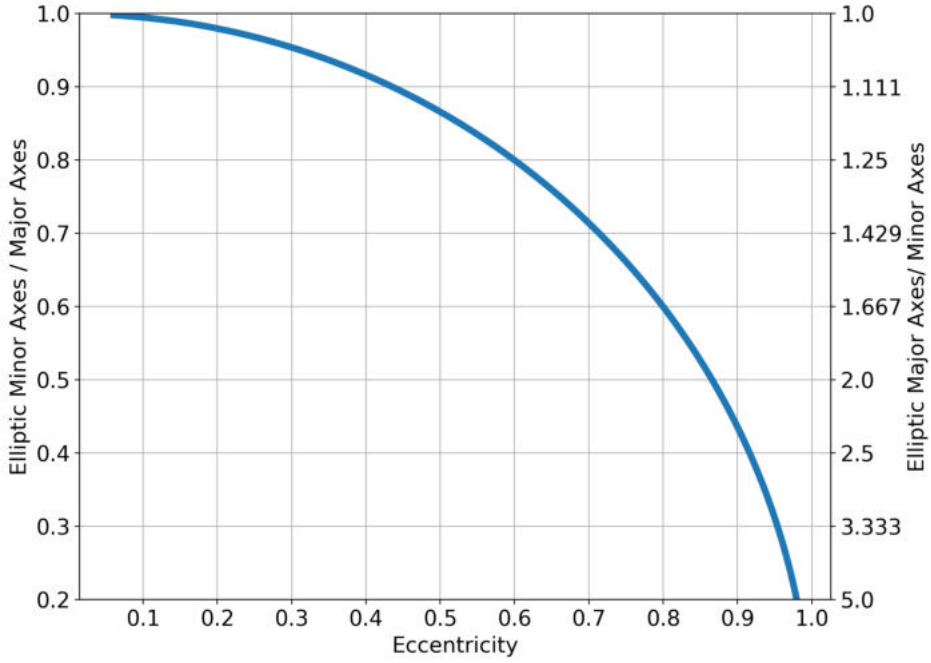

Figure A.3: Mathematical relation between eccentricity and aspect ratio of an ellipse (elliptical minor axis divided by elliptical major axis). The inverse aspect ratio is also shown on the right y-axis.

References

Ackerman, S. and R. A. Frey, 2015: MODIS Atmosphere L2 Cloud Mask Product. *NASA MODIS Adaptive Processing System*.

Augstein, E., H. Schmidt, and F. Ostapoff, 1974: The vertical structure of the atmospheric planetary boundary layer in undisturbed trade winds over the Atlantic Ocean. *Boundary-Layer Meteorology*, **6**, 129–150, doi:10.1007/BF00232480.

Barker, H. W., M. P. Jerg, T. Wehr, S. Kato, D. P. Donovan, and R. J. Hogan, 2011: A 3D cloud-construction algorithm for the EarthCARE satellite mission. *Quarterly Journal of the Royal Meteorological Society*, **137**, 1042–1058, doi:10.1002/qj.824.

Batista-Tomás, A. R., O. Díaz, A. J. Batista-Leyva, and E. Altshuler, 2015: Classification and dynamics of tropical clouds by their fractal dimension. *Quarterly Journal of the Royal Meteorological Society*, **142**, 983–988, doi:10.1002/qj.2699.

Benner, T. C. and J. A. Curry, 1998: Characteristics of small tropical cumulus clouds and their impact on the environment. *Journal of Geophysical Research: Atmospheres*, **103**, 28753–28767, doi:10.1029/98jd02579.

Bony, S. and B. Stevens, 2019: Measuring Area-Averaged Vertical Motions with Dropsondes. *Journal of the Atmospheric Sciences*, **76**, 767–783, doi:10.1175/jas-d-18-0141.1.

Bony, S., B. Stevens, F. Ament, S. Bigorre, P. Chazette, S. Crewell, J. Delanoë, K. Emanuel, D. Farrell, C. Flamant, S. Gross, L. Hirsch, J. Karstensen, B. Mayer, L. Nuijens, J. H. Ruppert, I. Sandu, P. Siebesma, S. Speich, F. Szczap, J. Totems, R. Vogel, M. Wendisch, and M. Wirth, 2017: EUREC4A: A Field Campaign to Elucidate the Couplings Between Clouds, Convection and Circulation. *Surveys in Geophysics*, **38**, 1529–1568, doi:10.1007/s10712-017-9428-0.

Bony, S., B. Stevens, D. M. W. Frierson, C. Jakob, M. Kageyama, R. Pincus, T. G. Shepherd, S. C. Sherwood, A. P. Siebesma, A. H. Sobel, M. Watanabe, and M. J. Webb, 2015: Clouds, circulation and climate sensitivity. *Nature Geoscience*, **8**, 261–268, doi:10.1038/ngeo2398.

Braden, B., 1986: The Surveyors Area Formula. *The College Mathematics Journal*, **17**, 326, doi:10.2307/2686282.

Bretherton, C. S. and P. N. Blossey, 2017: Understanding Mesoscale Aggregation of Shallow Cumulus Convection Using Large-Eddy Simulation. *Journal of Advances in Modeling Earth Systems*, **9**, 2798–2821, doi:10.1002/2017ms000981.

Bretherton, C. S., P. N. Blossey, and C. R. Jones, 2013: Mechanisms of marine low cloud sensitivity to idealized climate perturbations: A single-LES exploration extending the CGILS cases. *Journal of Advances in Modeling Earth Systems*, **5**, 316–337, doi:10.1002/jame.20019.

Brinkhoff, T., H.-P. Kriegel, R. Schneider, and A. Braun, 1995: Measuring the Complexity of Polygonal Objects. *ACM-GIS*.

Brueck, M., L. Nuijens, and B. Stevens, 2015: On the Seasonal and Synoptic Time-Scale Variability of the North Atlantic Trade Wind Region and Its Low-Level Clouds. *Journal of the Atmospheric Sciences*, **72**, 1428–1446, doi:10.1175/jas-d-14-0054.1.

Busen, R., 2012: Dropsondes and Radiosondes for Atmospheric Measurements. *Atmospheric Physics: Background - Methods - Trends*, 317–, doi:10.1007/978-3-642-30183-4_19.

Ceppi, P., F. Brient, M. D. Zelinka, and D. L. Hartmann, 2017: Cloud feedback mechanisms and their representation in global climate models. *Wiley Interdisciplinary Reviews: Climate Change*, **8**, e465, doi:10.1002/wcc.465.

Chazette, P., F. Marnas, J. Totems, and X. Shang, 2014: Comparison of IASI water vapor retrieval with H2O-Raman lidar in the framework of the Mediterranean HyMeX and ChArMEx programs. *Atmospheric Chemistry and Physics*, **14**, 9583–9596, doi:10.5194/acp-14-9583-2014.

Chen, Q., J. Fan, S. Hagos, W. I. Gustafson, and L. K. Berg, 2015: Roles of wind shear at different vertical levels: Cloud system organization and properties. *Journal of Geophysical Research: Atmospheres*, **120**, 6551–6574, doi:10.1002/2015jd023253.

Cox, C. and W. Munk, 1954: Measurement of the Roughness of the Sea Surface from Photographs of the Sun's Glitter. *Journal of the Optical Society of America*, **44**, 838, doi:10.1364/josa.44.000838.

Ewald, F., S. Groß, M. Hagen, L. Hirsch, J. Delanoë, and M. Bauer-Pfundstein, 2019: Calibration of a 35&thinspGHz airborne cloud radar: lessons learned and intercomparisons with 94&thinspGHz cloud radars. *Atmospheric Measurement Techniques*, **12**, 1815–1839, doi:10.5194/amt-12-1815-2019.

Ewald, F., T. Kölling, A. Baumgartner, T. Zinner, and B. Mayer, 2016: Design and characterization of specMACS, a multipurpose hyperspectral cloud and sky imager. *Atmospheric Measurement Techniques*, **9**, 2015–2042, doi:10.5194/amt-9-2015-2016.

Fitzgibbon, A. W. and M. P. R. B. Fisher, 1996: Direct Least Squares Fitting of Ellipses. *Proc. of the 13th Internation Conference on Pattern Recognition*, 253–257.

Gentle, J. E., 2017: *Matrix Algebra*. Springer International Publishing. URL `https://doi.org/10.1007/978-3-319-64867-5`

Gödde, F., 2018: Detecting Clouds in the Presence of Sunglint: An Approach Using Spectral Water Vapor Absorption. *Master Thesis*.

Ham, S.-H., S. Kato, H. W. Barker, F. G. Rose, and S. Sun-Mack, 2014: Effects of 3-D clouds on atmospheric transmission of solar radiation: Cloud type dependencies inferred from A-train satellite data. *Journal of Geophysical Research: Atmospheres*, **119**, 943–963, doi:10.1002/2013jd020683.

Henderson-Sellers, A. and K. McGuffie, 1990: Are cloud amounts estimated from satellite sensor and conventional surface-based observations related? *International Journal of Remote Sensing*, **11**, 543–550, doi:10.1080/01431169008955038.

Heus, T. and A. Seifert, 2013: Automated tracking of shallow cumulus clouds in large domain, long duration large eddy simulations. *Geoscientific Model Development*, **6**, 1261–1273, doi:10.5194/gmd-6-1261-2013.

Hinkelman, L. M., K. F. Evans, E. E. Clothiaux, T. P. Ackerman, and P. W. Stackhouse, 2007: The Effect of Cumulus Cloud Field Anisotropy on Domain-Averaged Solar Fluxes and Atmospheric Heating Rates. *Journal of the Atmospheric Sciences*, **64**, 3499–3520, doi:10.1175/jas4032.1.

Jacob, M., F. Ament, M. Gutleben, H. Konow, M. Mech, M. Wirth, and S. Crewell, 2019a: Investigating the liquid water path over the tropical Atlantic with synergistic airborne measurements. *Atmospheric Measurement Techniques*, **12**, 3237–3254, doi:10.5194/amt-12-3237-2019.

— 2019b: Liquid water path and integrated water vapor over the tropical Atlantic during NARVAL2.
URL `https://doi.org/10.26050/WDCC/HALO_measurements_6`

JCGM, 2008: Evaluation of measurement data – Guide to the expression of uncertainty in measurement (GUM). *International Journal of Remote Sensing*, **11**.

Kadoya, T. and H. Masunaga, 2018: New Observational Metrics of Convective Self-Aggregation: Methodology and a Case Study. *Journal of the Meteorological Society of Japan. Ser. II*, **96**, 535–548, doi:10.2151/jmsj.2018-054.

Klein, S. A., 1997: Synoptic Variability of Low-Cloud Properties and Meteorological Parameters in the Subtropical Trade Wind Boundary Layer. *Journal of Climate*, **10**, 2018–2039, doi:10.1175/1520-0442(1997)010¡2018:svolcp¿2.0.co;2.

Klein, S. A., A. Hall, J. R. Norris, and R. Pincus, 2018: Low-Cloud Feedbacks from Cloud-Controlling Factors: A Review. *Shallow Clouds, Water Vapor, Circulation, and Climate Sensitivity*, doi:10.1007/978-3-319-77273-8_7.

Kölling, T., 2020: macsserver. `https://macsserver.physik.uni-muenchen.de/`, accessed: 2020-03-01.

Kölling, T., T. Zinner, and B. Mayer, 2019: Aircraft-based stereographic reconstruction of 3-D cloud geometry. *Atmospheric Measurement Techniques*, **12**, 1155–1166, doi:10.5194/amt-12-1155-2019.

Konow, H., M. Jacob, F. Ament, S. Crewell, F. Ewald, M. Hagen, L. Hirsch, F. Jansen, M. Mech, and B. Stevens, 2018: HALO Microwave Package measurements during Next-generation Remote sensing for VALidation Studies 2 (NARVAL2).
URL `https://doi.org/10.1594/WDCC/HALO_measurements_3`

— 2019: A unified data set of airborne cloud remote sensing using the HALO Microwave Package (HAMP). *Earth System Science Data*, **11**, 921–934, doi:10.5194/essd-11-921-2019.

Koren, I., L. Oreopoulos, G. Feingold, L. A. Remer, and O. Altaratz, 2008: How small is a small cloud? *Atmospheric Chemistry and Physics*, **8**, 3855–3864, doi:10.5194/acp-8-3855-2008.

Krautstrunk, M. and A. Giez, 2012: The Transition From FALCON to HALO Era Airborne Atmospheric Research. *Atmospheric Physics*, Springer Berlin Heidelberg, 609–624.
URL `https://doi.org/10.1007/978-3-642-30183-4_37`

L. Tsang, J. K. R. S., 1985: *Theory of microwave remote sensing*, volume 613. (New York: John Wiley).

Lee, Y. and W. Lim, 2017: Shoelace Formula: Connecting the Area of a Polygon with Vector Cross Product. *The Mathematics Teacher*, **110**, 631, doi:10.5951/mathteacher.110.8.0631.

Li, Z., P. Zuidema, and P. Zhu, 2014: Simulated Convective Invigoration Processes at Trade Wind Cumulus Cold Pool Boundaries. *Journal of the Atmospheric Sciences*, **71**, 2823–2841, doi:10.1175/jas-d-13-0184.1.

Lovejoy, S., 1982: Area-Perimeter Relation for Rain and Cloud Areas. *Science*, **216**, 185–187, doi:10.1126/science.216.4542.185.

Mapes, B. E. and R. A. Houze, 1995: Diabatic Divergence Profiles in Western Pacific Mesoscale Convective Systems. *Journal of the Atmospheric Sciences*, **52**, 1807–1828, doi:10.1175/1520-0469(1995)052¡1807:ddpiwp¿2.0.co;2.

May, R. M., S. C. Arms, P. Marsh, E. Bruning, J. R. Leeman, K. Goebbert, J. E. Thielen, and Z. S. Bruick, 2020: MetPy: A Python Package for Meteorological Data.
URL `https://github.com/Unidata/MetPy`

Mech, M., E. Orlandi, S. Crewell, F. Ament, L. Hirsch, M. Hagen, G. Peters, and B. Stevens, 2014: HAMP – the microwave package on the High Altitude and LOng range research aircraft (HALO). *Atmospheric Measurement Techniques*, **7**, 4539–4553, doi:10.5194/amt-7-4539-2014.

Medeiros, B. and L. Nuijens, 2016: Clouds at Barbados are representative of clouds across the trade wind regions in observations and climate models. *Proceedings of the National Academy of Sciences*, **113**, E3062–E3070, doi:10.1073/pnas.1521494113.

Medeiros, B., B. Stevens, and S. Bony, 2015: Using aquaplanets to understand the robust responses of comprehensive climate models to forcing. *Climate Dynamics*, **44**, 1957–1977, doi:10.1007/s00382-014-2138-0.

Mieslinger, T., A. Horvvath, S. A. Buehler, and M. Sakradzija, 2019: The dependence of shallow cumulus macrophysical properties on large-scale meteorology as observed in ASTER imagery. *JGR: Atmospheres*.

Myers, T. A. and J. R. Norris, 2013: Observational Evidence That Enhanced Subsidence Reduces Subtropical Marine Boundary Layer Cloudiness. *Journal of Climate*, **26**, 7507–7524, doi:10.1175/jcli-d-12-00736.1.

Neggers, R. A. J., P. J. Griewank, and T. Heus, 2019: Power-Law Scaling in the Internal Variability of Cumulus Cloud Size Distributions due to Subsampling and Spatial Organization. *Journal of the Atmospheric Sciences*, **76**, 1489–1503, doi:10.1175/jas-d-18-0194.1.

Neggers, R. A. J., H. J. J. Jonker, and A. P. Siebesma, 2003: Size Statistics of Cumulus Cloud Populations in Large-Eddy Simulations. *Journal of the Atmospheric Sciences*, **60**, 1060–1074, doi:10.1175/1520-0469(2003)60¡1060:ssoccp¿2.0.co;2.

Nuijens, L., B. Medeiros, I. Sandu, and M. Ahlgrimm, 2015: The behavior of trade-wind cloudiness in observations and models: The major cloud components and their variability. *Journal of Advances in Modeling Earth Systems*, **7**, 600–616, doi:10.1002/2014ms000390.

Nuijens, L. and A. P. Siebesma, 2019: Boundary Layer Clouds and Convection over Subtropical Oceans in our Current and in a Warmer Climate. *Current Climate Change Reports*, **5**, 80–94, doi:10.1007/s40641-019-00126-x.

Nuijens, L. and B. Stevens, 2012: The Influence of Wind Speed on Shallow Marine Cumulus Convection. *Journal of the Atmospheric Sciences*, **69**, 168–184, doi:10.1175/jas-d-11-02.1.

Nuijens, L., B. Stevens, and A. P. Siebesma, 2009: The Environment of Precipitating Shallow Cumulus Convection. *Journal of the Atmospheric Sciences*, **66**, 1962–1979, doi:10.1175/2008jas2841.1.

Pavicic, S. J., 2018: Cloudfraction during the NARVAL-2 campaign. *Bachelor Thesis*.

Plank, V. G., 1969: The Size Distribution of Cumulus Clouds in Representative Florida Populations. *Journal of Applied Meteorology*, **8**, 46–67, doi:10.1175/1520-0450(1969)008¡0046:tsdocc¿2.0.co;2.

Rasp, S., T. Selz, and G. C. Craig, 2018: Variability and Clustering of Midlatitude Summertime Convection: Testing the Craig and Cohen Theory in a Convection-Permitting Ensemble with Stochastic Boundary Layer Perturbations. *Journal of the Atmospheric Sciences*, **75**, 691–706, doi:10.1175/jas-d-17-0258.1.

Rauber, R. M., B. Stevens, H. T. Ochs, C. Knight, B. A. Albrecht, A. M. Blyth, C. W. Fairall, J. B. Jensen, S. G. Lasher-Trapp, O. L. Mayol-Bracero, G. Vali, J. R. Anderson, B. A. Baker, A. R. Bandy, E. Burnet, J.-L. Brenguier, W. A. Brewer, P. R. A. Brown, R. Chuang, W. R. Cotton, L. D. Girolamo, B. Geerts, H. Gerber, S. Göke, L. Gomes, B. G. Heikes, J. G. Hudson, P. Kollias, R. R. Lawson, S. K. Krueger, D. H. Lenschow, L. Nuijens, D. Sullivan, R. A. Rilling, D. C. Rogers, A. P. Siebesma, E. Snodgrass, J. L. Stith, D. C. Thornton, S. Tucker, C. H. Twohy, and P. Zuidema, 2007: Rain in Shallow Cumulus Over the Ocean: The RICO Campaign. *Bulletin of the American Meteorological Society*, **88**, 1912–1928, doi:10.1175/bams-88-12-1912.

Rosenfeld, A. and A. C. Kak, 1982: *Digital Picture Processing*. Academic Press.

Sakradzija, M. and C. Hohenegger, 2017: What Determines the Distribution of Shallow Convective Mass Flux through a Cloud Base? *Journal of the Atmospheric Sciences*, **74**, 2615–2632, doi:10.1175/jas-d-16-0326.1.

Sengupta, S. K., R. M. Welch, M. S. Navar, T. A. Berendes, and D. W. Chen, 1990: Cumulus Cloud Field Morphology and Spatial Patterns Derived from High Spatial Resolution Landsat Imagery. *Journal of Applied Meteorology*, **29**, 1245–1267, doi:10.1175/1520-0450(1990)029¡1245:ccfmas¿2.0.co;2.

Siebesma, A., J.-L. Brenguier, C. Bretherton, W. Grabowski, J. Heintzenberg, B. Kaercher, K. Lehmann, J. Petch, P. Spichtinger, B. Stevens, and F. Stratmann, 2009: *Cloud-controlling factors: low clouds*. Cambridge, Mass.: MIT Press, In J. Heintzenberg, & R. Charlson (Eds.), 173–196 pp.

Siebesma, A. P., 1998: Shallow Cumulus Convection. *Buoyant Convection in Geophysical Flows*, Springer Netherlands, 441–486.
URL `https://doi.org/10.1007/978-94-011-5058-3{_}19`

Song, L. and Q. Min, 2011: Cloud 3D effects on broadband heating rate profiles: I. Model simulation. *Journal of Quantitative Spectroscopy and Radiative Transfer*, **112**, 292–303, doi:10.1016/j.jqsrt.2010.06.020.

Stein, T. H. M., C. E. Holloway, I. Tobin, and S. Bony, 2017: Observed Relationships between Cloud Vertical Structure and Convective Aggregation over Tropical Ocean. *Journal of Climate*, **30**, 2187–2207, doi:10.1175/jcli-d-16-0125.1.

Stevens, B., F. Ament, S. Bony, S. Crewell, F. Ewald, S. Gross, A. Hansen, L. Hirsch, M. Jacob, T. Kölling, H. Konow, B. Mayer, M. Wendisch, M. Wirth, K. Wolf, S. Bakan, M. Bauer-Pfundstein, M. Brueck, J. Delanoë, A. Ehrlich, D. Farrell, M. Forde, F. Gödde, H. Grob, M. Hagen, E. Jäkel, F. Jansen, C. Klepp, M. Klingebiel, M. Mech, G. Peters, M. Rapp, A. A. Wing, and T. Zinner, 2019a: A High-Altitude Long-Range Aircraft Configured as a Cloud Observatory: The NARVAL Expeditions. *Bulletin of the American Meteorological Society*, **100**, 1061–1077, doi:10.1175/bams-d-18-0198.1.

— 2019b: A High-Altitude Long-Range Aircraft Configured as a Cloud Observatory: The NARVAL Expeditions. *Bulletin of the American Meteorological Society*, **100**, 1061–1077, doi:10.1175/bams-d-18-0198.1.

Stevens, B., S. Bony, H. Brogniez, L. Hentgen, C. Hohenegger, C. Kiemle, T. S. LEcuyer, A. K. Naumann, H. Schulz, P. A. Siebesma, J. Vial, D. M. Winker, and P. Zuidema, 2019c: Sugar, Gravel, Fish, and Flowers: Mesoscale cloud patterns in the Tradewinds. *Quarterly Journal of the Royal Meteorological Society*, doi:10.1002/qj.3662.

Stevens, B., H. Brogniez, C. Kiemle, J.-L. Lacour, C. Crevoisier, and J. Kiliani, 2017: Structure and Dynamical Influence of Water Vapor in the Lower Tropical Troposphere. *Surveys in Geophysics*, **38**, 1371–1397, doi:10.1007/s10712-017-9420-8.

Stevens, B., D. Farrell, L. Hirsch, F. Jansen, L. Nuijens, I. Serikov, B. Brügmann, M. Forde, H. Linne, K. Lonitz, and J. M. Prospero, 2016: The Barbados Cloud Observatory: Anchoring Investigations of Clouds and Circulation on the Edge of the ITCZ. *Bulletin of the American Meteorological Society*, **97**, 787–801, doi:10.1175/bams-d-14-00247.1.

Tobin, I., S. Bony, and R. Roca, 2012: Observational Evidence for Relationships between the Degree of Aggregation of Deep Convection, Water Vapor, Surface Fluxes, and Radiation. *Journal of Climate*, **25**, 6885–6904, doi:10.1175/jcli-d-11-00258.1.

Tompkins, A. M. and A. G. Semie, 2017: Organization of tropical convection in low vertical wind shears: Role of updraft entrainment. *Journal of Advances in Modeling Earth Systems*, **9**, 1046–1068, doi:10.1002/2016ms000802.

van der Walt, S., J. L. Schönberger, J. Nunez-Iglesias, F. Boulogne, J. D. Warner, N. Yager, E. Gouillart, and T. Yu, 2014: scikit-image: image processing in Python. *PeerJ*, **2**, e453, doi:10.7717/peerj.453.

Vial, J., S. Bony, B. Stevens, and R. Vogel, 2017: Mechanisms and Model Diversity of Trade-Wind Shallow Cumulus Cloud Feedbacks: A Review. *Surveys in Geophysics*, **38**, 1331–1353, doi:10.1007/s10712-017-9418-2.

Vial, J., R. Vogel, S. Bony, B. Stevens, D. M. Winker, X. Cai, C. Hohenegger, A. K. Naumann, and H. Brogniez, 2019: A New Look at the Daily Cycle of Trade Wind Cumuli. *Journal of Advances in Modeling Earth Systems*, **11**, 3148–3166, doi:10.1029/2019ms001746.

Vogel, R., L. Nuijens, and B. Stevens, 2016: The role of precipitation and spatial organization in the response of trade-wind clouds to warming. *Journal of Advances in Modeling Earth Systems*, **8**, 843–862, doi:10.1002/2015ms000568.

Wang, J. J., K. Young, T. Hock, D. Lauritsen, D. Behringer, M. Black, P. G. Black, J. Franklin, J. Halverson, J. Molinari, L. Nguyen, T. Reale, J. Smith, B. Sun, Q. Wang, and J. A. Zhang, 2015: A Long-Term, High-Quality, High-Vertical-Resolution GPS Dropsonde Dataset for Hurricane and Other Studies. *Bulletin of the American Meteorological Society*, **96**, 961–973, doi:10.1175/bams-d-13-00203.1.

Weger, R. C., J. Lee, T. Zhu, and R. M. Welch, 1992: Clustering, randomness and regularity in cloud fields: 1. Theoretical considerations. *Journal of Geophysical Research*, **97**, 20519, doi:10.1029/92jd02038.

Wendisch, M., D. Müller, D. Schell, and J. Heintzenberg, 2001: An Airborne Spectral Albedometer with Active Horizontal Stabilization. *Journal of Atmospheric and Oceanic Technology*, **18**, 1856–1866, doi:10.1175/1520-0426(2001)0181856:aasawa 2.0.*co* 2.

White, B. A., A. M. Buchanan, C. E. Birch, P. Stier, and K. J. Pearson, 2018: Quantifying the Effects of Horizontal Grid Length and Parameterized Convection on the Degree of Convective Organization Using a Metric of the Potential for Convective Interaction. *Journal of the Atmospheric Sciences*, **75**, 425–450, doi:10.1175/jas-d-16-0307.1.

Wing, A. A. and K. A. Emanuel, 2014: Physical mechanisms controlling self-aggregation of convection in idealized numerical modeling simulations. *Journal of Advances in Modeling Earth Systems*, **6**, 59–74, doi:10.1002/2013ms000269.

Wirth, M., A. Fix, P. Mahnke, H. Schwarzer, F. Schrandt, and G. Ehret, 2009: The airborne multi-wavelength water vapor differential absorption lidar WALES: system design and performance. *Applied Physics B*, **96**, 201–213, doi:10.1007/s00340-009-3365-7.

Wood, R. and P. R. Field, 2011: The Distribution of Cloud Horizontal Sizes. *Journal of Climate*, **24**, 4800–4816, doi:10.1175/2011jcli4056.1.

Yamaguchi, Y., A. Kahle, H. Tsu, T. Kawakami, and M. Pniel, 1998: Overview of Advanced Spaceborne Thermal Emission and Reflection Radiometer (ASTER). *IEEE Transactions on Geoscience and Remote Sensing*, **36**, 1062–1071, doi:10.1109/36.700991.

Zhao, G. and L. D. Girolamo, 2006: Cloud fraction errors for trade wind cumuli from EOS-Terra instruments. *Geophysical Research Letters*, **33**, doi:10.1029/2006gl027088.

— 2007: Statistics on the macrophysical properties of trade wind cumuli over the tropical western Atlantic. *Journal of Geophysical Research: Atmospheres*, **112**, doi:10.1029/2006jd007371.

Zuidema, P., Z. Li, R. J. Hill, L. Bariteau, B. Rilling, C. Fairall, W. A. Brewer, B. Albrecht, and J. Hare, 2012: On Trade Wind Cumulus Cold Pools. *Journal of the Atmospheric Sciences*, **69**, 258–280, doi:10.1175/jas-d-11-0143.1.

Zuidema, P., G. Torri, C. Muller, and A. Chandra, 2017: A Survey of Precipitation-Induced Atmospheric Cold Pools over Oceans and Their Interactions with the Larger-Scale Environment. *Surveys in Geophysics*, **38**, 1283–1305, doi:10.1007/s10712-017-9447-x.

Zuidema, P., H. Xue, and G. Feingold, 2008: Shortwave Radiative Impacts from Aerosol Effects on Marine Shallow Cumuli. *Journal of the Atmospheric Sciences*, **65**, 1979–1990, doi:10.1175/2007jas2447.1.

Acknowledgements

Zunächst möchte ich mich sehr herzlich bei Prof. Dr. Felix Ament und Dr. Heike Konow bedanken, die mir diese Arbeit ermöglicht haben und mir stets bei Fragen und Anregungen zur Verfügung standen. Insbesondere möchte ich mich dabei auch nochmal bedanken dafür, dass sie mir Reisen die Teilnahme am HALO SSP Seminar ermöglicht haben. Es handelte sich dabei um eine sehr spannende Erfahrung. Generell möchte ich der Arbeitsgruppe "Atmosphärenmessungen/Prozessmodellierung" am Meteorologischen Institut der Uni Hamburg und auch der TCO Barbados Gruppe am Max-Planck-Institut für Meteorologie danken für die nette Aufnahme und die stets spannenden Diskussionen über tropische Wolken. Neben Marcus Klingebiel, Geet George, Hauke Schulz möchte ich dabei auch besonderen Dank an Theresa Mieslinger ausrichten, die mich maßgeblich für meine Arbeit mit Ihrer Studie inspiriert hat und mir stets tollen Input gab. Im Rahmen meiner Arbeit möchte ich auch meinen Dank an Norbert Noreiks für die tollen Skizzen des Halo-Flugzeuges ausrichten, die ich für die Erstellungen meiner Abbildungen dankenswerterweise verwenden durfte.

Durch die Besuche in München möchte ich mich besonders bei der dortigen Arbeitsgruppe des Meteorologischen Instituts "Fernerkundung und Strahlungstransport", geleitet von Prof. Dr. Bernhard Meyer, bedanken, die mir einerseits mit total großer Offenheit entgegenkamen und vor allem durch zur Verfügung Stellung von specMACS Daten die Erstellung meiner Masterarbeit ermöglichten. In diesem Zuge gilt besonderer Dank an Felix Gödde auch für die Erstellung des tollen Wolkenmaskenproduktes sowie Lucas Höppler und Tobias Kölling, die mich mit ihrem unglaublichen Fachwissen stets beeindruckten und mich super bereitwillig in die Welt ihres Messgerätes einwiesen. Stets konnte ich auf euch bei Fragen zu greifen, was ich sehr zu schätzen weiß.

Abseits davon möchte ich meiner Freundin Melina Rebaum meinen herzlichsten Dank aussprechen, dass sie mich durch alle Höhen und Tiefen der Masterarbeit begleitet hat und mich stets untersützt hat. Von meinen Komillitonen möchte ich besonders Daniel Luigi Sorg, Jerome Sauer, Simon Michel, Theresa Lang, Daniel Krueger, Julia Menken und Jule Radtke danken, mit denen ich spannende Diskussionen führen konnte und dabei einen tollen fachwissenschaftlichen Ausstausch hatte. Ich danke für Eure Anrengungen.

Natürlich möchte ich mich auch bei meiner Familie und meinen Freunden bedanken, die mir stets mit Rat und Tat zur Seite gestanden sind.

Versicherung an Eides Statt

Ich versichere an Eides Statt durch meine Unterschrift, die vorliegende Arbeit selbstständig und nur unter Verwendung der angegebenen Quellen und Hilfsmittel verfasst zu haben. Hierfür wurden insbesondere keine anderen Internet-Quellen als die angegebenen verwendet. Alle Stellen, die wörtlich oder sinngemäß aus Veröffentlichungen entnommen wurden, sind als solche kenntlich gemacht. Ferner versichere ich, dass die vorliegende Arbeit nicht im Rahmen eines anderen Prüfungsverfahrens eingereicht wurde und die auf dem elektronischen Speichermedium eingereichte Fassung der schriftlich eingereichten Fassung der Arbeit entspricht.

Darüber hinaus stimme ich hiermit einer Veröffentlichung meiner Arbeit in der Fachbibliothek zu.

Hamburg, dem 02. März 2020

.....
Henning Dorff